

COHERENT MATTER WAVE MANIPULATION IN MICROGRAVITY

Dissertation

zur Erlangung des akademischen Grades
„Doktor der Naturwissenschaften“

am Fachbereich Physik, Mathematik und Informatik
der Johannes Gutenberg-Universität
in Mainz

vorgelegt von
Peter Stromberger, M. Sc.
geb. in Kopejsk

Mainz, den 15. Juni 2021

Abstract

Peter Stromberger

Coherent Matter Wave Manipulation in Microgravity

A microgravity environment offers beneficial conditions for research on cold atom clouds. The trapping potentials are not distorted by gravity, the dynamic of cold atom ensembles is determined by inter-atomic interactions and interaction with controlled external fields. Moreover, the time-of-flight is not restricted by the size of the vacuum-chamber. On the other hand, new challenges arise such as expansion velocities limiting the observability of the cold atom clouds after a long time-of-flight, less controlled environmental conditions in comparison to laboratory experiments such as temperature, vibrations, external magnetic and electric fields.

QUANTUS-2 is a mobile Bose-Einstein condensate (BEC) experiment used for experiments in microgravity in the drop tower in Bremen, Germany. It aims to utilize the microgravity environment of the drop tower to study coherent manipulation of rubidium and potassium ensembles. The most significant field of study will be atom interferometry, which prospectively will allow to test the universality of free fall at new levels of precision.

The main objective of QUANTUS-2 is to investigate atom interferometry in microgravity. The sensitivity of atom interferometers increases quadratically with the interrogation time making microgravity an ideal environment. Utilizing a magnetic lens in combination with collective mode excitations, we were able to reduce the expansion velocity of a BEC below $80 \mu\text{m/s}$ in all three spatial directions and allow for observation of the BEC after evolution times greater than 2 seconds. In this thesis the combination of a magnetically lensed rubidium 87 BEC with Double-Bragg atom interferometry will be investigated. Under gravity and in microgravity the coherence length of Bose-Einstein condensates released from different magnetic traps will be investigated. In microgravity the coherence length and wavefront distortions of magnetically lensed Bose-Einstein condensates will be studied. On ground measurements with symmetric and asymmetric Mach-Zehnder geometries will be performed. Additionally, a novel method of determining the optimal collimation of a magnetic lens with a Double-Bragg Open-Ramsey type interferometer will be presented.

Furthermore, in microgravity it is possible to implement dressed state shell potentials and confine cold atoms in two dimensions without gravity distortion leading to partially filled shells. Studying a Bose gas on a shell surface allows to investigate topology dependent vortex behavior, new collective modes, crossovers from thick to thin shells, and self-interference effects. We realize shell potentials by radio-frequency dressing the magnetic sub-states of the hyperfine ground-state $F = 2$ of rubidium 87. In this thesis measurements of thermal atoms in shell potentials in microgravity at varying positions from the atom chip, different detunings and Rabi frequencies will be presented. The results will be compared to simulations.

Key words: Atom Interferometry, Bose-Einstein Condensate, Magnetic Lensing, Shell Potentials

Contents

1	Introduction	1
1.1	Testing the Universality of Free Fall	2
1.2	Atom Interferometry	2
1.3	The QUANTUS collaboration and the Bremen Drop Tower	4
1.4	Cold Atom Clouds	5
1.5	Further Research in Microgravity	5
1.6	Structure of the Thesis	6
2	Experimental Setup	7
2.1	QUANTUS-2 Overview	7
2.2	Atom Chip	8
2.3	Fluorescence Detection	9
2.4	Absorption Imaging	9
2.5	Creating and Transporting a Bose-Einstein Condensate	10
3	Atom Interferometry	13
3.1	Theory Background	13
3.1.1	Light Atom Interaction	13
3.1.2	Bragg Diffraction	16
3.1.3	Bose Einstein Condensates	20
3.1.4	Magnetic Lens	23
3.1.5	Atom Interferometry	24
3.2	Hardware Setup and Preparatory Measurements	31
3.2.1	Atom Interferometry Setup	31
3.2.2	Atom Interferometry Laser	32
3.2.3	Spincore PulseBlaster	33
3.2.4	Atom Interferometry Laser Light Path	34
3.2.5	Transport of the Bose-Einstein Condensate	36
3.2.6	Increasing the Time-of-flight	37
3.3	Rabi Oscillations	41
3.4	Open-Ramsey Type Interferometer	46
3.5	Open-Ramsey Type Interferometer with Double Diffraction	49
3.6	Atomic Shear Interferometer	54
3.7	Asymmetric Mach-Zehnder Interferometer	58
3.8	Mach-Zehnder Interferometer	62
3.9	Summary and Conclusion	67

4 Shell Potentials	69
4.1 Physical Background	70
4.2 Hardware Setup	75
4.3 Simulation	76
4.3.1 Effects of Gravity	82
4.4 Preparatory Measurement	91
4.5 Transfer to Shell Potentials	94
4.6 Rabi Frequency	99
4.7 Detuning	102
4.8 Comparison - Gravity / Microgravity	105
4.9 Temperature Dependence	108
4.10 Lifetime	112
4.11 Summary and Conclusion	117
Bibliography	119
Appendix	133
Publications	133

CHAPTER 1

Introduction

The drive of modern physics for many decades was to develop an understanding for quantum gravity. The twentieth century physics yielded a remarkable understanding of the physical reality by describing the macroscopic world of celestial objects with the general theory of relativity (GR) and the interactions in the microscopic world with quantum physics. Both theories were verified with high precision [1, 2]. Still, many research areas in physics, such as the first fractions of a second after the big bang [3], dark energy and dark matter [4], and the inside of black holes [5] cannot solely be described by one of the two above.

One way of developing a new theory is to find limits of the old theory. Einstein's general theory of relativity is based on two postulates [6]: Einstein's field equations and the Einstein's equivalence principle (EEP). The latter states that gravity can be described as geometry and GR is a metric theory. The former postulate describes this metric. By finding limits to the EEP one would find limits to every geometric description of gravity. The EEP can be divided in three sub-principles:

- **Universality of Free Fall (UFF)**: The trajectory of any uncharged test body is independent of its internal structure and composition. Famously illustrated to the public by the Apollo 15 Commander David Scott by dropping a hammer and feather on the Moon¹.
- **Local Position Invariance (LPI)**: The outcome of any local non-gravitational experiment is independent of when and where in space the experiment was performed.
- **Local Lorentz Invariance (LLI)**: The outcome of any local non-gravitational experiment is independent of the velocity of the experimental apparatus.

These three sub-principles are related by Schiff's conjecture [7], which states that a violation of any of the three sub-principles implies a violation of the other two. To sum up, these three principles state that gravity couples universally to all types of mass and energy independent of its internal composition and charge. On the other hand, in quantum theories forces couple to a certain charge. Electrical charge in case of the electro-magnetic interaction, hyper-charge in case of the electro-weak interaction, and flavor in case of the strong interaction [8]. Thus, it is somewhat surprising that gravity couples universally without any dependence on some kind of *charge*. In this thesis, the contribution to the effort to find limits to the UFF-principle will be described.

¹ <https://moon.nasa.gov/resources/331/the-apollo-15-hammer-feather-drop/>

1.1 Testing the Universality of Free Fall

The violation of the UFF principle is quantified by the Eötvös ratio named after the Hungarian physicist Loránd Eötvös. It is the relative difference of the gravitational acceleration of two bodies g_1 and g_2

$$\eta = 2 \left| \frac{g_1 - g_2}{g_1 + g_2} \right|. \quad (1.1)$$

If the UFF principle is correct then η equals zero. So far, all experiment investigating this principle yielded a result consistent with $\eta = 0$, but with increasing precision. The UFF was tested by several methods. In the following text the most recent methods will be summed up.

Lunar laser ranging by Williams *et. al.* [9] tested the gravitational acceleration of the Earth and the Moon towards the Sun by means of reflection of laser pulses on mirrors placed on the surface of the Moon by Apollo astronauts. A precision of $\Delta\eta = 1.4 \times 10^{-13}$ was reached. Schlamminger *et. al.* [10] measured the Eötvös ratio using a rotating torsion balance. The authors measured the gravitational acceleration towards Earth of beryllium (Be) and titanium (Ti) test masses. Be and Ti test bodies of equal mass were mounted on a cylinder with the rotational axis parallel to the gravitational acceleration. A difference of g_{Be} and g_{Ti} would cause a torque on the fiber the cylinder is mounted to. A precision of $\Delta\eta = 1.8 \times 10^{-13}$ was reached. The most precise measured of the UFF principle was performed by Touboul *et. al.* [11] on the MICROSCOPE satellite mission. In that experiment a precision of $\Delta\eta = 0.9 \times 10^{-14}$ was reached. Two concentric hollow cylinders consisting of a platinum alloy and a titanium alloy were placed into orbit inside a satellite. The differential acceleration towards Earth was measured capacitively. The high precision was made possible by accurately controlling the position of the satellite with cold-gas thrusters. These three measurements were performed on macroscopic objects with either a significant difference in mass or different constituents such as beryllium and titanium. A measurement of the Eötvös ratio of free falling cold atom clouds of rubidium 85 and 87 isotopes was performed by Asenbaum *et. al.* [12]. By means of atom interferometry the differential acceleration of two cold atom clouds consisting of rubidium 85 and 87 atoms in the gravitational field with respect to a retro-reflective mirror were measured. A precision of $\Delta\eta = 3.8 \times 10^{-12}$ is one to two orders of magnitude smaller than the precision of the three other experiments. Nevertheless, the exactly known constituents of the probed objects differentiate this measurement. Moreover, measuring the Eötvös ratio with atom interferometry is comparatively new and promises significant improvements of the precision [13]. The research covered in this thesis is contributing to efforts of a collaboration funded by the *German Space Agency* to measure the Eötvös ratio of rubidium 87 and potassium 41 isotopes with a precision of 10^{-18} .

1.2 Atom Interferometry

Interferometry is a powerful tool to measure physical quantities. Recently, the first ever detection of gravitational waves was published by the LIGO and Virgo collaboration [14]. The oscillation of space was measured with an interferometer with an arm length of 4 km

and 3 km, respectively. In an interferometer a physical quantity is measured by the phase difference it induces between the two interferometer arms. Figure 1.2(a) shows a sketch of a Mach-Zehnder interferometer [15]. A laser beam initially passes a beam splitter, then it is reflected at the two mirrors and finally recombined at a beam splitter. The laser beams in the two output ports interfere constructively and destructively. A phase difference of zero between the two beams would cause full intensity in one port and zero intensity in the other port. The sensitivity of the interferometer scales with the area enclosed by the interferometer [16].

In analogy to an optical interferometer an atomic interferometer can be realized. Instead of the laser beam a cold atom cloud is used and beam splitters and mirrors are realized with laser pulses driving Rabi oscillations of the cold atom ensemble. Hence, the roles of matter and light have been interchanged. This process is illustrated in Figure 1.2(b). A phase difference between the two arms is then for example induced by a spatially varying potential. This could be the gravitational potential along the y -direction in that graph. The sensitivity of the atomic Mach-Zehnder interferometer scales as well with the enclosed area. The area can be easily calculated to $k_{eff} \cdot T^2$, where k_{eff} is the transferred momentum at the beam splitting pulse and T the time between the beam splitting and the mirror pulse. Hence, the phase sensitivity of an atomic Mach-Zehnder interferometer is

$$\Delta\Phi \sim k_{eff} \cdot T^2. \quad (1.2)$$

Thus, it follows immediately that it is beneficial to increase the time between the beam splitting and the mirror pulse. Very much in analogy to the long interferometer arms of the LIGO/Virgo interferometers. Typical table-top experiments can reach free fall times in the order of 100 ms. Asenbaum *et. al.* achieved a free fall time of 2 s by accelerating a cold atom clouds upwards in a 10 m high vacuum chamber. An experiment with a 100 m high vacuum chamber is in development at the Fermi National Accelerator Laboratory [18]. Another way of achieving free fall times of several seconds is to have the whole experimental apparatus in free fall. This is done in drop towers [19], parabolic airplane flights [20], sounding rocket missions [21], and on space-missions [22].

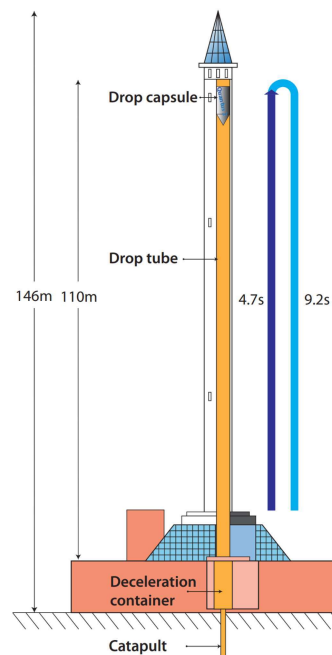


Fig. 1.1: Illustration of the drop tower. Figure taken from [17].

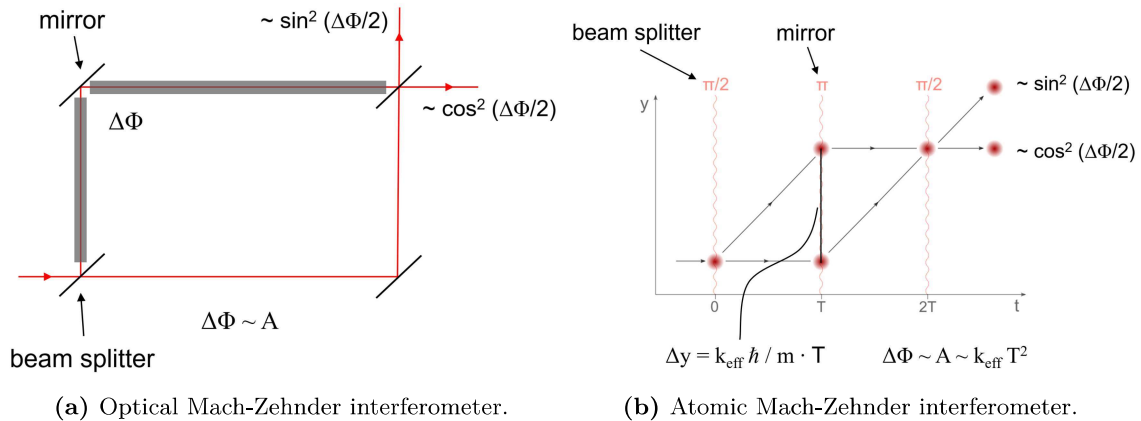


Figure 1.2: Sketch of the optical and atomic Mach-Zehnder interferometer. **a)** shows an optical Mach-Zehnder interferometer. An additional phase $\Delta\Phi$ is accumulated on the upper interferometer arm. The intensity of the two output ports depends on the accumulated phase. The sensitive to the accumulated phase is proportional to the area enclosed by the interferometer. **b)** shows an atomic Mach-Zehnder interferometer. The beam splitters and the mirror is realized with laser pulses transferring half the atomic ensemble population to an excited state or the full population to an excited state, respectively. The transferred momentum to the excited state is k_{eff} . The different interferometer arms can as well accumulate a different phase and the sensitive to the accumulated phase is proportional to the area enclosed by the interferometer: $\Delta\Phi \sim k_{eff}T^2$.

1.3 The QUANTUS collaboration and the Bremen Drop Tower

The QUANTUS¹ collaboration was funded by the *German Space Agency* since 2004. The aim of this collaboration is to perform experiments on cold atom clouds in microgravity at the drop tower in Bremen, Germany (see Figure 1.1). The drop tower facility provides a cylindrical capsule of a height of up to ~ 2 m and a diameter of ~ 0.7 m in which an experimental apparatus can be integrated. The core of the drop tower is a 110 m high vacuum chamber. The cylindrical capsules are either lifted to the top of the vacuum chamber or placed in the catapult at the bottom of the vacuum chamber. In the drop mode, when the capsule is placed at the top of the vacuum chamber, a free fall time of 4.7 s can be reached. In the catapult mode, when the capsule is accelerated upwards with 30 g from the bottom of the vacuum chamber, a free fall time of 9.2 s is reached. In the drop and the catapult mode the capsule is decelerated in a Styrofoam pebbles filled container with 40 g. The microgravity quality during the free fall reaches up to 10^{-6} g.

The QUANTUS-2 apparatus is one of the two cold atom experiment performing research in microgravity at the drop tower. Its aim is to perform simultaneous atom interferometry experiments with rubidium 87 and potassium 41 cold atom clouds in the catapult mode with an interferometer time $2T > 7$ s to test the UFF. This thesis is based on experiments performed at the QUANTUS-2 apparatus.

¹ German abbreviation for quantum gases in microgravity

1.4 Cold Atom Clouds

Long interferometer times set strict demands on the expansion rates of the cold atom clouds used for atom interferometer experiments. Previous work at the QUANTUS-2 apparatus I contributed to, but which is not part of this thesis, reduced the expansion velocity of a cold atom cloud cooled to degeneracy to below $80 \mu\text{m}/\text{s}$ in all three spatial directions. This was achieved by combining a magnetic lens [23] with quadrupole mode oscillations of the cold atom cloud [24]. The results have been submitted to the journal *Physical Review Letters* [25].

In Chapter 3 of this thesis atom interferometry experiments with unlensed and lensed rubidium 87 cold atom clouds will be covered. These experiments will present the necessary steps to perform experiments with interferometry times of several seconds. This includes

- Efficient beam splitting and mirror pulses: Reducing losses at the three Mach-Zehnder pulses and increasing detectability after long time-of-flights.
- Determination of the coherence length through self-interference allowed to investigate dephasing of cold atom clouds.
- Coherence properties of lensed cold atom clouds: It was investigated whether a magnetic lens decreases the coherence properties of cold atom clouds.
- Mach-Zehnder interferometer measurements under gravity: Allowed to compare results from dephasing of the cold atom cloud with the contrast of the interferometer.
- Identification of possible systematic effects reducing the interferometer time.

Additionally, a novel method for determining the collimation of a magnetic lens, later referred to as *atomic shear interferometer* will be presented.

1.5 Further Research in Microgravity

The emergence of platforms for cold atom research in microgravity was initially motivated by atom interferometry to utilize the long free fall times. In the wake of available tools for manipulating cold atom clouds before executing an atom interferometry sequence other areas of research opened up. The lack of gravity allows, for example, to create exactly overlapping trapping potentials for different atomic species and to study mixtures [22]. Moreover, atom lasers (matter wave analogues of the optical laser) are realized on ground by coupling out atoms from a Bose-Einstein condensate [26]. Due to gravity a vertical beam is formed. Meister *et. al.* [27] proposed an atom laser in microgravity. In contrast to the atom laser on ground the dynamics of the out-coupled atoms are only determined by repulsive interactions. The authors show that this leads to an isotropic coherent matter wave. Furthermore, the available radio-frequency sources allow to create shell potentials as proposed by Zobay *et. al.* [28]. The lack of gravity would allow to populate the shell potential homogeneously and to study self-interference effects of different parts of the shell after release from the potential [29], the dynamic of vortices on curved surfaces [30, 31], some authors even proposed investigating models of neutron stars with shell potentials [32]. In this thesis the realization of shell potentials with the QUANTUS-2 apparatus will be studied.

1.6 Structure of the Thesis

This thesis consists of two separate parts. Chapter 3 is dedicated to the atom interferometry topic and Chapter 4 will cover shell potentials. These chapters can be read independently. Chapter 2 will introduce the QUANTUS-2 apparatus and the experimental components and sequences common to the aforementioned chapters.

CHAPTER 2

Experimental Setup

The experimental context of the QUANTUS-2 apparatus was presented in the previous chapter. The experimental setup is treated in detail in References [33, 34] and the laser system in Reference [35]. This chapter will give a brief overview of the experimental apparatus. Chapters 3 and 4 will provide details on the implementation of the atom interferometry and shell potentials setup, respectively.

2.1 QUANTUS-2 Overview

The QUANTUS-2 apparatus is an atom chip based experiment with a double MOT¹ chamber made for performing atom interferometry experiments on the timescale of seconds in microgravity in the drop tower in Bremen [36]. In its final stage it will perform differential atom interferometry experiments with rubidium and potassium atoms. In its current stage only rubidium atoms are implemented. The double MOT configuration allows for loading a MOT with 10^8 atoms in 150 ms. Trapping frequencies in the range of kHz allow for fast evaporative cooling in 1 s resulting in a BEC² with 10^5 atoms. This fast BEC preparation allows for 2 consecutive experiments in the drop mode and up to 4 consecutive experiments in the catapult mode, allowing to perform 6 to 12 measurements on a day with 3 drops or catapult shots. Experiments with free time-of-flights in the range of seconds reduce the number of experiments.

The laser system was developed at the *Humboldt University of Berlin* [37] and consists of one master laser and three master-oscillator-power-amplifier (MOPA) laser with an output power of 1 W [38]. One laser is used for laser cooling of the 2D+ MOT with a laser power of up to 50 mW per beam and for the detection of the atoms. Another laser provides cooling beams with a laser power of up to 15 mW for the 3D MOT. The third laser is used as a repumper for the two MOT chambers and for the Bragg atom interferometry, where the laser power per beam is up to 20 mW.

The atom interferometry setup is configured such that it is possible to perform double Bragg diffraction. Two Bragg lattices are created with a combination of a quarter wave plate (QWP) and a mirror. The frequency detuning between the laser beams is induced by driving two *Crystal Technologies 3080-125* acusto-optical modulators (AOMs) with the *Spincore PulseBlaster DDS* frequency generator. Further details on the atom interferometry setup are provided in Section 3.2.1.

¹ Magneto-optical trap

² Bose-Einstein condensate

The whole system is controlled with a *National Instruments PXI* system. The *NI-PXI-8101* is an embedded controller running a *LabView* program. The *NI-PXI-7854R* is a FPGA providing the real-time control and read-out. Furthermore, the systems has two *NI-PXI-1428* frame grabber cards to read out two *Hamamatsu C8484-15G* CCD cameras. The *NI-PXI-6723* card has 32 analog-out channels allowing to control devices such as current drivers.

The laser system and its adjacent components are controlled by an electronics package internally developed by Thjis Wendrich called *T-STACK*. It encompasses laser diode drivers, rich-wave-guide (RW) and tapered amplifier (TA) drivers, frequency controllers, shutter drivers, frequency generation with a direct digital synthesis (DDS) for AOM control, and photo diode readout electronics. An exception is the temperature control (TEC) of the lasers, it is performed with the *Meerstetter TEC-1092* and *TEC-1091* for the master laser and the three MOPAs, respectively.

The coils and the atom chip structures are driven with the *High Finesse BCSP 10* current generators. An exception are the 2D MOT coils and the H-structure of the atom chip, it is driven by a current generator internally developed by Manuel Popp [39].

The whole system is powered by a battery platform with LiFePo4 cells developed by Tammo Sternke [40], which can power the QUANTUS-2 apparatus up to 4 h without a power supply.

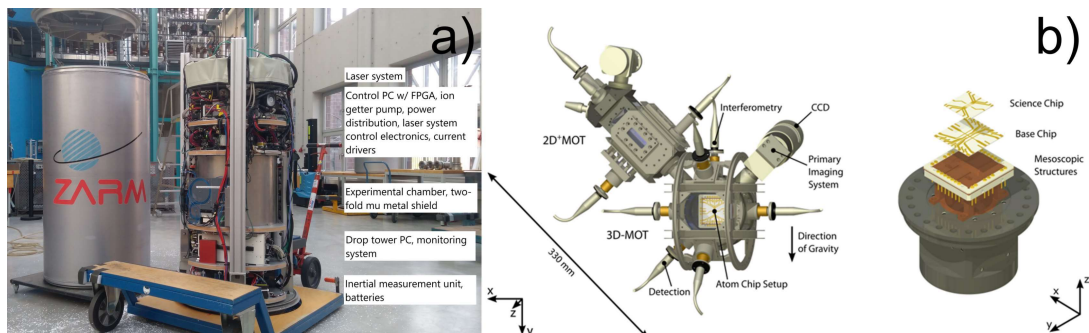


Figure 2.1: Overview of the QUANTUS-2 apparatus. **a)** shows the whole capsule on the transportation cart in the integration hall. To the left is the hull, which is put around the capsule to keep the pressure around the capsule at 1 bar in the drop tower vacuum tube. **b)** shows the QUANTUS-2 vacuum chamber and the atom chip. The system consists of a two MOT system to achieve MOT loading times of 150 ms and has a mirror MOT, which is reflected at the atom chip. The atom chip has three layers to provide functionality throughout the sequence.

2.2 Atom Chip

The atom chip is one of the main component of the QUANTUS-2 apparatus. In combination with the three Helmholtz-coil pairs it provides the magnetic fields for all trapping steps in the sequence. The use of the U-structure allows to omit large water-cooled Helmholtz-coils for the magneto-optical trap. Furthermore, another U-structure on the atom chip is connected to the National Instruments PXI-5421 arbitrary waveform generator and allows to perform evaporative cooling and create radio frequency dressed state potentials. The

atom chip is structured in three layers: the mesoscopic layer, the base chip, and the science chip (see Figure 2.2). The mesoscopic layer consists of 1 mm diameter copper wires in U- and H-configuration. The U-structure is used to create a 3D MOT and the H-structure is used for an Ioffe-Pritchard type magnetic trap. The second layer, the base chip, consists of gold structures electroplated on an aluminum nitride substrate. The Z-structure on the base chip has a wire-width of $500 \mu\text{m}$. Parallel to the horizontal part of the Z-structure are two U-wires functioning as radio frequency antennas. The base chip's Z-structure is used to create a Ioffe-Pritchard type magnetic trap and for a magnetic lens potential. The third layer is dubbed science chip and is similarly structured to the base chip, but with a wire width of $50 \mu\text{m}$ and no U-wires. It is used as well for an Ioffe-Pritchard type magnetic trap.

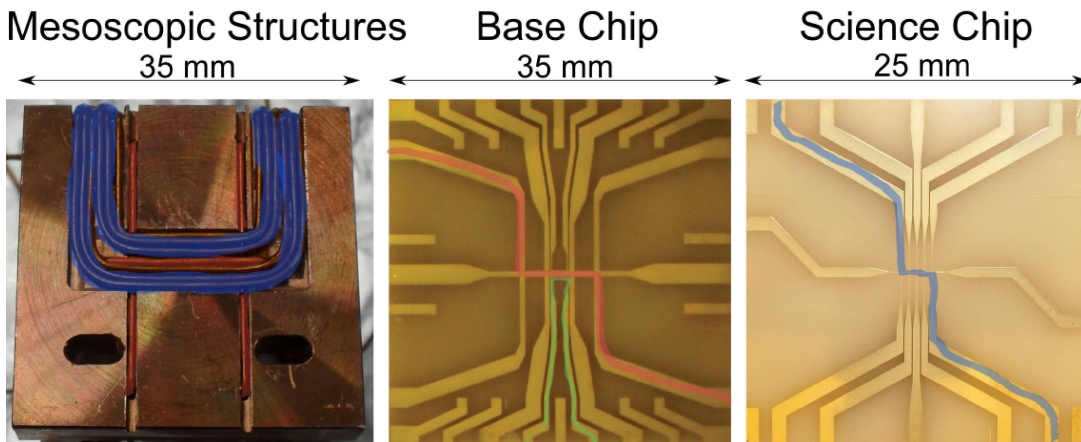


Figure 2.2: Overview of the three layers of the QUANTUS-2 atom chip. The full stack can be seen in Figure 2.1. The U-structure (blue color) on the mesoscopic structures layer contributes to the magnetic field of the MOT. The H-structure (red color) is used for realization of an Ioffe-Pritchard type magnetic trap. The Z-structure of the base chip (red color) contributes to the static Ioffe-Pritchard magnetic trap and the lower U-wire (green color) creates the RF field for evaporative cooling and for the dressed state potentials. The science chip is placed centered on the base chip. The Z-structure is used as well for the Ioffe-Pritchard magnetic trap and is indicated by the blue color. Figure adapted from [33].

2.3 Fluorescence Detection

To detect the fluorescence light of the atoms undergoing the transition $F' = 3 \rightarrow F = 2$ a lens system in front of the large window in the 3D chamber focuses the light onto Hamamatsu S5107 photodiode. The resulting photocurrent is transformed to a voltage with a transimpedance amplifier (Femto DLPCA-200). The fluorescence detection is used to monitor the performance of the experiment and as an input to the cost function of an optimization algorithm.

2.4 Absorption Imaging

The QUANTUS-2 apparatus has two imaging systems both consisting of the same setup of two achromatic lenses with $f_1 = 90 \text{ mm}$ and $f_2 = 50 \text{ mm}$ with a mirror in between to change the light path by 90° and the Hamamatsu C8484-15G CCD camera. Both are

based on the saturation absorption imaging principle [41]. The primary imaging system is tilted by 45° to the x-axis in the x-y plane. The resulting absorption images show the z-coordinates on the x-axis (later referred to as x') and a linear combination of the x- and y-coordinates on the y-axis (later referred to as y'). The secondary detection system is mounted in the x-z plane with an angle of 52.5° to the x-axis. The imaging beam is reflected on the atom chip surface before reaching the imaging system. This introduces two shadows. For the first shadow the laser beam is reflected by the atom chip and passes through the atomic cloud and for the second shadow the laser beam passes through the atomic cloud and is then reflected on the atom chip. The x-axis of secondary detection system (later referred to as x'') corresponds to a linear combination of the x- and z-coordinates and the y-axis (later referred to as y'') corresponds to the y-coordinates. Additionally, by considering the distance between the two shadows the z-coordinate can be deduced allowing to extract full 3D information of the ensemble. Furthermore, the secondary imaging system is mounted such that it can image the interference fringes resulting from atom interferometry along the y-direction.

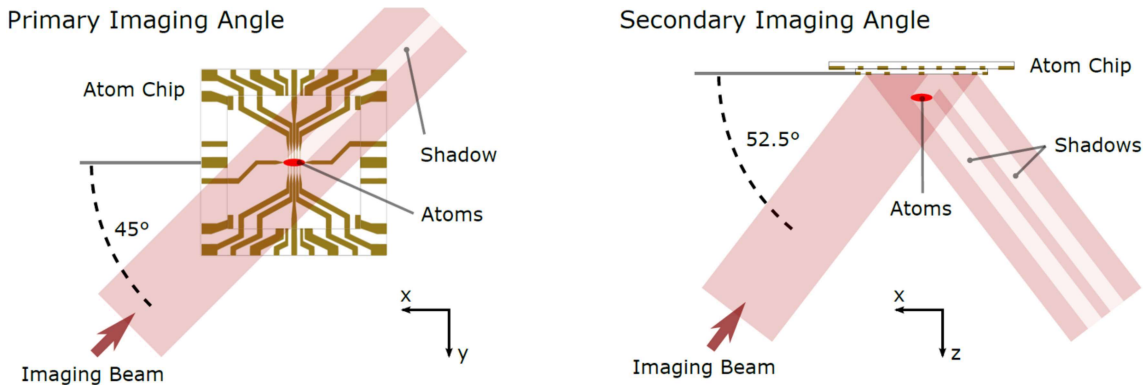


Figure 2.3: The two imaging systems of the QUANTUS-2 apparatus. The primary imaging system on the left is for precisely determining the atom number and extracting the z-position. The secondary imaging system is used for measuring the fringe spacing in atom interferometry measurements and for determining the full 3D position of the atomic cloud. Figure taken from [34].

2.5 Creating and Transporting a Bose-Einstein Condensate

This section will briefly describe the sequence used to create a Bose-Einstein condensate in chronological order and continue afterwards with transport to positions further away from the atom chip.

1. Magneto-optical trap (MOT): The MOT consists of a 2D+ MOT and a 3D MOT setup. The pre-cooled rubidium 87 beam from the 2D+ MOT is caught in the 3D MOT created by the mesoscopic U-wire and the y- and z-Helmholtz coil pairs, and four laser beams. The x-direction is cooled and trapped by two laser beams and the y- and z-direction is cooled and trapped by two laser beams reflected on the surface of the atom chip. After 150 ms the 3D MOT is loaded with $1 \cdot 10^8$ atoms and has a temperature of $200 \mu K$.

2. Compression MOT (CMOT): To transfer the atoms efficiently from the MOT to the magnetic trap it is necessary to change the position and to reduce the size of the atomic cloud. This is done by changing the magnetic field, the detuning, and the power of the laser beams by a genetic algorithm [33].
3. Optical molasses: To cool the atoms below the Doppler limit an optical molasses is applied. A temperature of $10 \mu K$ could be reached with this method.
4. Optical state preparation: To maximize the number of atoms in the magnetic trap the atoms need to be transferred to the $|F = 2, m_f = 2\rangle$ state. This is done by driving the $F = 2 \rightarrow F' = 2$ transition with σ^+ light.
5. Ioffe-Pritchard trap (IPT): The atoms are initially caught with an Ioffe-Pritchard type trap consisting of the mesoscopic H-structure and the Z-structure on the base chip plus the 3 Helmholtz-coil pairs with trapping frequencies of $(f_x, f_y, f_z) = (8, 58, 62)$ Hz. Following that, the atoms are transferred to another IPT consisting of the base chip Z-structure, the science chip Z-structure, and the x- and y-Helmholtz coil pairs closer to the atom chip with significantly higher trapping frequencies $(f_x, f_y, f_z) = (21, 1779, 1783)$ Hz. The temperature after that step increases again to $180 \mu K$.
6. Evaporative cooling: The phase space density of the atomic cloud is increased by radio-frequency induced evaporative cooling. Starting with a frequency of 23.4 MHz the exponential decrease of the frequency is approximated with seven linear ramps of the length of 100 ms to 200 ms to a frequency of 1.58 MHz. After the fourth ramp the atoms are transported to a position further away from the atom chip with trapping frequencies of $(f_x, f_y, f_z) = (24.4, 456.5, 462.3)$ Hz to increase the efficiency of the evaporation process. After the final ramp a phase space density of 2.612 is reached and $3 \cdot 10^5$ atoms remain in the condensate.
7. Transport: After the evaporation the BEC is at position $z = 209 \mu m$ dubbed position a. Another position with the advantage of being further away from the atom chip and providing a more harmonic magnetic potential is at $z = 1462 \mu m$ dubbed position c. The latter position can in contrast to position a not be realized under gravity. Other positions are a2 and b located at $z = 354 \mu m$ and $z = 813 \mu m$, respectively. They are primary used to perform experiments on ground. The four positions and their properties are listed in Table 2.1. For transport to position a2 and b sigmoid current ramps are used. A special current ramp for transport to position c was calculated by Corgier *et. al.* [42] to minimize the excitation of oscillations. More details are provided in Section 3.2.

Table 2.1: Properties of different positions dubbed *a*, *a2*, *b*, and *c*. The currents through the Z-structures of the base- and science-chip were 6 A and 2 A, respectively, for all positions. The x-coil current was 0.5 A for the positions a to b and 0.1 A for position *c*. The z-coil current was 0 A for positions *a* to *b* and -0.0038 A for position *c*. The trapping frequencies were calculated with the atom chip simulation from the group of Reinhold Walser at *TU Darmstadt* [43].

Name	y-current (A)	z-position (μm)	(f_x, f_y, f_z) in Hz
a	-1.5	209	(24.4, 456.5, 462.3)
a2	-1.1	354	(24.8, 213.3, 218.3)
b	-0.6	813	(17.5, 61.1, 59.8)
c	-0.374	1462	(9.1, 27.9, 24.6)

CHAPTER 3

Atom Interferometry

As mentioned in the introduction the method of atom interferometry allows to measure very small inertial forces [44] and to test fundamental physics [45]. The sensitivity of these measurements scales quadratically with the duration of the measurement [46]. The microgravity environment of the drop tower can be utilized to perform measurements on free falling atoms on the time scale of seconds. The long time scales set strict demands on the atomic source and the free falling experimental apparatus could disturb the measurements. This chapter will investigate a magnetically lensed Bose-Einstein condensate (BEC) as an atomic source. The focus will be put on investigating the dephasing of the BEC by measuring the coherence length. Additionally, a new method for determining the collimation of a magnetic lens will be introduced, later referred to as atomic shear interferometer.

This chapter will start with the introduction of the necessary concepts to understand atom interferometry with Bose-Einstein condensates in Section 3.1. Section 3.2 will present the experimental setup used for atom interferometry measurements. Measurements of Rabi oscillations with single diffraction Bragg pulses are shown in Section 3.3. Two beam splitting pulses are combined in Section 3.4 to perform an Open-Ramsey type interferometer. Section 3.5 will do the same for double diffraction and show first measurements in microgravity. Finally, in Section 3.6 measurements in microgravity where the magnetic lens was combined with an Open-Ramsey type interferometer are presented. Additionally, asymmetric Mach-Zehnder interferometer measurements on ground are presented in Section 3.7. In Section 3.8 a symmetric Mach-Zehnder interferometer is used to measure the gravitational acceleration along the atom interferometry axis of the QUANTUS-2 apparatus.

3.1 Theory Background

This section will introduce the necessary theoretical concepts to interpret the results of this chapter. Section 3.1.1 will introduce light atom interaction for the 1- and 2-photon case and state the resulting Rabi frequencies. Section 3.1.2 will use the results of the light atom section to introduce the concept of Bragg diffraction with a light grating for the case of single and double diffraction and discuss different diffraction regimes and pulse shapes. Finally, in Section 3.1.5 atom interferometry with light pulses will be introduced. The Open-Ramsey type interferometer and the Mach-Zehnder interferometer will be discussed.

3.1.1 Light Atom Interaction

Although, atom interferometry with 1-photon interactions are possible [47] 2- and n-photon interactions are more common due to longer lifetimes of the excited states and higher transferred momentum. This section will introduce the concept of Rabi oscillations and its

dependence on the laser power and detuning to the excited state in case of an 1-photon and 2-photon interactions.

1-photon interaction The wavelength of the laser light used for atom interferometry is typically in the visible and near-infrared range. Hence, the interaction can be described by the electrical dipole interaction:

$$\vec{E}(\vec{r}, t) \sim \vec{E}_0(\vec{r})e^{-i(\vec{k}\cdot\vec{r}-\omega t)}. \quad (3.1)$$

Additional approximations are the size of the atoms being much smaller than the wavelength of the laser light and the lack of movement of the atom during the interaction. This lead to an further simplification of for the electrical field:

$$\vec{E}(t) = \vec{E}_0e^{i\omega t}. \quad (3.2)$$

The dynamics of the system is given by the Schrödinger equation

$$i\hbar\frac{\partial}{\partial t}\psi(\vec{r}, t) = H\psi(\vec{r}, t) = (H_{atom} + H_{int}(t))\psi(\vec{r}, t), \quad (3.3)$$

with $H_{int} = -\vec{d}\cdot\vec{E}$, where \vec{d} is the electric dipole moment of the atom. This equation can be solved with an ansatz were the total wave function is a linear combination of the eigenfunctions of the two states: $e^{-i\omega_1 t}u_1(\vec{r})$ and $e^{-i\omega_2 t}u_2(\vec{r})$

$$\psi(\vec{r}, t) = c_1(t)e^{-i\omega_1 t}u_1(\vec{r}) + c_2(t)e^{-i\omega_2 t}u_2(\vec{r}), \quad (3.4)$$

where $c_i(t)$ are the time-dependent amplitudes of the two states and $\hbar(\omega_2 - \omega_1)$ their energy difference. The probability of the atom to be in the state 1 or state 2 is given by $|c_1|^2$ and $|c_2|^2$. By considering near resonant laser light ($\omega \approx \omega_2 - \omega_1$) and applying the rotating wave approximation (RWA) one gets

$$\begin{aligned} P_1 &= |c_1|^2 = \frac{1}{2}(1 + \cos\Omega_0 t), \\ P_2 &= |c_2|^2 = 1 - P_1, \end{aligned} \quad (3.5)$$

where $\Omega_0 = \langle u_2 | \vec{d} | u_1 \rangle \cdot \vec{E}_0 / \hbar$ is the Rabi frequency. For a two state system with a natural line width Γ and a saturation intensity I_{sat} the Rabi frequency is

$$\Omega_0 = \Gamma \sqrt{\frac{I}{2I_{sat}}}, \quad (3.6)$$

where I is the intensity of the laser beam. By choosing $\Omega_0 t = \pi/2$ or $\Omega_0 t = \pi$ one would transfer half the population or the full population to the excited state. This pulses are called $\pi/2$ - and π - pulses, respectively. They can be set by either adjusting the laser power or the pulse duration.

The Equation 3.5 can be modified for small detunings $\varepsilon = \omega - (\omega_2 - \omega_1) \ll \omega$. The

derivation can be found in Reference [46], resulting in:

$$P_2 = |c_2|^2 = \frac{\Omega_0^2}{2(\varepsilon^2 + \Omega_0^2)} \left(1 - \cos \sqrt{\varepsilon^2 + \Omega_0^2} t \right), \quad (3.7)$$

$$P_1 = |c_1|^2 = 1 - P_2.$$

A small detuning has two effects. It increases the oscillation frequency and reduces the amplitude of the oscillation. Off-resonant 1-photon interaction can not completely invert the population.

2-photon interaction This concept can be extended for two photon transitions and in the general case for a n-photon transition. This section will limit the discussion to 2-photon processes. Figure 3.1 illustrates the concept of one and two photon transitions. The intermediate levels are virtual states and are not populated in the process; the atom interacts simultaneously with 2 photons in a coherent process. By choosing a large enough detuning Δ to the intermediate state one reduces the losses due to spontaneous emission. The intermediate state in Figure 3.1 was chosen arbitrary. The intermediate level could also be located in between the states 1 and 2 and be used as a mean of exiting states with lower laser frequencies than the transition frequency. This effect is used for example in higher harmonic generation [48]. In this case of a 2-photon process the atom is interacting

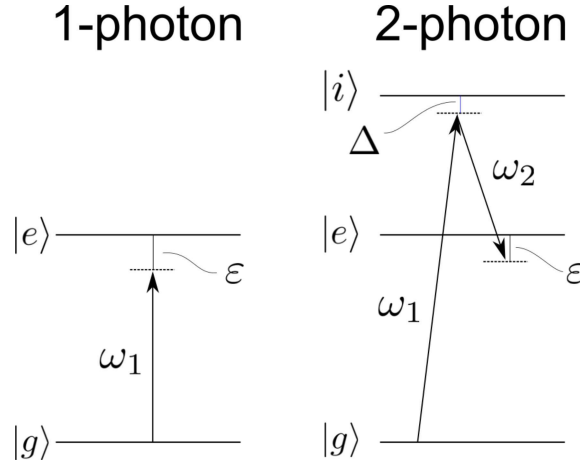


Figure 3.1: Sketch of 1- and 2-photon interactions. The transition between state $|g\rangle$ and state $|e\rangle$ in case of an 1- and 2-photon interaction is shown. The light frequencies are denoted by ω_1 and ω_2 , the detuning to the final state $|e\rangle$ is denoted by ε , and the detuning to the intermediate state $|i\rangle$ by Δ . The intermediate state $|i\rangle$ was chosen arbitrary and could be located at different position. The discussion is in the text.

with two laser beams and the electrical field is of the following form

$$\vec{E}(t) = \vec{E}_1(t) + \vec{E}_2(t) = \vec{E}_{0,1}e^{i\omega_1 t} + \vec{E}_{0,2}e^{i\omega_2 t} \quad (3.8)$$

The time-dependent population of the two states can be described by:

$$P_2(t) = \frac{\Omega_{2p}^2}{4\Omega_r^2} \sin^2 \Omega_r t, \quad (3.9)$$

$$P_1(t) = 1.0 - P_2$$

- **2-photon Rabi frequency:** $\Omega_{2p} = \frac{\Omega_{1,i}\Omega_{i,2}}{2\Delta}$, with $\Omega_{1,i}$ and $\Omega_{i,2}$ being the single photon Rabi frequencies between the state 1 and the intermediate state and the intermediate state and state 2, respectively. Δ is the detuning with respect to the intermediate state.
- **Detuning and AC-Stark shift:** $\Omega_r^2 = \Omega_{2p}^2 + (\varepsilon - \delta_{AC})^2$. Like in a 1-photon process a detuning leads to smaller amplitude and faster oscillation frequency. Additionally, the AC-Stark shifts needs to be considered, because its value is different for the two momentum states and does not cancel out like in the 1-photon process.

3.1.2 Bragg Diffraction

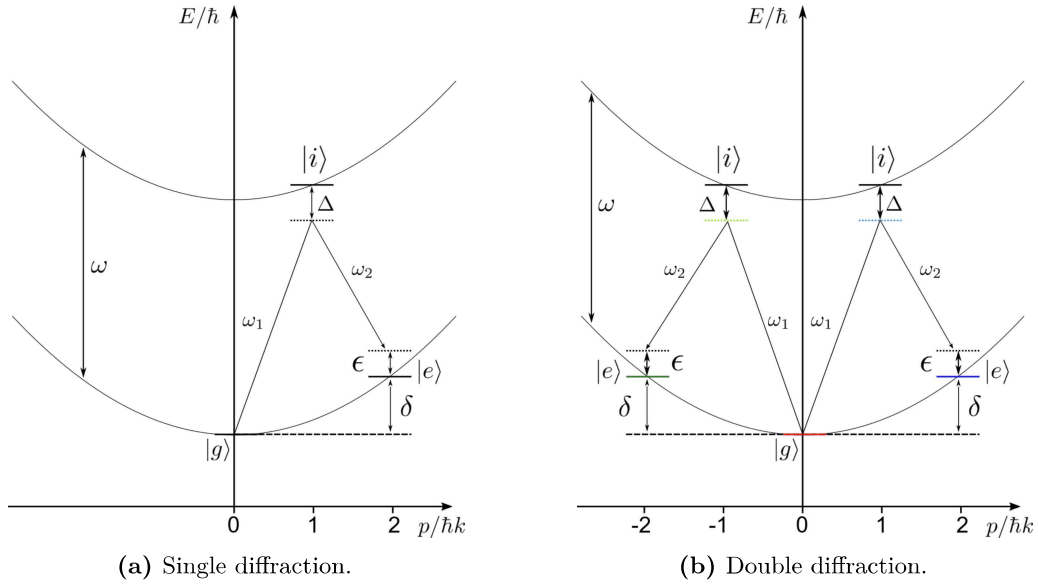


Figure 3.2: Sketch of the Bragg diffraction process. The parabolic curves show the energy dispersion of two states, e.g. $5^2S_{1/2}, F = 2$ and $5^2P_{3/2}, F = 0$. a) Two counter-propagating laser beams with a laser frequency difference of $\delta + \varepsilon$ are driving the transition between two momentum states $|g\rangle = |0\hbar k\rangle$ and $|g\rangle = |2\hbar k\rangle$ via a 2-photon process. The ground and excited states are in the same hyperfine state. If they were in a different hyperfine state the process would be called Raman diffraction. The detuning Δ to the intermediate state reduces losses due to spontaneous emission. b) A 4-photon process with two counter-propagating pairs of lasers drive a transition to the $|g\rangle = |\pm 2\hbar k\rangle$ momentum states.

2-photon processes can be for example realized by two counter-propagating laser beams. If the initial and final states were different internal states such as the $F = 1$ and $F = 2$ hyperfine states of the rubidium 87 $5^2S_{1/2}$ ground state one would call the process Raman

diffraction. If the initial and the final states are identical and only differ in the momentum one would call this process Bragg diffraction. The name stems from the analogy to the scatter process of electro-magnetic waves at a crystal structure, but in this case the roles of matter and light are interchanged. Two counter-propagating laser beams with equal frequency would create a standing wave. An incident matter-wave, such as a cold atom cloud, would be diffracted at that light-grating.

The process of scattering from the $|0\hbar k\rangle$ state via an intermediate state to the $|+2\hbar k\rangle$ momentum state is called *single diffraction* and is illustrated in Figure 3.2(a). The two parabolic curves indicate the quadratic dispersion relation of the $5^2S_{1/2}$ - and $5^2P_{3/2}$ - rubidium 87 states. The energy difference between the two states corresponds to a wavelength of 780.24 nm or a frequency of 384.23 THz. As indicated by the two different frequencies ω_1 and ω_2 a resonant transition only occurs if the two laser beams have a energy difference equal to δ . This is due to the momentum difference of the two states and the frequency difference calculates to

$$\begin{aligned} E_{final} - E_{initial} &= \frac{4\hbar^2 k^2}{2m} \\ \rightarrow \delta = \omega_1 - \omega_2 &= \frac{4\hbar k^2}{2m} = 2\pi \cdot 15.084 kHz. \end{aligned} \quad (3.10)$$

Hence, the two counter-propagating laser beams with a frequency difference δ create a moving grating, at which atoms at rest are being diffracted. A detuning ε can also be introduced, either due to a frequency difference between the two laser beams or due to residual movement of the cold atom cloud. The population of the ground and excited state in aforementioned light field is described by Equation 3.9.

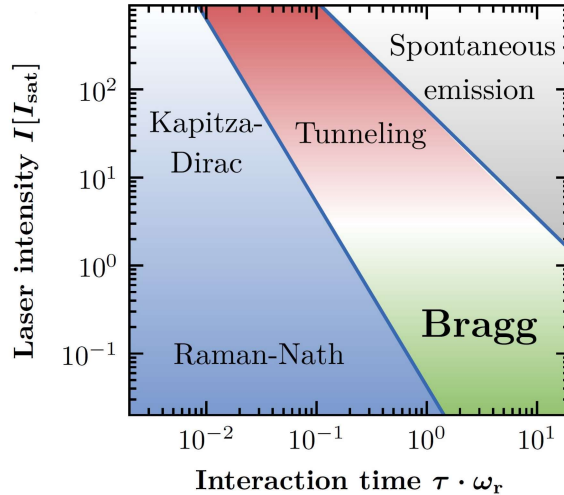


Figure 3.3: Different diffraction regimes for single Bragg diffraction. The explanation is in the text. Figure taken from [49]

Different Diffraction Regimes So far only the transitions between two states have been discussed. In a typical experimental setting the interaction times and the laser intensity have values where transitions to additional states occur. The possible regimes are shown in Figure 3.3. The Bragg diffraction regime is a special case of the Kapitza-Dirac regime [50]. In the Bragg regime the atoms are only diffracted to one excited state. This corresponds to a thick grating in the crystal analogy, or to long interaction times with a light grating. For shorter interaction times the atoms are diffracted to more than one state and this regime is called Raman-Nath. For higher laser intensities losses due to tunneling and spontaneous emission occur. The regime between the Bragg regime and the Raman-Nath regime is referred to as the quasi-Bragg regime.

Velocity selection and pulse shapes So far in the discussion of the diffraction of atoms the momentum distribution of the cold atom clouds was not considered. The momentum distribution causes different Doppler shifts over the atomic cloud, and hence, different Rabi frequencies. Thus, a laser pulse should accommodate for different momenta with an according frequency distribution. If the distribution of frequencies in the laser pulse allows to compensate for different Rabi frequencies over the atomic cloud one would speak of all *momenta being addressed*. Typically, not all momenta are being addressed and one would speak of the *velocity selection or acceptance* of the laser pulse. Hotter atomic clouds demand higher velocity acceptance, which can be realized with shorter pulses. Additionally, the different pulse shapes have difference velocity selections. To illustrate this problem one consider a 1D thermal ensemble with a temperature of $T = 20$ nK. The velocity distribution can be described by a Gaussian distribution:

$$f(v) = \frac{1}{\sqrt{2\pi}\sigma_v} e^{-\frac{v^2}{2\sigma_v^2}}, \quad (3.11)$$

where v is the velocity of the atoms and $\sigma_v = \frac{k_B T}{m}$ (k_B : Boltzmann constant, m : mass of the atoms). The above equation can be rewritten in terms of momentum $p = \hbar k$ (\hbar : reduced Planck constant, k : wave vector)

$$f(\hbar k) = \frac{1}{\sqrt{2\pi}\sigma_v} e^{-\frac{(\hbar k/m)^2}{2\sigma_v^2}}. \quad (3.12)$$

The blue curve in Figure 3.4(a) shows the momentum distribution. A Gaussian light pulse can be described by the following equation

$$g(t) = I_0 e^{-\frac{t^2}{2\sigma_t^2}}, \quad (3.13)$$

where I_0 is the peak intensity and σ_t the standard deviation of the pulse. To perform a Fourier transform and obtain a momentum acceptance in units of $\hbar k$ it is necessary to transform the time variable: $t \rightarrow t' = t \cdot m/k$. The Fourier transformed Gaussian light

pulse calculates to

$$\tilde{g}(\hbar k) = I_0 \sqrt{\frac{2\pi}{\sigma_{t'}}} e^{-\frac{(\hbar k)^2}{2\sigma_k}}, \quad (3.14)$$

with $\sigma_{t'} = \sigma_t \cdot m/k$ and $\sigma_k = 1/(2\pi\sigma_{t'})$. On the other hand, a box pulse is described by an amplitude I_0 and a width τ

$$b(t) = \begin{cases} I_0, & t \leq \frac{\tau}{2} \\ 0, & \text{otherwise} \end{cases} \quad (3.15)$$

Doing a variable transformation $t \rightarrow t' = t \cdot m/k$ and performing a Fourier transformation gives the the following equation for the box pulse

$$\tilde{b}(\hbar k) = I_0 \tau \operatorname{sinc}(\pi \tau k / m \cdot \hbar k). \quad (3.16)$$

Figure 3.4(a) show the velocity distribution of the $T = 20$ nK thermal ensemble and the Fourier transformed equations of a Gaussian and a box pulse (Equation 3.14 and 3.15) with a standard deviation of $\sigma_t = 14 \mu s$ and a box pulse width of $\tau = 14 \mu s$. The width and standard deviation were chosen such most of the momenta are being addressed. The width of the Gaussian pulse can be chosen such that it follows follows the Gaussian distribution of the atom momenta distribution, while the box pulse distribution in the momentum space looks significantly different. To address more atom momenta with a box pulse one need a shorter pulse and would increase the maximum peak power and increase losses due to spontaneous emissions. The disadvantage of box pulse is further shown in Figure 3.4(b). For the same area under the curve the box pulse has more than double the amplitude of the Gaussian pulse. Rigorous calculations have also shown that the Gaussian pulses are the preferable pulse shapes [51].

Double Diffraction The simultaneous diffraction to two opposing momentum states from a different hyperfine state was first demonstrated by Lévêque *et. al.* [52]. Simultaneous diffraction to opposing momentum states from the same hyperfine state was first proposed by Giese *et. al.* [53] and first demonstrated by Ahlers *et. al.* [54]. In this process atoms are diffracted from the $|0\hbar k\rangle$ - simultaneously to the $|\pm 2\hbar k\rangle$ - momentum states. The process was dubbed double Bragg diffraction and is a 4-photon process realized with two pairs of laser. The advantage of this method is that it doubles the sensitivity of a Mach-Zehnder interferometer by double the transfered momentum (see Equation 3.54). Furthermore, a more significant advantage is the cancellation of the laser phases in contribution of the final phase of the Mach-Zehnder interferometer [55] (see Equation 3.53 for the single diffraction case).

The $\pi/2$ -, and π -pulses are defined such that the former leads to the transfer of the population from the $|0\hbar k\rangle$ -state to the $|\pm 2\hbar k\rangle$ -states and the latter causes an inversion of the $|\pm 2\hbar k\rangle$ -states. The Rabi frequency of the double diffraction process relates to the

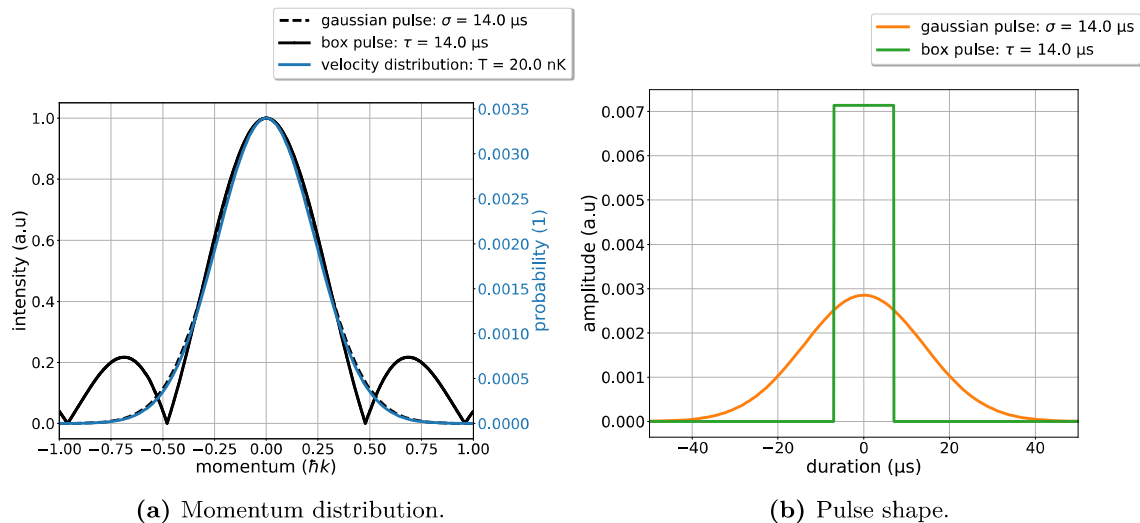


Figure 3.4: Velocity selection of different pulse shapes. a) The momentum distribution of a thermal gas with a 20 nK temperature, the velocity acceptance of a Gaussian pulse with a standard deviation $14 \mu s$, and a box pulse with a width of $14 \mu s$ are shown. The Gaussian pulse resembles the momentum distribution of the thermal gas, while the box pulse deviates significantly. b) The time profile of the pulses. The box pulse has more than a factor two higher peak amplitude leading to more losses due to spontaneous emissions, but a lower velocity acceptance.

single diffraction Rabi frequency by [55]

$$\Omega_{DD} = \Omega_{SD}/\sqrt{2}. \quad (3.17)$$

While in the single diffraction setup the atoms oscillate between two states in the double diffraction setup three states are involved. Figures 3.5(a) and 3.5(b) show the Rabi oscillations of atoms initially starting in the $|0\hbar k\rangle$ - momentum state and the $|+2\hbar k\rangle$ - momentum state, respectively. In the former case the atoms are transferred to the $|\pm\hbar k\rangle$ -momentum states by a $\pi/2$ -pulse and in the latter case half of the atoms are transferred to the $|0\hbar k\rangle$ - momentum state and 25 % to the $|\pm\hbar k\rangle$ - momentum states each.

3.1.3 Bose Einstein Condensates

The Bose Einstein Condensate (BEC) was predicted by Satyendra Nath Bose and Albert Einstein in 1924 and first realized by Eric Cornell, Carl Wiemann, and Wolfgang Ketterle in 1995 [56, 57]. In a BEC the atoms of the cold atom cloud can be described with a single wave function. The state of the BEC in an external anisotropic harmonic potential can be described by the Gross-Pitaevskii (GP) equation [58]

$$\left[-\frac{\hbar^2}{2m}\Delta + U_{ext}(\vec{r}) + Ng\psi^2(\vec{r}) \right] \psi(\vec{r}) = \mu\psi(\vec{r}), \quad (3.18)$$

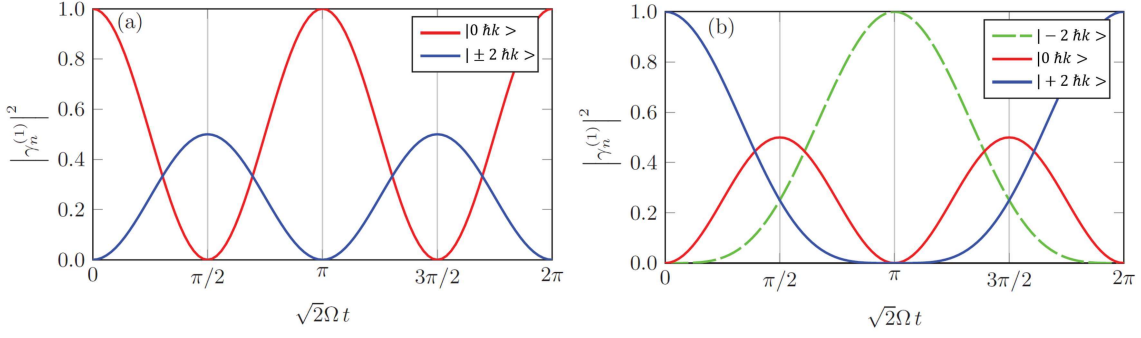
(a) Starting in the $|0\hbar k\rangle$ - momentum state.(b) Starting in the $|+2\hbar k\rangle$ - momentum state.

Figure 3.5: Double diffraction Rabi oscillations. a) Atoms initially starting in the $|0\hbar k\rangle$ - momentum state are transferred to the $|\pm 2\hbar k\rangle$ - momentum states by a $\pi/2$ -pulse, while b) atoms starting in the $|+2\hbar k\rangle$ - momentum states are transferred to the $|0\hbar k\rangle$ - momentum state (50%) and $|\pm 2\hbar k\rangle$ - momentum states (25% each) by an $\pi/2$ -pulse. Figures adapted from Reference [53]

with the interaction strength $g = 4\pi\hbar^2 a/m$, the s-wave scattering length a , the chemical potential μ , the condensate wave function $\psi(\vec{r})$, and the atom number in the condensate N . A solution to the GP equation can be found with a Hartree-Fock ansatz in case of zero temperature and is time-independent. In the regime where the atomic interactions are dominant one can neglect the kinetic energy term and use the Thomas-Fermi approximation

$$\psi(\vec{r}) \simeq \psi_{TF}(\vec{r}) = \left(\frac{\mu - U_{ext}(\vec{r})}{Ng} \right)^{1/2} \quad (3.19)$$

for $\mu \geq U_{ext}(\vec{r})$ and otherwise $\psi(\vec{r}) = 0$. The radius for an anisotropic harmonic potential with the trapping frequencies ω_i is given by [58]

$$R_i = \bar{a} \left(\frac{15Na}{\bar{a}} \right)^{1/5} \frac{\bar{\omega}}{\omega_i}, \quad (3.20)$$

where $\bar{\omega}$ the geometrical mean of the three trapping frequencies, and $\bar{a} = \sqrt{\hbar/m\bar{\omega}}$. Hence, the initial radius of the condensate is determined by the atom number N in the condensate and the individual trapping frequency. However, this equation does not describe the time-dependent behavior of the BEC such as release from the external potential and the evolution afterwards.

Scaling Approach With a generalized Hartree-Fock ansatz one can get the time-dependent GP equation

$$\left[-\frac{\hbar^2}{2m} \Delta + U_{ext}(\vec{r}, t) + Ng\psi^2(\vec{r}, t) \right] \psi(\vec{r}, t) = i\hbar \frac{\partial}{\partial t} \psi(\vec{r}, t). \quad (3.21)$$

In that case the Thomas-Fermi approximation cannot be applied, because the time variation leads to conversion of potential to kinetic energy. Due to the challenge of finding exact solutions to this nonlinear partial differential equation Y. Castin and R. Dum [59] developed the scaling approach. They started with a classical ansatz where each particle experiences a force

$$\vec{F}(\vec{r}, t) = -\nabla (U_{ext}(\vec{r}, t) + g\rho(\vec{r}, t)), \quad (3.22)$$

where $\rho(\vec{r}, t)$ is the spatial density with the condition $\rho(\vec{r}, 0) = N |\psi_{TF}(\vec{r})|$. For $t > 0$ the gas experiences a dilation described by the scaling parameters λ_1 , λ_2 , and λ_3

$$R_i(t) = \lambda_i(t) R_i(0). \quad (3.23)$$

Using Equation 3.22 and assuming a potential of the following form

$$U(\vec{r}, t) = \frac{1}{2} \sum_{i=1,2,3} \omega_i(t) r_i^2, \quad (3.24)$$

one gets three coupled differential equation, which only depend on the frequencies of the harmonic potential

$$\ddot{\lambda}_i = \frac{\omega_i^2(0)}{\lambda_i \lambda_1 \lambda_2 \lambda_3} - \omega_i^2(t) \lambda_i, \quad (3.25)$$

with the initial conditions $\lambda_i(0) = 1$ and $\dot{\lambda}_i(0) = 0$. With this results it is possible to generalize Thomas-Fermi approximation to time-dependent problems. The dynamics of macroscopic wave function is described by the three scaling parameters and the condensate density is an inverted paraboloid [59]

$$|\psi_{TF}(\vec{r}, t)|^2 = \frac{\mu - \sum_{i=1}^3 \frac{1}{2} \omega_i(0) r_i^2(0) / \lambda_i(t)}{Ng \lambda_1(t) \lambda_2(t) \lambda_3(t)}, \quad (3.26)$$

for positive values, otherwise zero.

Dephasing To obtain a description of the phase evolution of the condensate it is necessary to derive the continuity equation of the system [58]

$$\frac{\partial n}{\partial t} + \vec{\nabla}(n \cdot \vec{v}) = 0, \quad (3.27)$$

where n is the particle density and \vec{v} the velocity of the condensate. By multiplying Equation 3.21 with ψ^* and subtracting the complex conjugate of the resulting equation one arrives at

$$\frac{\partial |\psi|^2}{\partial t} + \vec{\nabla} \left[\frac{\hbar}{2mi} \left(\psi^* \vec{\nabla} \psi - \psi \vec{\nabla} \psi^* \right) \right] = 0. \quad (3.28)$$

By comparing the above equation with Equation 3.27 one gets

$$\vec{v} = \frac{\hbar}{2mi} \frac{(\psi^* \vec{\nabla} \psi - \psi \vec{\nabla} \psi^*)}{|\psi|^2}. \quad (3.29)$$

Expressing the wave function ψ in terms of an amplitude f and a phase ϕ

$$\psi = f e^{i\phi} \quad (3.30)$$

yields that the motion of the condensate corresponds to a potential flow

$$\vec{v} = \frac{\hbar}{m} \vec{\nabla} \phi. \quad (3.31)$$

Furthermore, by inserting 3.30 into 3.21 we obtain [58]

$$-\hbar \frac{\partial \phi}{\partial t} = -\frac{\hbar^2}{2mf} \nabla^2 f + \frac{1}{2} m v^2 + U_{ext}(\vec{r}, t) + N g f^2. \quad (3.32)$$

From this equation it follows that the additional contribution to the phase evolution is the external potential $U_{ext}(\vec{r}, t)$

$$\frac{\partial \Delta \phi(\vec{r}, t)}{\partial t} = -\frac{U_{ext}(\vec{r}, t)}{\hbar}. \quad (3.33)$$

By applying, for example a laser pulse of duration τ , the phase evolves according to

$$\Delta \phi(\vec{r}, t) = \frac{1}{\hbar} \int_0^\tau U_{ext}(\vec{r}, t) dt. \quad (3.34)$$

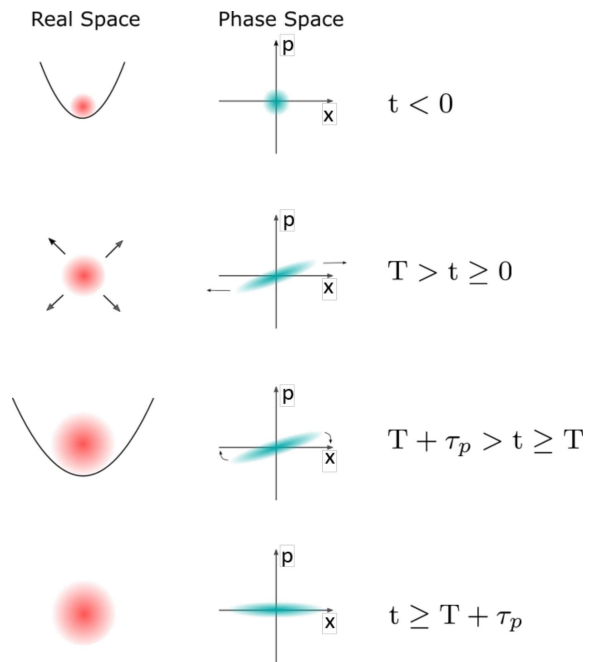
Hence, intensity variations of the laser beam over the condensate would lead to locally different phase evolution.

3.1.4 Magnetic Lens

The expansion velocity of a BEC after release depends on the trapping frequencies of the trap and the total atom number of condensed and non-condensed atoms [58, 59]. In case of atom interferometry, as will be explained in the next section, it is desirable to observe BECs several seconds after the release from the magnetic trap. This requires expansion velocities in the range of 100 $\mu\text{m/s}$ [25]. A microgravity environment is suited for very low trapping frequencies in the range of 1 Hz. Leanhardt *et. al.* [60] demonstrated the reduction of the geometric mean of the trapping frequencies to $\bar{\omega} = 2\pi \times (1.12 \pm 0.08)$ Hz by compensating gravity with a vertical bias field. This process took 25 s due to the slow long collisional equilibrium time. The authors further reduced the temperature of the BEC by reducing the atom number to 2500 through a long hold time in the trap of around 200 s. The resulting temperature was (450 ± 80) pK and the thermal velocity around 1 mm/s. This method is not viable in the drop tower due to the limited experimental time of 4.7 s in the drop mode and due to the need for higher atom numbers. Alternatively,

the expansion velocity of an atomic ensemble can be reduced by applying a well timed harmonic potential on a freely expanding ensemble as proposed by Ammann *et. al.* [23]. The basic idea is that after sufficiently long time of flights T the momentum will be a linear function of the position: $p = mx/T$, where m is the mass of the atoms. If the atoms are still located in a region where an approximately harmonic potential $U(x) \approx m\omega^2 x^2/2$ can be applied for a short period of time τ than it is possible to reduce the momenta of the atoms to almost zero due to the force on the atoms being proportional to the position: $\Delta p \propto dU/dx \propto x \propto p$. The velocity of the atoms after the application of the potential will not be zero for two reasons. First, the relation $p = mx/T$ is only approximately fulfilled for long time-of-flights T and second, potentials are only approximately harmonic in a certain region. Hence, a trade-off between the two factors needs to be made. Figure 3.6 shows an illustration of the process and in the aforementioned source a rigorous treatment of the process can be found. This method is often referred to as *magnetic lensing* or as the original authors referred to *delta kick cooling*.

Figure 3.6: Illustration of the magnetic lensing process. The atomic cloud is at time $t < 0$ confined in a magnetic potential. The atoms are released from the trap at time $t = 0$ and are expanding freely for a time period of T . After a sufficient long time-of-flight the momentum of the atoms is a linear function of space $p = mx/T$. In the phase space representation this corresponds to stretching of the cloud. At time $t = T$ a harmonic potential is applied for a time period of τ_p and the system is described by $H = p^2/2m + \Pi(\frac{t-T}{\tau_p} - \frac{1}{2})V(x)$, where Π is the Heaviside function and $V(x) \approx m\omega^2 x^2/2$ an approximately harmonic potential. The momentum transferred to the atoms is proportional to the momentum of the atoms due to the linear relation between momentum and position: $\Delta p \propto dU/dx \propto x \propto p$. More details are in the text.



3.1.5 Atom Interferometry

In this section the atom-light interaction and Bose-Einstein condensates will be combined to realize atom interferometers. In analogy to optical interferometers, atom interferometers consist of beam splitters and mirrors, but utilize laser light to split or reflect atomic clouds. Atom interferometers allow to probe the atomic clouds, such as Bose-Einstein condensates, or to measure external properties such as gravity or acceleration.

First, the Open-Ramsey type interferometer will be introduced. It allows to probe the properties of the used atomic source. Second, the Mach-Zehnder interferometer will be discussed, which allows to probe external properties. At last, the asymmetric Mach-

Zehnder interferometer will be treated. This interferometer geometry is a combination of an Open-Ramsey type and Mach-Zehnder interferometer and allows to probe the properties of the atomic source after a Mach-Zehnder sequence.

Open-Ramsey type interferometer The Open-Ramsey type interferometer consists of two $\pi/2$ -pulses separated by an interrogation time T_{int} . A Sketch of the geometry in case of single diffraction is shown in Figure 3.7 and in case of double diffraction in Figure 3.8. Initially, only the single diffraction case will be discussed. As a source of cold atoms Bose-Einstein condensates will be considered. The first $\pi/2$ -pulses causes the cold atom cloud to separate in the momentum states $|0\hbar k\rangle$ and $|+2\hbar k\rangle$. The second $\pi/2$ -pulse splits both momentum states again in the $|0\hbar k\rangle$ - and $|+2\hbar k\rangle$ -states. By choosing the interrogation time such that there is still an overlap of the wave functions at the second $\pi/2$ -pulse the two output ports after a time-of-flight will consists of two overlapping condensates whose center-of-mass is separated by $2\hbar k T_{int}$. This will cause interference of the condensates and fringe patterns will be visible in the absorption images.

The fringe spacing can be calculated by using the scaling approach introduced prior in this chapter. The wave function of a Bose-Einstein condensate can be expressed as: $\psi(x) = f(x) e^{i\phi}$, where $\phi = \alpha x^2 + \beta x$. $\alpha = \nabla^2 \phi$ describes the mean-field expansion of the wave packet and β its center-of-mass motion. The fringe pattern can be calculated by evaluating the density $|\psi_A(x) + \psi_B(x + \delta x)|^2$ for two condensates A and B separated by a distance δx .

$$|\psi_A(x) + \psi_B(x + \delta x)|^2 = |\psi_A(x)|^2 + |\psi_B(x + \delta x)|^2 + 2\text{Re}[\psi_A^*(x) \psi_B(x + \delta x)]. \quad (3.35)$$

Evaluating the cross-term will give us the fringe pattern [61]

$$\begin{aligned} 2\text{Re}[\psi_A^*(x) \psi_B(x + \delta x)] &= 2\sqrt{f_A(x)f_B(x + \delta x)} \text{Re}\left[e^{i(-\phi_A(x) + \phi_B(x + \delta x))}\right] \\ &= 2\sqrt{f_A(x)f_B(x + \delta x)} \cos(\kappa x + \phi_0), \end{aligned} \quad (3.36)$$

where $\phi_0 = \alpha \delta x^2 + \beta \delta x$ is a constant phase and $\kappa = 2\alpha \delta x + 2\beta$ the spatial fringe frequency. Thus, the fringe spacing is given by

$$d = \frac{2\pi}{2\alpha \delta x^2 + 2\beta}. \quad (3.37)$$

Taking the time-derivative of Equation 3.23 and inserting the initial radius in the expression for the velocity gives

$$v_i(\vec{r}, t) = r_i \frac{\dot{\lambda}_i(t)}{\lambda_i(t)}. \quad (3.38)$$

Taking Equations 3.38 and 3.31 together we get an expression for α

$$\alpha(t) = \frac{m}{\hbar} \frac{\dot{\lambda}_i(t)}{\lambda_i(t)} \quad (3.39)$$

Neglecting the relative velocity of the two wave packets leads to the following expression for the fringe spacing

$$d(t) = \frac{h}{m\delta x} \frac{\lambda_i(t)}{\dot{\lambda}_i(t)}. \quad (3.40)$$

Hence, the fringe spacing depends on the trapping frequencies of magnetic trap. In the QUANTUS-2 experiment the atom interferometry beams align with the radial axis of the Ioffe-Pritchard trap ($\omega_{rad} \gg \omega_{axial}$) and the scaling parameters can be expressed in term of the radial trapping frequency

$$\lambda_{rad} = \sqrt{1 + (\omega_{rad}t)^2}. \quad (3.41)$$

In the far-field the fringe spacing can be approximated by

$$d = \frac{h \cdot T_{TOF}}{m \cdot \delta x}, \quad (3.42)$$

where $\delta x = 2k\hbar T_{int}$ in case of single diffraction and $\delta x = 4k\hbar T_{int}$ in case of double diffraction. T_{TOF} is the total time-of-flight after release from the magnetic trap.

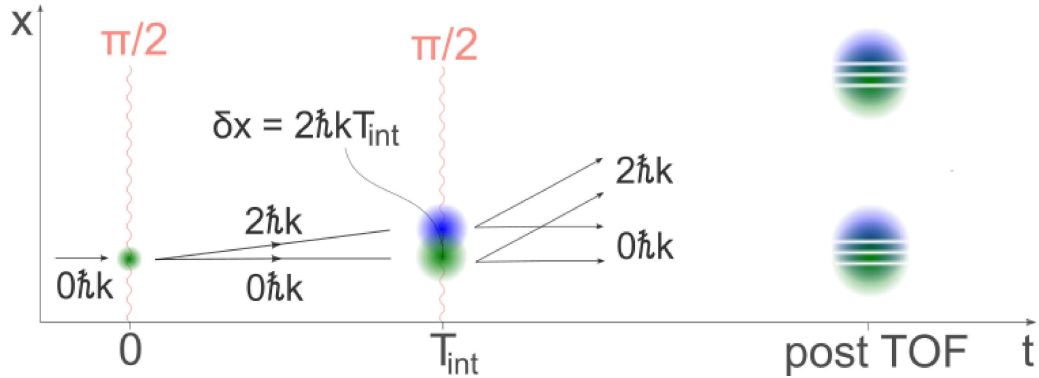


Figure 3.7: Sketch of an Open-Ramsey type interferometer with single diffraction. At $t = 0$ a $\pi/2$ - pulse is applied and transfers 50 % of the population into the $2\hbar k$ momentum state. After a time of T_{int} another $\pi/2$ - pulse is applied. At that time the center of mass distance of the two clouds is $2\hbar k \cdot T_{int}$. After sufficient time of flight the two clouds are separated enough to be distinguished. An interference pattern with a fringe spacing proportional to $1/(2 \cdot T_{int})$ can be observed.

In case of double diffraction and non-perfect transfer to the $\pm 2\hbar k$ states atoms remain in the the state $0\hbar k$ and are again at $t = T_{int}$ not perfectly transferred to the states $\pm 2\hbar k$. This leads to three different overlapping clouds at the three output ports. Two of them have a center-of-mass difference of $4\hbar k \cdot T_{int}$, but the third cloud has only a center-of-mass difference to the other clouds of $2\hbar k \cdot T_{int}$ leading to a fringe spacing proportional to $1/(2 \cdot T_{int})$.

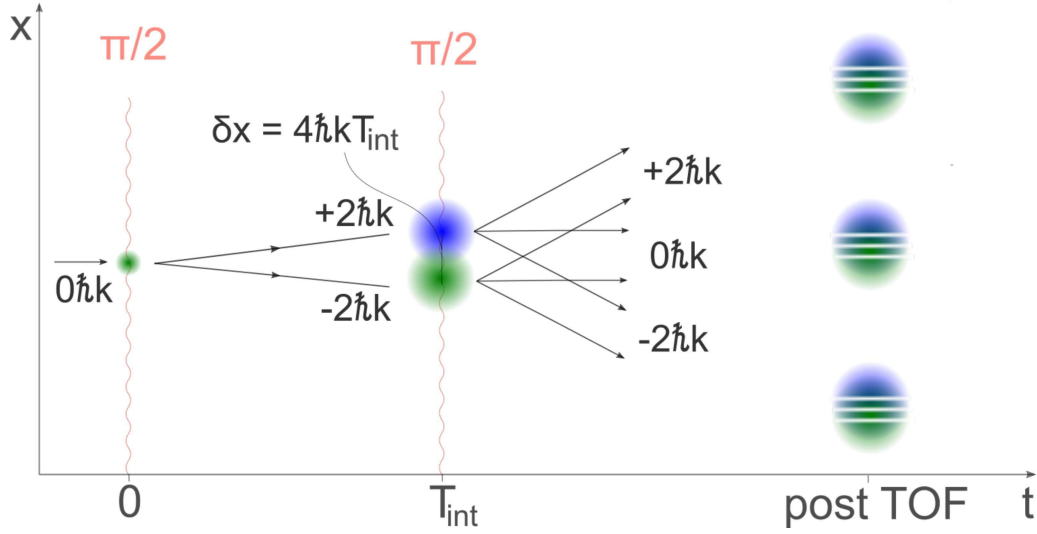


Figure 3.8: Sketch of an Open-Ramsey type interferometer with double diffraction. A double diffraction $\pi/2$ -pulse (4-photon process) transfers the atoms to the $\pm 2\hbar k$ momentum states. After a time of T_{int} another $\pi/2$ -pulse distributes the atoms to the $\pm 2\hbar k$ and $0\hbar k$ states. After a sufficiently long time of flight the three output ports are separated and interference with a fringe spacing proportional to $1/(4 \cdot T_{int})$ is visible.

Mach-Zehnder Interferometer The Mach-Zehnder (MZ) interferometer (sketch in Figure 3.9) is aside from the Michelson interferometer one of the most popular interferometer geometries used. The interferometer starts with a beam splitter, two mirrors to redirect the two interferometer arms, and a final beam splitter to recombine the two interferometer arms. The phase difference between the two interferometer arms is read out through the intensity difference in the two output ports.

This interferometer geometry can also be realized with an atom interferometer. The initial and final beam splitter is implemented by a $\pi/2$ - pulse and the two mirrors with one π - pulse. The pulse sequence looks as follows: $\pi/2 - \pi - \pi/2$. The time between the pulses should be equal and is denoted by T .

In Section 3.1.1 the spatial extent of the light beam was neglected. For the purpose of a Mach-Zehnder interferometer the interaction of the cold atom clouds with different relative phases of the light field needs to be considered, because a) the size of the atom cloud spans many wave length and b) the de Broglie wavelength of the atomic source exceeds the wave length of the used light source. Finally, the population of the output ports of the MZ interferometer depends on the phase difference between the two interferometer arms and subsequently the phase of the light field needs to be taken into account.

Analogue to the ansatz for Equation 3.4 the wave function at a time t_0 of a two level system can be expressed as

$$|\Psi(t_0)\rangle = c_e(t_0) |e\rangle + c_g(t_0) |g\rangle. \quad (3.43)$$

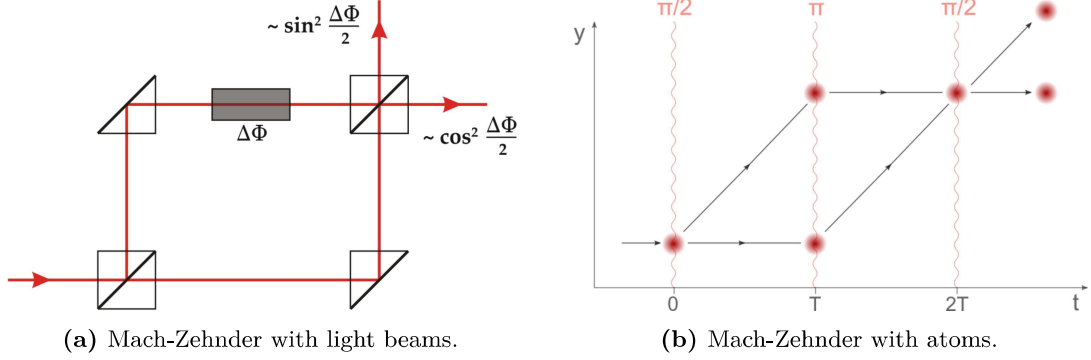


Figure 3.9: a) Sketch of a Mach-Zehnder interferometer with light beams. The setup consist of a beam splitter, two mirrors, and a final beam splitter two recombine the beams again. The intensity at the two output ports is proportional to the phase difference between the two interferometer arms. (The image was taken from Wikipedia). b) Sketch of a Mach-Zehnder inteferometer with atoms. The beam splitters are realized with $\pi/2$ -pulses and the two mirrors are realized with one π -pulse. The sketch represents an interferometer in microgravity due to the linear motion of the atomic clouds.

The probabilities c_e and c_g after a light pulse of length τ are calculated in [46] and are

$$c_e(t_0 + \tau) = e^{-i\delta\tau/2} \left\{ c_e(t_0) \left[\cos\left(\frac{\Omega_r\tau}{2}\right) - i \cos\theta \sin\left(\frac{\Omega_r\tau}{2}\right) \right] + c_g(t_0) e^{-i(\delta t_0 + \phi)} \left[-i \sin\theta \sin\left(\frac{\Omega_r\tau}{2}\right) \right] \right\} \quad (3.44)$$

and

$$c_g(t_0 + \tau) = e^{-i\delta\tau/2} \left\{ c_e(t_0) e^{i(\delta t_0 + \phi)} \left[-i \sin\theta \sin\left(\frac{\Omega_r\tau}{2}\right) \right] + c_g(t_0) \left[\cos\left(\frac{\Omega_r\tau}{2}\right) + i \cos\theta \sin\left(\frac{\Omega_r\tau}{2}\right) \right] \right\}, \quad (3.45)$$

where δ is the detuning, Ω_r the off-resonant Rabi frequency, $\sin\theta = \Omega_0/\Omega_r$ the ratio of the resonant and off-resonant Rabi frequency, and $\cos\theta = -\delta/\Omega_r$ the ratio of the detuning to the off-resonant Rabi frequency.

For a detuning much smaller than the off-resonant Rabi frequency, the probabilities for $\pi/2$ - and π -pulses of a duration of $\tau/2$ and τ , respectively, can be expressed as

$$\begin{aligned} c_e(t_0 + \tau) &= -i c_g(t_0) e^{-i\delta\tau/2} e^{-i(\delta t_0 + \phi)} \\ c_g(t_0 + \tau) &= -i c_e(t_0) e^{i\delta\tau/2} e^{i(\delta t_0 + \phi)} \end{aligned} \quad (3.46)$$

and

$$\begin{aligned} c_e(t_0 + \tau/2) &= e^{-i\delta\tau/4} \left[c_e(t_0) - ic_g(t_0)e^{-i(\delta t_0 + \phi)} \right] / \sqrt{2} \\ c_g(t_0 + \tau/2) &= e^{i\delta\tau/4} \left[-ic_e(t_0)e^{i(\delta t_0 + \phi)} + c_g(t_0) \right] / \sqrt{2}. \end{aligned} \quad (3.47)$$

The probabilities after a MZ interferometer with a $\pi/2 - \pi - \pi/2$ pulse sequence can be calculated by successive application of Equation 3.46 and 3.47. The first $\pi/2$ -pulse is applied at t_1 , the π -pulse at $t_2 = T + \tau/2 + t_1$, and the second $\pi/2$ -pulse at $t_3 = 2T + 3/2\tau + t_3$ resulting in

$$c_e(t_3 + \tau/2) = -\frac{i}{2} e^{-\delta\tau/2} e^{-i[\delta t_2 + \phi(t_2)]} (1 - e^{i\delta\tau/2} e^{-i\Delta\phi}), \quad (3.48)$$

where

$$\Delta\phi = \phi(t_1) - 2\phi(t_2) + \phi(t_3), \quad (3.49)$$

where $\phi(t_i)$ are the phases of light at time t_i in reference to a fixed point in space. This reference is for example the retro-reflective mirror in the QUANTUS-2 experiment and the phase shifts are measured in reference to this point. The probability of finding the atoms in the excited state is then

$$|c_e(2T + 2\tau)|^2 = \frac{1}{2} [1 - \cos(\Delta\phi - \delta\tau/2)]. \quad (3.50)$$

For $\delta = 0$ this looks exactly like on of the output ports in Figure 3.9. Furthermore, if no forces are acting on the atoms and the detuning does not change during the sequence we get $\Delta\phi = \delta\tau/2$ and all atoms are in the ground state after the full MZ sequence. The next section will explain how external forces, like gravitational acceleration, are changing the result.

Sensing with a Mach-Zehnder interferometer The basic principle behind sensing inertial forces with atom interferometry is the change of the matter wave phase relative to the driving field, which is fixed to the experimental chamber. The experimental chamber, or more precisely, the retro-reflective mirror is the local reference frame.. The change of the phase of the matter wave leads to a change in the number of atoms. Accordingly, measuring the fraction of the number of atoms in the excited states to the total number of atoms yields the phase change [46].

In a Mach-Zehnder interferometer a three pulse sequence is executed: $\pi/2 - \pi - \pi/2$. The frequency shift of the driving field shifts in the rest frame of the atoms with $-\vec{k}_{eff} \cdot \vec{g}t$, where \vec{k}_{eff} is the effective wave vector of the driving field ($\vec{k}_{eff} = 2\vec{k}$ in case of single diffraction) and \vec{g} the acceleration vector showing in the direction of gravity. This effect can be incorporated into Equation 3.49. The linear increase in the detuning leads to a

effective phase at time t_n of the tree pulses

$$\phi_n = - \int_{t_0}^{t_n} \vec{k}_{eff} \cdot \vec{g}t' dt'. \quad (3.51)$$

The overall phase shift $\Delta\phi = \phi_1 - 2\phi_2 + \phi_3$ calculates for a pulse separation of T to

$$\Delta\phi = -\vec{k}_{eff} \cdot \vec{g}T^2. \quad (3.52)$$

One could perform a phase-continuous sweep of the synthesizer frequency $\omega(t) = \omega_0 + \alpha(t - t_0)$, where ω_0 is the frequency at the $\pi/2$ - pulse time t_0 . Therefore, the effective phases at the free pulses are the following

$$\begin{aligned} \phi_1(t_0) &= \omega_0 t_0 - \vec{k}_{eff} \cdot \vec{g}t_0^2 + \phi_0 \\ \phi_2(t_2) &= (\omega_0 + \alpha(t_2 - t_0))t_2 - \vec{k}_{eff} \cdot \vec{g}t_2^2 + \phi_0 \\ \phi_3(t_3) &= (\omega_0 + \alpha(t_3 - t_0))t_3 - \vec{k}_{eff} \cdot \vec{g}t_3^2 + \phi_0, \end{aligned} \quad (3.53)$$

where ϕ_0 is the initial phase of the synthesizer and ω_0 the resonance frequency of the first $\pi/2$ - pulse. This leads to a phase shift in the rest frame of the atoms of

$$\Delta\phi = (\alpha - \vec{k}_{eff} \cdot \vec{g})T^2. \quad (3.54)$$

For $\alpha = \vec{k}_{eff} \cdot \vec{g}$ the phase shift is zero and the gravitational acceleration is compensated by the frequency sweep. Hence, the atoms are in the ground state after the second $\pi/2$ -pulse.

For a measurement determining the gravitational acceleration one would perform a scan of the frequency sweep rate α for at least two interrogation times T to determine the correct fringe and then do an integration measurement at that fringe.

Asymmetric Mach-Zehnder interferometer The Open-Ramsey type interferometer allows to test whether there is a stable phase on the Bose-Einstein condensate at a point in time. During a Mach-Zehnder interferometer sequence dephasing could occur in the different interferometer arms. For example by an interaction with a potential, which has a spatial variation in the order of the size of the BEC. This would lead to dephasing as described by Equation 3.34 and to a loss of contrast in the symmetric Mach-Zehnder interferometer. The dephasing could be tested by scanning the α parameter in Equation 3.54 and determining whether a sinusoidal oscillation is observable. Due to number of daily drops limited to 3 at the drop tower the scanning of the oscillation would take at least a week. Moreover, drop to drop variations in BEC's velocity, capsule rotation, Bragg diffraction efficiency, and other sources could reduce the contrast. A method to test whether dephasing is occurring during the interferometry sequence and whether the BECs of the two interferometer arms are still coherent is the asymmetric Mach-Zehnder interferometer (see Figure 3.10). With this method it is possible to probe the coherence of the two arms of a Mach-Zehnder interferometer with one measurement. In difference to a symmetric Mach-Zehnder interferometer the second $\pi/2$ -pulse is applied δt seconds

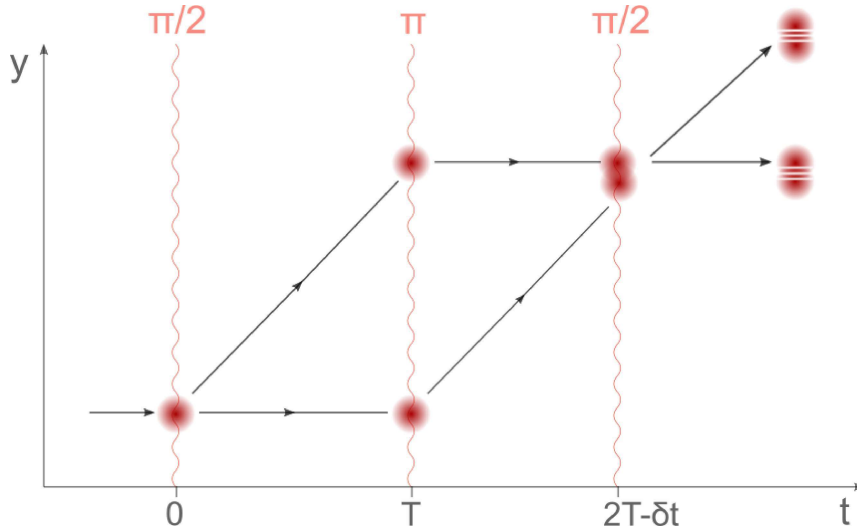


Figure 3.10: Sketch of an asymmetric Mach-Zehnder interferometer. In contrast to a symmetric Mach-Zehnder interferometer the last $\pi/2$ -pulse is applied δt earlier. At that point the two momentum states are not overlapping completely and are having a center of mass distance of $2\hbar k\delta t$. After application of the second $\pi/2$ -pulse the center of mass difference is transferred to the two output ports.

earlier. This resembles the second $\pi/2$ -pulse of an Open-Ramsey type interferometer (see Figure 3.7) with $T_{int} = \delta t$. Due to the earlier $\pi/2$ -pulse the two BECs are not overlapping completely and the output ports show an interference pattern in case of coherence between the two interferometer arms. The fringe spacing of the interference pattern is described by the same equation as for the Open-Ramsey type interferometer with $T_{int} = \delta t$ (see Equation 3.42).

3.2 Hardware Setup and Preparatory Measurements

This section will provide information on the necessary setup to perform atom interferometry and show measurements to quantify the possible systematic errors. Section 3.2.1 will give an overview of the whole setup. Section 3.2.2 will focus on the frequency control of the lasers and the occurring systematic errors. Afterwards, Section 3.2.3 will discuss the frequency generation and control of the acousto-optic modulators. Section 3.2.4 will present the light path of the atom interferometry beams and investigate the phase stability of the laser beams. Finally, Section 3.2.5 will describe the transport of Bose-Einstein condensates in microgravity conditions.

3.2.1 Atom Interferometry Setup

The main parts of the atom interferometry setup were the Schäfter & Kirchhoff 60FC-4-A18-02 collimator with a beam diameter¹ of 3.31 mm, the Thorlabs BB1-E03P mirror, and the Lambda Research Optics WPO-25.4CQ-0-4-780 quarter wave plate (QWP). Figure

¹ $1/e^2$ diameter

3.11 shows the setup around the vacuum chamber. The AI beam axis is tilted by 7° to the vertical axis to avoid standing waves from reflection at the mirrors indicated in the aforementioned figure. The collimator was placed in a custom designed holder, which can be moved in the z-direction. A custom made holder allowed to rotate the QWP by 90° and be fixed with locking screws for the drop. The QWP and the mirror were fixed to tip-tilt stage, which allowed to adjust the pitch and yaw and fix them with locking screws for the drop. The residual light passing through the mirror was reflected by two mirrors into an avalanche photo diode (*Hamamatsu C12703*) to monitor the AI laser pulses (see Figure 3.11 for sketch and 3D animation of the setup).

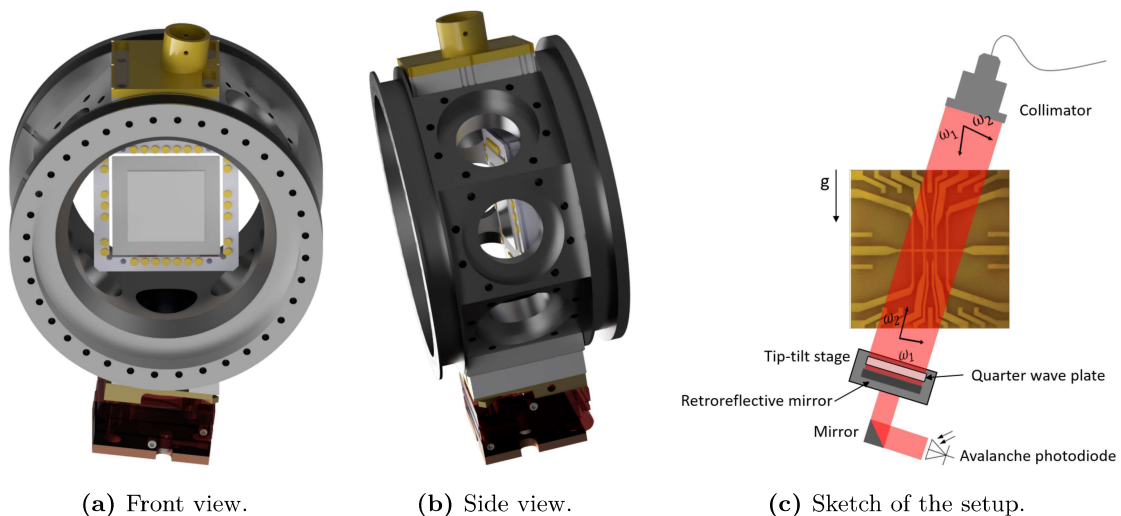


Figure 3.11: The atom interferometry setup. **a)** and **b)** show the bare 3D chamber with the atom-chip inside. Gravity points down along the vertical edge of the atom-chip. On top of the chamber is the collimator holder for the atom interferometry beam (indicated with the color gold). On the other side of the vacuum chamber is the QWP holder (indicated in brass color), the tip-tilt stage (indicated in red), and the mirror hold (indicated in copper). At the bottom of the mirror holder is a cut-out to collect residual light with an avalanche photo diode. The different colors are for indication. The mentioned components are made of aluminum. **c)** shows a sketch of the atom interferometry setup. Laser light of two different frequencies ω_1 and ω_2 from the two axis of a polarization maintaining single mode fiber is coupled out, passes the atom chip, and is reflected at the retro-reflective mirror. The polarization is rotated by 90° with the combination of the retro reflective mirror and the quarter wave plate. The tip-tilt stage makes sure that the k-vector of the reflected beam is parallel to the k-vector of the incident beam. The residual light passing the retro reflective mirror is redirected with a mirror to an avalanche photodiode to monitor the laser light.

3.2.2 Atom Interferometry Laser

Due to restricted space in the capsule no dedicated Bragg laser was used. Instead the MOPA2 laser, which is normally utilized as a repump-laser for the D2 $F = 1 \rightarrow F' = 2$ transition, was repurposed during the sequence. The challenge is to change the MOPA2 frequency during the sequence by 5 GHz. This is necessary, because the MOPA2 frequency is 6.568 GHz above the D2 $F = 2 \rightarrow F' = 3$ transition and to achieve π -pulses with the

available laser power we need a detuning of around 1 GHz. The Thijs frequency regulation card is only capable to change the laser frequency by 1 GHz. For that reason, the card was modified with a current-by-pass consisting of a MOSFET transistor activated by a TTL signal to bypass 1.25 mA to 1.50 mA, and hence, reducing the frequency of the MOPA2 by around 5 GHz.

The beat between the master laser and the MOPA2 was measured with the *Rohde & Schwarz FSH8* spectrum analyzer with and without the current-by-pass 10 times, alternately. Figure 3.12 shows the resulting frequencies. The current-by-pass lowered the frequency by 5300 ± 41 MHz. The detuning to the intermediate state was 1268 ± 41 MHz (relative error of 3.2 %).

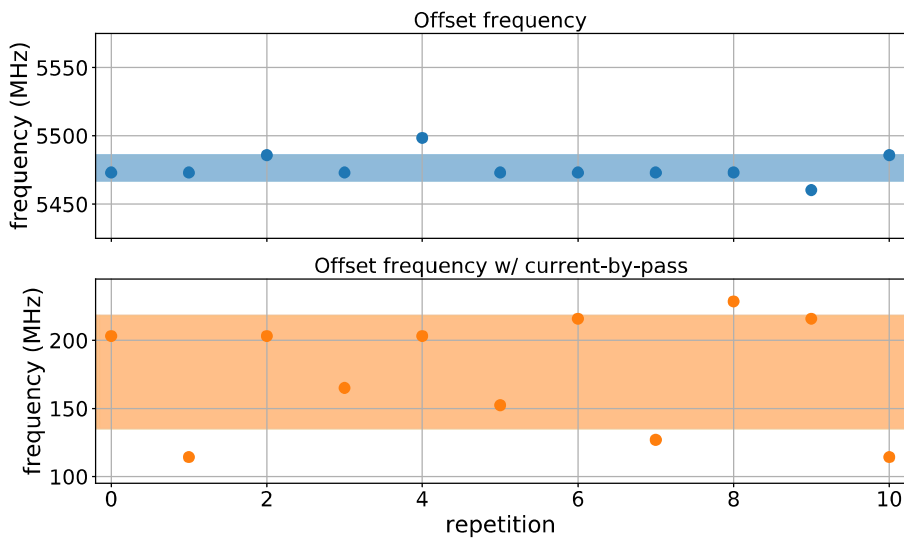


Figure 3.12: Measurement of the offset frequency with the current-by-pass. The frequency of the MOPA2 laser beat was measured with the *Rhode & Schwarz FSH8* spectrum analyzer. Alternately, the frequency without and with the current-by-pass was measured. The shaded area indicates the 95 % confidence interval. The current-by-pass lead to a frequency jump of 5300 ± 41 MHz.

3.2.3 Spincore PulseBlaster

The frequency difference in the kHz range between the two AI laser beams were created with the Spincore PulseBlaster DDS frequency generator. The output of the two channels of the DDS were smoothed with two *Mini-Circuits SLP-100+* 98 MHz low pass filter. The frequency of the two output channels were set to 100 MHz and 100 MHz plus the necessary detuning (e.g 15.084 kHz in case of resonant Bragg diffraction). The two output channels were combined with the Thijs DDS in the *Mini-Circuits ZFSC-2-1-S* coupler, amplified by the *Mini-Circuits ZJL-7G* 10 dB amplifier, attenuated with the *Mini-Circuits ZX73-2500-S+*, and finally provided to the *OPTO-ELECTRONIC AMPA-B-30* 1 W AOM drivers to control two Crystal Technologies 3080-125 acusto-optical modulators dubbed AOM1 and AOM2. Stability measurements of the radio frequency path were performed. Figure 3.13 shows the output power of the two *PulseBlaster* channels and the amplified

power after the AOM driver. The output power is stable (less than 4 % peak power fluctuation) and the pulse power shape stays constant as well.

3.2.4 Atom Interferometry Laser Light Path

Figure 3.14 shows the exact path the two AI laser beams are taking until they are combined and coupled into the AI periscope. The MOPA2 laser light is immediately split into two paths with a PBS after entering the distribution module. For the purpose of laser cooling and detection these two beams are diffracted into the first order of a 80 MHz signal at the AOM1 and AOM2. For atom interferometry they are diffracted into the first order of a 100 MHz signal at the AOM1 and AOM2. At marking M1 in Figure 3.14 the two beams are recombined. Marking M2 is worth mentioning, because the AI path passes very close to the 3D cooling path. Measurements of the evaporation process with an open atom interferometry shutter have shown a small amount of 3D cooling light, which is not measurable after the AI mirror, couples into the AI periscope and reduces the contrast of the atom interferometer. Therefore, another shutter was added, which blocks the 3D cooling light before the marked point M2. Finally, the two recombined AI beams are coupled into the fast and slow axis of the AI periscope. Due to the different paths of the vertically and horizontally polarized beams a drift in the phase difference between the two beams could occur. To investigate the phase difference between the beams a polarizing beamsplitter cube (PBS) was placed in front of the APD. According to [62], the electric field of a plane wave at an arbitrary point $\vec{r} = 0$ can be expressed in the following way

$$\vec{E}(t) = \begin{pmatrix} a_x \cos(\omega t + \phi_x) \\ a_y \cos(\omega t + \phi_y) \end{pmatrix}, \quad (3.55)$$

where a_x / a_y are the amplitudes and ϕ_x / ϕ_y are the phases. By setting one of the amplitudes to zero one gets a linear polarization. If one sets the difference between the phases to $\pi/2$ and chooses equal amplitudes one gets left- and right-handed circular polarized light

$$\vec{E}(t) = \begin{pmatrix} a_0 \cos(\omega t + \phi) \\ \mp a_0 \sin(\omega t + \phi) \end{pmatrix}. \quad (3.56)$$

Two orthogonally linear polarized AI laser beams passing through the fast and slow axis of the QWP would be converted to left- and right-handed circular polarized laser beams. Choosing the left-handed circular light to have a frequency of $\omega + \delta$, setting the phase only in the right-handed circular light, and adding both electric fields yields

$$\vec{E}(t) = 2a_0 \begin{pmatrix} \cos(\delta/2 \cdot t + \phi/2) \\ \sin(\delta/2 \cdot t + \phi/2) \end{pmatrix} \cdot \cos((\omega + \delta/2)t + \phi/2). \quad (3.57)$$

This is a linearly polarized electric field, whose polarization rotates with half the frequency of the detuning δ . Passing the light beam through a PBS would lead to a intensity modulation of the light beam with the same frequency. Fitting a Gaussian function modulated by a sinusoidal function to all pulse shapes of the left measurement in Figure

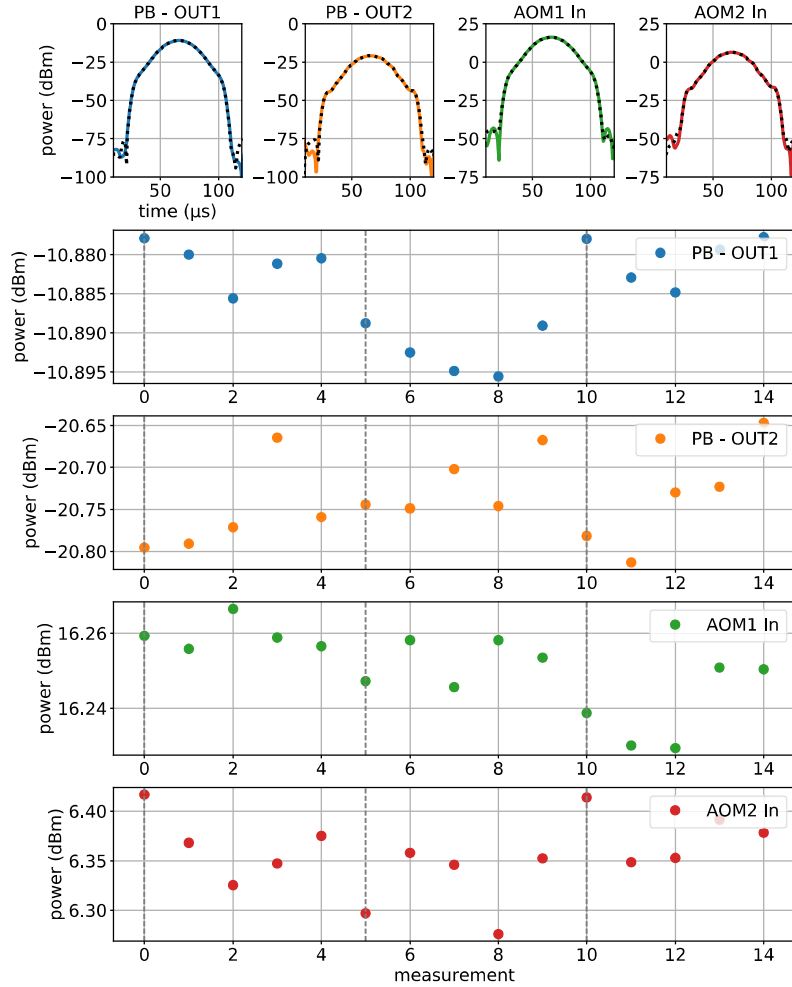


Figure 3.13: Power Stability of the *Spincore PulseBlaster* and the following amplifier chain. For each channel of the *Spincore PulseBlaster* the stability of the TMDA^a power around 100 MHz was measured with the *Rhode & Schwarz FSH8* spectrum analyzer. Before each repetition a 5 min pause was included. In each repetitions 5 shots with a pause of 12 s were performed. The upper row (from left to right) shows the pulse power shape of the first and the fifth shot of the *PulseBlaster* output channel 1 (after low pass filter), *PulseBlaster* output channel 2 (after low pass filter), the AOM driver to AOM2, and the AOM driver to the AOM2. The four plots below show the peak power of the 15 measurements performed at each channel. The gray dashed vertical lines (at measurement 5 and 10) indicate the measurement point with a 5 min pause before. The power was set, such that pulse would diffract 50 % of the atoms to an excited state. No deviation of the first shot after the *PulseBlaster* and the amplifier chain is observed.

^a Time-division multiple access

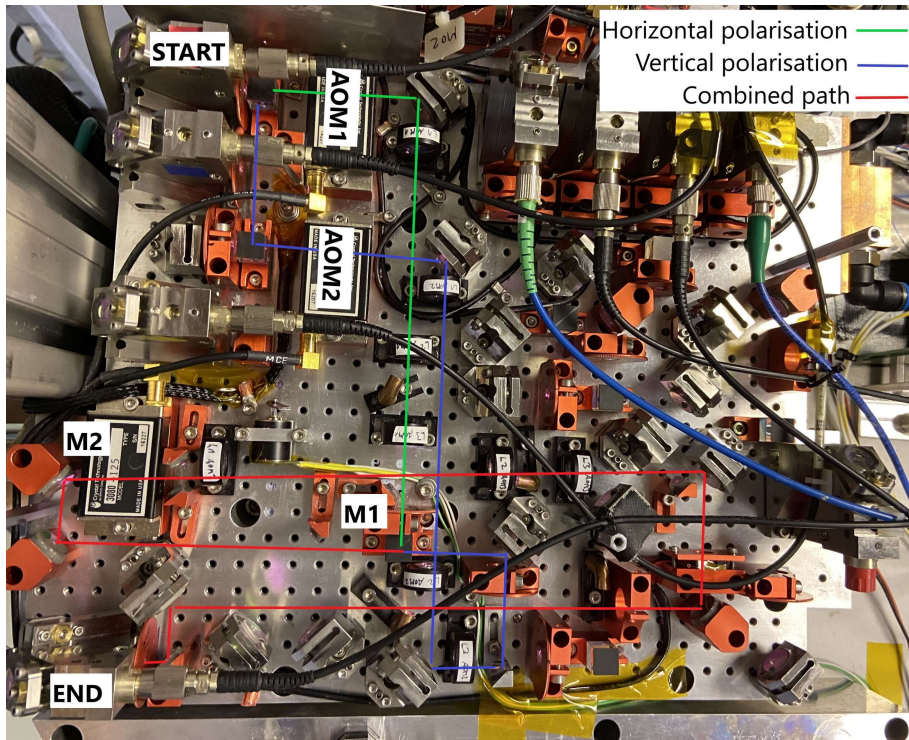


Figure 3.14: Path of the two atom interferometry paths in the distribution module. After the MOPA2 light is coupled into the distribution module it is split at a PBS. The horizontally polarized light passes through AOM1 and the vertically polarized light through the AOM2. At the PBS at marking M1 they are recombined again. Afterwards, they follow the same path and are coupled into the Bragg periscope at the *END* position.

3.16 leads to a detuning of (14.78 ± 0.33) kHz, which is equal within the uncertainties to the set detuning of 15.084 kHz.

The first, tenth, and twentieth signal of a measurement directly after turning on the experiment is shown in Figure 3.15 . Figure 3.16 does the comparison for all signals encoded in a color code for three measurement at different times of the day. After the several hours of measurements the phase stays constant, while directly after turning on the experiment the phase drifts significantly, although, in one direction. Turning off the chiller leads even much faster drift of the phase.

3.2.5 Transport of the Bose-Einstein Condensate

Atom interferometry in microgravity allows for interrogation times in the range of seconds, but to detect atomic clouds after such long time-of-flights requires to reduce their expansion velocity by, for example, a magnetic lens as described in Section 3.1.4. A magnetic lens realized with an atom chip reduces the expansion velocity more effectively with potentials further away from the atom chip due to smaller anharmonic components of the potential [34, 63]. This requires the transport of the atomic cloud from a position closer to the atom chip to a position further away, because evaporation is more efficient in steeper potentials

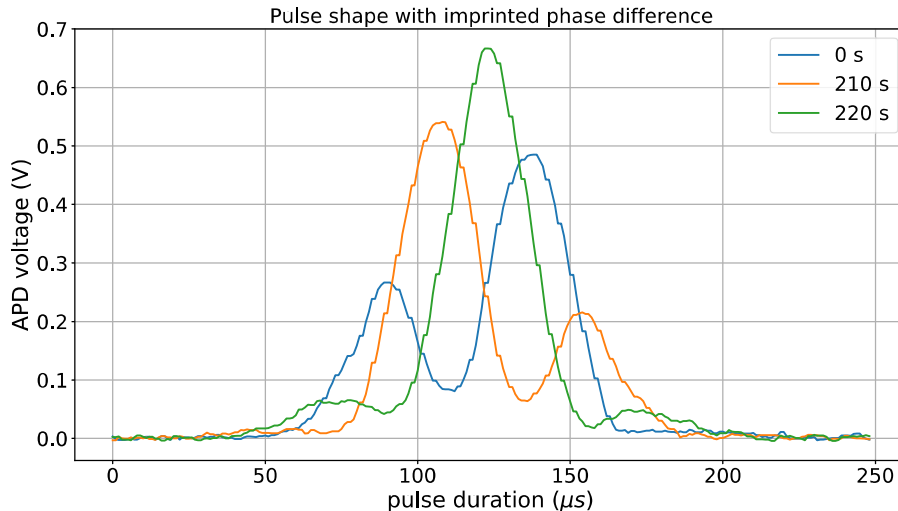


Figure 3.15: Phase difference between the two beams imprinted in the intensity of the pulse. The AI laser beam intensity was measured behind a polarizing beamsplitter cube on an avalanche photodiode. As shown in the text, the overlaid laser beams after passing a quarter wave plate have a linear polarization, which rotates with half the detuning of the laser beam frequencies. The phase difference between the beams is seen in the position of the fringes. This measurement was taken in the morning directly after the experiment was turned on. A significant drift of the phase can be seen. The full measurement and two other measurements can be seen in Figure 3.16.

closer to the atom chip [34]. After the evaporation the BEC is at position $z = 209 \mu\text{m}$ dubbed position a . Another position with the advantage of being further away from the atom chip is at $z = 1462 \mu\text{m}$ dubbed position c . The latter position can in contrast to position a not be realized under gravity, because of the weak trapping potential. Other positions are $a2$ and b located at $z = 354 \mu\text{m}$ and $z = 813 \mu\text{m}$, respectively. They are primarily used to perform experiments on ground. The positions are reached by ramping down the y -coil current to values specified in Table 2.1. The mayor challenge is transporting the BEC fast (in the order of 100 ms) without exciting strong oscillations, such as dipole modes, quadrupole modes, breathing modes, or scissor modes [58]. Linear current ramps excite strong oscillations due to fast acceleration at the beginning and at the end of the ramp. Sigmoid ramps are more suitable, but they still require long transport times. By using the method of *shortcut to adiabaticity* Corgier *et. al.* [42] calculated a ramp, which transports the BEC in 150 ms to position c and only excites little oscillations. The residual oscillations after transport are discussed in the PhD thesis of Christian Deppner [63].

3.2.6 Increasing the Time-of-flight

Albeit having a time-of-flight of several seconds, measurements in microgravity are limited in data rate by the 3 drops per day. Preparatory measurements need to be done on ground and are limited by the available time-of-flight. When releasing the Bose-Einstein condensate from a magnetic trap without transferring momentum in negative y -direction (direction against gravity) the maximal time-of-flight is limited to 22 ms and 14 ms when detecting

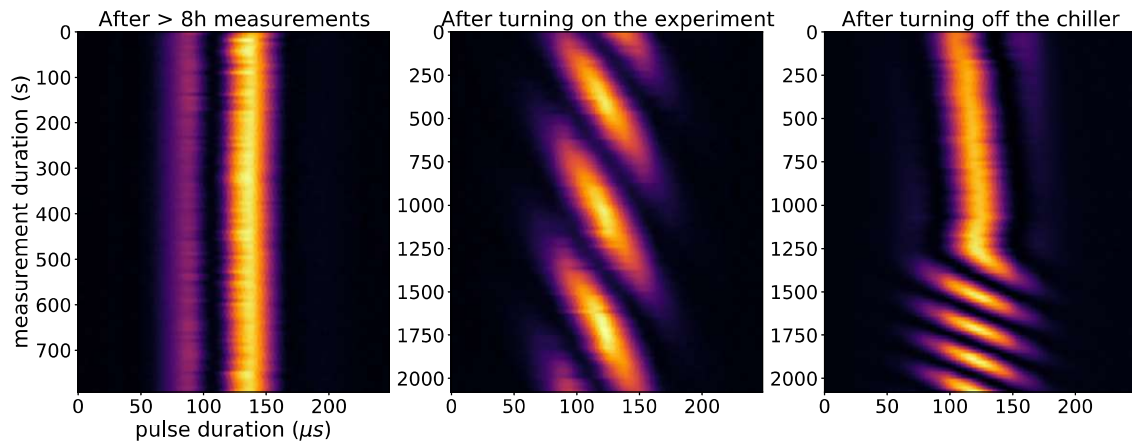


Figure 3.16: Phase drift in three different measurements. The pulse shapes seen in Figure 3.15 were projected onto a 2D plane to visualize the phase drift. From left to right: 1) Stable phase after a full day of measurements. 2) Drifting phase after turning on the experiment. 3) Initially, mildly drifting phase in the middle of a day. After 1250 s into the measurement the chiller was turned off, which led to a fast drift of the phase.

the atomic clouds from the primary and the secondary detection system, respectively.

When investigating the self-interference of Bose-Einstein condensates with an Open-Ramsey type interferometer or an asymmetric Mach-Zehnder interferometer the secondary detection system needs to be used, because the fringe orientation is perpendicular to the direction of the atom interferometry axis, which is along the y direction (7° tilted in the x - y plane). After applying a beam-splitting pulse the different momentum states separate with ~ 11 mm/s leading to a separation of $\sim 150 \mu\text{m}$ after 14 ms, which is also approximately the Thomas-Fermi radius of a Bose-Einstein condensate with $N = 200\text{k}$ atoms 14 ms after release from the magnetic trap at position a . Considering that the beam-splitting pulse can't directly be applied after release from the magnetic trap, because the mean-field-energy is transferred into kinetic energy several milliseconds after release from the trap, and the calculations from Section 3.1.5 only apply for an interaction-free expanding Bose-Einstein condensate a release-method increasing the time-of-flight to several 10th of milliseconds is required. The normal vector of the atom chip is located perpendicular to the gravity vector. Therefore, the atomic cloud needs to be accelerated parallel to the atom chip surface. To accomplish that the y -bias-coil and z -bias-coil currents needs to be varied simultaneously. Figure 3.17 plots the

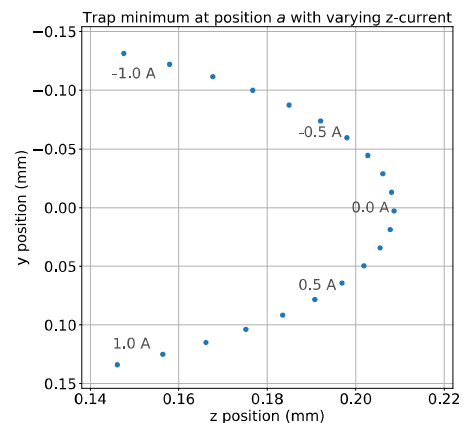


Fig. 3.17: y - z position of the magnetic trap at position a with varying z -bias-coil current. The minimum was calculated with the simulation provided by the TU Darmstadt and the z -current was varied from -1.0 A to 1.0 A in 0.1 A steps.

trap minimum's y- and z-position for a constant y-bias-coil current and varying z-bias-coil current. Two different release sequences were implemented. The first flight trajectory was optimized for low expansion rates and low oscillation mode excitation. Time-of-flights of 34 ms could be reached with this sequence. It will be later referred to as *parabola1* and details on it can be found in the PhD thesis of Merle Cornelius [64]. The second release sequence was optimized for the time-of-flight. It has a higher expansion velocity and a clearly visible scissor mode was excited. On the other hand, the time-of-flight is with 63 ms significantly higher compared to the *parabola1*. To this flight trajectory will be later referred to as *parabola2*. Figure 3.18 compares the two different flight trajectories and the resulting absorption images.

Parabola1 To accelerate the atomic cloud on an upward trajectory the atom were initially transported from position *a* to a position further away from the atom chip by decreasing the y-bias-coil current from -1.5 A to -0.7 A in 250 ms with a sigmoid current ramp. Afterwards, the y-bias-coil and z-bias-coil current were set to -0.635 A and -0.57 A, respectively. The final current values were reached in 2.5 ms and 1.2 ms in case of the y-bias-coil and z-bias-coil, respectively [34]. After 5.5 ms the z-bias-coil current was set to zero and after another 0.1 ms the y-bias-coil current was set to zero. With a delay of 0.1 ms the *BaseChip* and *ScienceChip* structures were set to zero. That sequence of steps led to acceleration upward and away from the atom chip (see Figure 3.18). The positions of the minima of each step are summed up in Table 3.1.

Table 3.1: Sequence of steps for the trajectory *parabola1*. The sequence starts at position *a*. The type in the *step duration* column indicates how the current is ramped from the previous sequence step. The *instant* type indicates that the current was ramped as fast as the current driver allowed for, which was in 2.5 ms and 1.2 ms in case of the y-bias-coil and z-bias-coil, respectively [34]. The final step does not trap atoms, because it does not have a local minimum, but accelerates the atoms away from the atom chip. After the final step the *BaseChip* and the *ScienceChip* structures were turned off as well.

step duration (ms)	(y, z) current (A)	(x, y, z) position (mm)	(f_x, f_y, f_z) (Hz)	rotation x-y plane (°)
250 - sigmoid	(-0.7, 0.0)	(0.10, 0.06, 0.67)	(20, 78, 84)	10.7
5.5 - instant	(-0.635, -0.57)	(-0.43, -0.44, 0.52)	(16, 84, 79)	12.4
0.1 - instant	(-0.635, 0.0)	(0.13, 0.08, 0.76)	(19, 62, 69)	11.7
0.1 - instant	(0.0, 0.0)	-	-	-

Parabola2 For this trajectory the atoms were transported from position *a* to a position located 0.44 mm below and 0.44 mm displaced in the positive x-direction by ramping the y-bias-coil and z-bias-coil current to -0.8 A and 1.0 A with a sigmoid current ramp in 100 ms, respectively. Hereafter, the y-bias-coil and z-bias-coil currents were set back to the values of position *a* and after 2.7 ms the y-bias-coil current was turned off and after another 0.4 ms the *BaseChip* and *ScienceChip* structures were set to zero. This led to an acceleration upwards and away from the atom chip as can be seen in Figure 3.18. The absorption image in that figure shows an elongated Bose-Einstein condensate, whose axis

does not correspond to the atom chip coordinate axis. Furthermore, the expansion velocity is greater than the expansion velocity after the trajectory *parabola1*. This properties likely stem from the release from a steeper trap, faster acceleration, and a rotation of the trap axis during the acceleration (from 10.9° in the x-y plane at the lower position to 3.6° at position *a*). The exact steps of this trajectory are shown in Table 3.2. Nevertheless, this trajectory will prove useful for self-interference experiments due to the long time-of-flight and the greater extension in y-direction in comparison to trajectory *parabola1*.

Table 3.2: Sequence of steps for the trajectory *parabola2*. The sequence starts at position *a*. In contrast to the *parabola1* the minimum is pulled down 0.44 mm and accelerated upwards back to position *a*. The steeper trapping potential causes the atoms to accelerate faster. Furthermore, the almost 20 times higher trapping frequency in y-direction in comparison to the x-direction causes the atoms to mainly accelerate in the y-direction. The final step does not trap atoms, because it does not have a local minimum, but accelerates the atoms away from the atom chip. After the final step the *BaseChip* and the *ScienceChip* structures were turned off as well.

step	(y, z)	(x, y, z)	(f_x, f_y, f_z) (Hz)	rotation
duration (ms)	current (A)	position (mm)		x-y plane ($^\circ$)
100 - sigmoid	(-0.8, 1.0)	(0.44, 0.44, 0.21)	(20, 136, 146)	10.9
2.7 - instant	(-1.5, 0.0)	(0.02, 0.00, 0.21)	(24, 456, 462)	3.6
0.4 - instant	(0.0, 0.0)	-	-	-

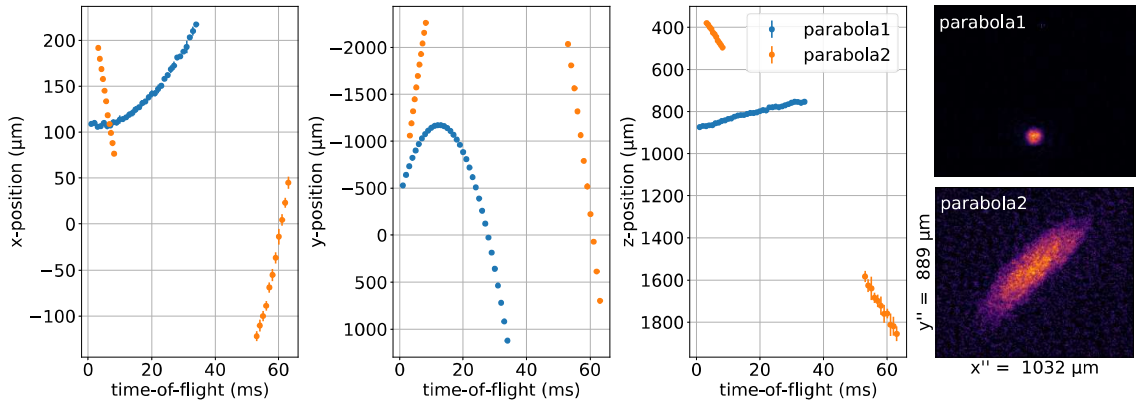


Figure 3.18: Comparison of the flight trajectories of *parabola1* and *parabola2*. The position was determined from the secondary detection system. The missing data points at the *parabola2* trajectory are due to atomic clouds being out of the imaging plane. The two absorption images show the Bose-Einstein condensates after 34 ms and 60 ms time-of-flight in case of the trajectory of *parabola1* and *parabola2*, respectively. The size of the absorption images are equal and the pixels are square shaped.

3.3 Rabi Oscillations

To perform atom interferometry measurements it is necessary to implement a beam-splitter pulse and in case of a Mach-Zehnder interferometer additionally a mirror pulse. Beam-splitting and mirror pulses are expressed in terms of Rabi oscillation cycles. A beam splitting pulse performs a quarter cycle and is called a $\pi/2$ -pulse and a mirror pulse performs half a cycle and is called a π -pulse. The $\pi/2$ - and π -values refer to the argument of a sinusoidal function. Rabi oscillations of a 2-photon processes are described by Equation 3.7. Either pulse duration at constant power or pulse power at constant duration can be increased to observe oscillations between the ground and excited state. Figure 3.19 shows Rabi oscillations at constant power. In this measurement the atoms were freely falling on the trajectory *parabola1* (see Section 3.2.6) with an angle of 7° to the AI laser beams. Prior to this measurement the detuning between the laser beams was optimized for a pulse duration of $165 \mu s$ to accommodate the detuning-shift due to gravitational acceleration. With a fixed detuning the pulse duration was varied and the number of atoms in the two momentum states were detected by the primary imaging system. One and a half cycles were scanned. 80 % of the population could be transferred to the excited state with the first π - pulse, but only 50 % at the next inversion. The reason for the decreasing efficiency is the detuning-shift due to gravitational acceleration, which amounts to 12 kHz after $500 \mu s$. We could not mitigate this problem due the missing support for frequency sweeping in our setup. We continued the optimization by fixing the pulse duration and scanning the pulse power around the π - pulse. We chose pulse durations¹ with the total length of $80 \mu s$, $100 \mu s$, and $120 \mu s$. The lower boundary was limited by diffraction to higher momentum states due to higher peak powers. A diffraction efficiency over 95 % was achieved with an pulse duration of $80 \mu s$. Additionally, in Figure 3.20 one can see that the $80 \mu s$ pulse duration is favorable, because it offers a wider pulse power tolerance around its maximum.

Several source can lead to uncertainties in determination of the Rabi frequency and cause fluctuations in the efficiency over the course of a measurement. In the end, this leads to fluctuations of the atom interferometer contrast. Figure 3.22 shows 50 consecutive measurements of a $\pi/2$ - pulse. The first 3 data points deviate significantly from the 50 % diffraction efficiency. The likeliest reason is the AI laser power, shown as well in the figure. Variations in the AI laser power can stem from the laser itself, the coupling between different modules, and from the acousto-optic modulator (AOM). During standby the AOMs are supplied with a 80 MHz sinusoidal signal from a RF source developed in the QUANTUS collaboration with a power of approximately 1 W. During a sequence the power of the 80 MHz signal is reduced or turned off to adjust the necessary laser power. Additionally, for a sequence with AI pulses a 100 MHz sinusoidal signal is provided to the AOMs from a *Spincore PulseBlaster* DDS. In Section 3.2.3 it was shown that all the components up to the AOM show no "warm-up" effect. Hence, it can be concluded that the AOM is the cause of the "warm-up" effect. The laser power and the coupling between different modules can be excluded, because the former is typically on several hours

¹ The pulse duration is 8 times the σ -width of the Gaussian pulse. All the following pulse durations are stated in that manner.

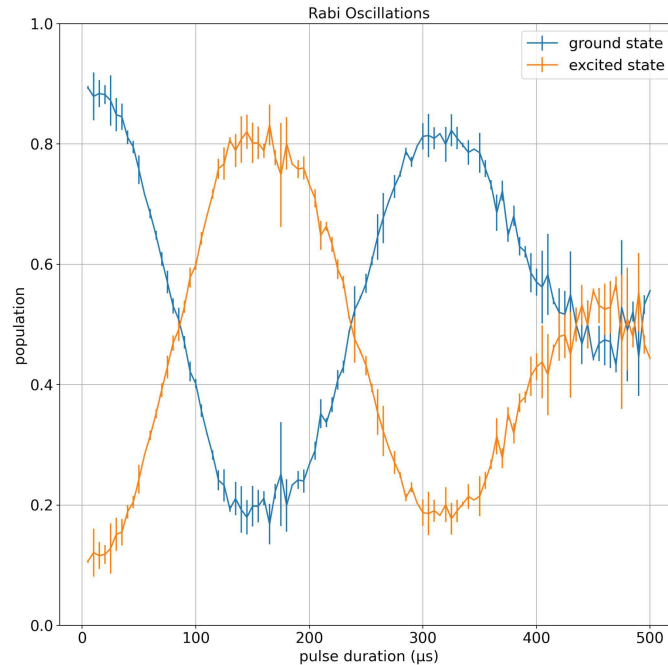


Figure 3.19: Scan of the pulse duration of a single diffraction pulse. Prior the detuning of the laser beams was optimized for a pulse duration of $165 \mu s$. A value of 90 kHz was determined. The pulse power was fixed during the measurement. Due to missing possibility of sweeping the detuning during a single pulse the population transfer at a pulse duration of $500 \mu s$ is not exceeding 50% . The gravitational acceleration of the free falling atoms shift the resonant detuning by approximately 12 kHz .

before a measurement and the latter only changes gradually with temperature changes and mechanical stress.

Further sources of uncertainties are residual magnetic field gradients causing acceleration of atoms in the $m_f = 2$ states, variations of the detuning to the intermediate state, variations in the detuning between the two AI laser beams, polarization instabilities in the AI optical fiber, variation in the position of the BEC due to the release, and diffraction to higher order. These sources of uncertainty will be discussed below:

- **Residual magnetic field gradients:** In this measurements the atoms were not transfer to the $m_f = 0$ state via adiabatic rapid passage, but remained in the $m_f = 2$ state. Constant magnetic field gradients over the course of the measurement would have been included in the determination of the detuning of the AI laser beams and would have been another source of the acceleration additionally to the gravitational acceleration. Varying magnetic field gradients could stem from measurements at the neighboring QUANTUS-1 experiment or by tools and devices put close to the

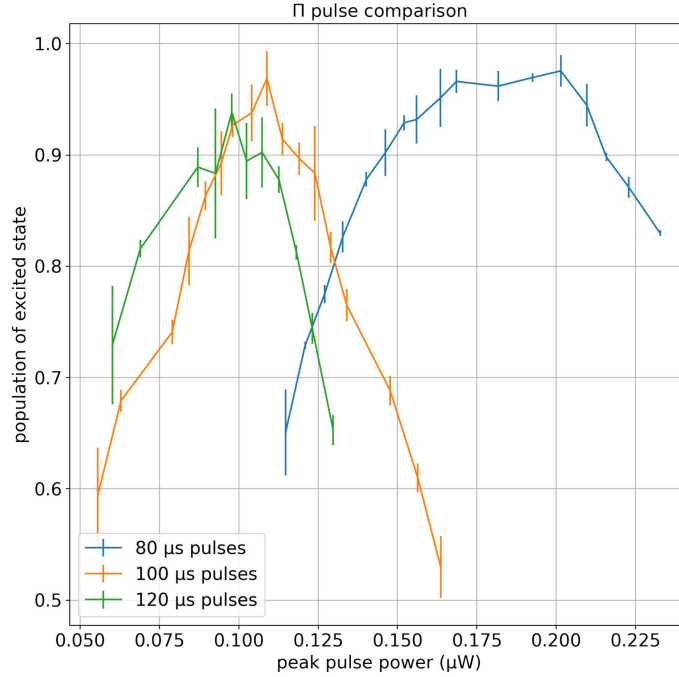


Figure 3.20: Comparison of different pulse durations. Single diffraction pulses with an optimal detuning were used. By reducing the pulse duration and adjusting the detuning the diffraction efficiency can be increased from 80 % for 165 μs pulses to over 95 % for 80 μs . Pulse durations shorter than 80 μs were not investigated, because short pulses and high laser power caused diffraction to state higher than $2\hbar k$.

experiment. The residual magnetic gradients in the chamber were determined [34] to be around 1 G/m. The force on the $m_f = 2$ is then 0.07 % of the force of the gravitational acceleration and can be neglected for the sake of determining the π -pulse duration.

- **Detuning to intermediate state:** In Section 3.2.2 the detuning was determined to be 1268 ± 41 MHz (relative error of 3.2 %). The current-by-pass being the reason for the mayor relative error. By Equation 3.9 the relative error directly translates in a 3.2 % relative error of the diffraction efficiency ($\Omega \sim \frac{1}{\Delta}$).
- **Detuning between the AI laser beams:** The two AI laser beams are detuned by a frequency in the range of 100 kHz by passing two AOMs separately, which are driven by the two channels of the *Spincore PulseBlaster* DDS. The one channel has a frequency of 100 MHz and the other 100 MHz plus the detuning. The *PulseBlaster* frequency resolution is 0.28 Hz at a 50 MHz reference clock. Hence, far below the detuning range.
- **Polarization of the AI optical fiber:** The two AI laser beams are coupled in the

two axis of a polarization maintaining single mode fibers and overlaid with a quarter wave plate and a mirror. A low polarization extinction ratio (PER) would cause parts of the AI laser beams being overlaid with oneself and creating a standing lattices. The detuning in the range of 100 kHz necessary to drive a transition to another momentum state of the falling atoms is sufficiently far away from the standing lattices (0 kHz detuning) not to cause additional interactions, but the laser power going into the standing lattices is subtracted from the moving Bragg lattice. The PER in both axis was above 33 dB under mechanical and thermal stress. Thus, the effects of polarization can be neglected.

- **Variation in the *parabola1* trajectory:** A different trajectory due to variations in the release of the BEC would cause the atoms to be off resonant due to a different velocity. The variation of the time point of the apex was determined by making a time-of-flight measurement and fitting a 2nd degree polynomial to the data. The resulting 95 % confidence bound was 0.11 ms, which in turn gives a uncertainty of the detuning of 2.75 kHz ($24.985 \text{ kHz/ms} \cdot 0.11 \text{ ms} = 2.75 \text{ kHz}$). This is approximately 1-2 % of the Rabi frequency, depending on the chosen parameters.
- **Diffraction to higher orders:** Unwanted diffractions to higher orders occurs when the AI pulses are not in the pure Bragg regime (see Section 3.1.2). Diffraction to higher orders reduce the number of atoms in the output ports of an atom interferometer. Hence, reducing the signal-to-noise-ratio of the interferometer. Figure 3.21 shows the fraction of atoms in unwanted orders for a pulse duration of 80 μs , 100 μs , and 120 μs . It can be concluded that for shorter pulse durations more atoms are diffracted to other order than $+2\hbar k$.

It was shown that it is possible to depopulate the ground state to 5 % with a π -pulse. When only considering the $|0\hbar k\rangle$ and the $|+2\hbar k\rangle$ states the diffraction efficiency is over 95 %. Considering losses into higher orders, such as $|-2\hbar k\rangle$ and $|+4\hbar k\rangle$ the diffraction efficiency into the $|+2\hbar k\rangle$ reduces to 80 %. When performing single diffraction experiments losses to higher orders or lower diffraction efficiencies are equivalent, because they both cause a reduction of atoms in the output ports. In case of double diffraction, which will be treated in Section 3.5, the depopulation of the ground state is more important. In case of an Open-Ramsey type interferometer or a Mach-Zehnder type interferometer the undiffracted ground state enters the output ports as a spurious cloud and distorts the result.

Moreover, the diffraction efficiency could be improved by increasing the precision of the frequency control during the AI pulse, improving the flight trajectory repeatability, and by introducing the capability to sweep the detuning during an AI pulse. Furthermore, the measurement shown in Figure 3.22 indicates a problem for measurements in the drop tower due to a "warm-up"-effect. The mitigation of this problem will be introduced in Section 3.5.

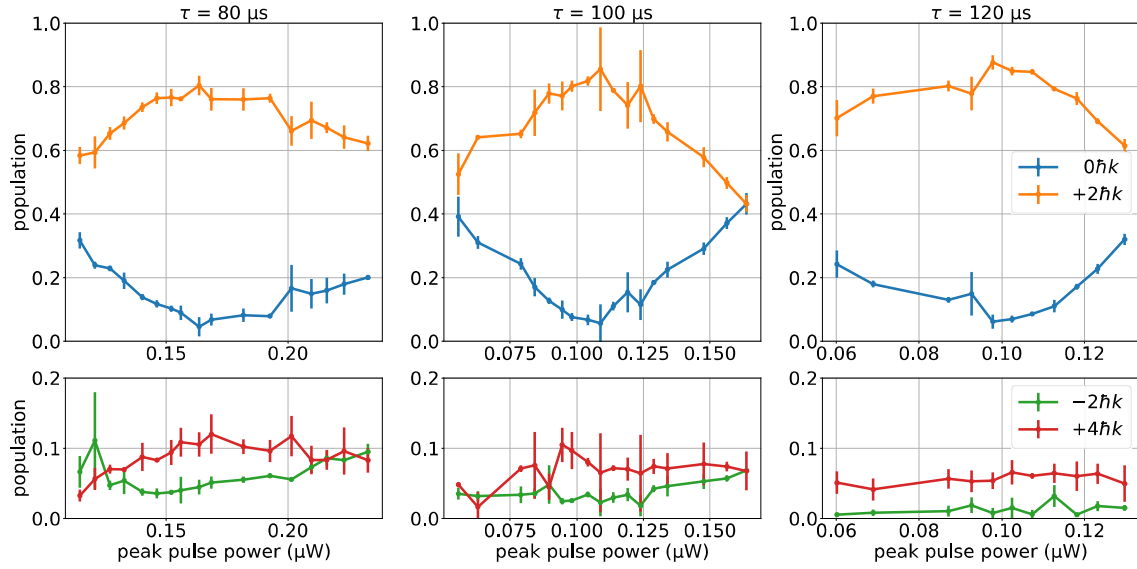


Figure 3.21: Diffractions to higher order for $80 \mu s$, $100 \mu s$, and $120 \mu s$ pulses. This diffractions occur due to AI pulses, which are not in the pure Bragg regime. Higher laser power for the same pulse duration lead to more diffracted atoms to unwanted higher orders. The *population* axis refers to the population in reference to the total number of atoms in the $|0\hbar k\rangle$, $|\pm 2\hbar k\rangle$, and $|4\hbar k\rangle$ states. While in Figure 3.20 the population referred to the number of atoms in the $|+2\hbar k\rangle$ in comparison to the atoms in the $|+\hbar k\rangle$ and $|0\hbar k\rangle$ states.

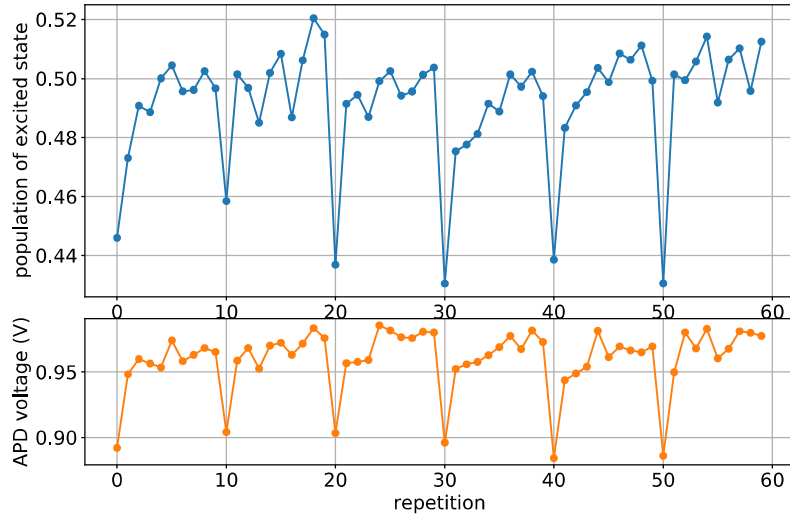


Figure 3.22: The stability of the single diffraction $\pi/2$ -pulse was investigated. Consecutive $\pi/2$ -pulses were performed in groups of 10. Ten minutes before the measurement no measurements were performed. After 10 repetitions the measurement was paused for 20 s, 40 s, 60 s, 120 s, and 240 s. Each repetition lasted 10 s. It is clearly visible that the diffraction of the first measurement after the pause is lower and it directly correlates to the lower pulse power measured at the avalanche photo diode. Further measurements restricted the lower pulse power to the diffraction efficiency of the acousto-optical modulator (see Section 3.2.3).

3.4 Open-Ramsey Type Interferometer

As mentioned before, atom interferometry experiments on long time-scale set strict demands on the underlying matter wave source [13], such as long coherence length and slow expansion. Bose-Einstein condensates (BEC) are ideally suited for that application. Slow expansion rates can be achieved by a release from a shallow trap or further reduced by application of a magnetic lens and the long de Broglie λ_{dB} lead to long coherence length. The phase coherence of a BEC or more general a matter wave source can be investigated by self-interference experiments. Hence, allowing to probe the coherence length. The first interference experiments were performed in 1997 [65] by releasing two BECs from a double well trap. Self-interference of a BEC can also be observed by splitting an ensemble and introducing a center-of-mass difference by means of two $\pi/2$ -pulses. The method is called an Open-Ramsey type interferometer (ORI) and was introduced in Section 3.1.5. The resulting interference pattern is along the AI beam direction and the periodicity or fringe spacing is described by Equation 3.42

$$d = \frac{\pi \cdot T_{TOF}}{m \cdot k \cdot T_{int}},$$

where d is the fringe spacing, T_{TOF} is the time-of-flight after release from the trap, T_{int} the interrogation time (time between the $\pi/2$ -pulses), m the mass of the rubidium 87 atom, and k the wave vector of the laser beam. The coherence length can be deduced by investigating the contrast as a function of the interrogation time. According to Reference [66] the decay of the contrast as function of the interrogation time can be described by a Gaussian. The coherence length L_c can be defined as the center-of-mass separation at the time T_e , when the contrast reduces to a value of $1/e$

$$L_c = 2 \cdot v_r \cdot T_e, \tag{3.58}$$

where $v_r \approx 5.86$ mm/s is the recoil velocity. This allows to study decoherence effects, such as thermal excitations, collisions with the background gas, dephasing due to stray magnetic field gradients, etc.

In this section ORI measurements on ground with single diffraction will be presented. In the next section the ORI measurement with double diffraction on ground and in microgravity will be presented. Section 3.6 will present ORI measurements with lensed BECs in microgravity and Section 3.7 will investigate the coherence length in an asymmetric Mach-Zehnder interferometer.

The trajectory *parabola2* (see Section 3.2.6) was chosen for the Open-Ramsey type interferometer with single diffraction. It offered much greater size in y -direction ($300 \mu m$ at *parabola2* and $60 \mu m$ at *parabola1* for the maximal time-of-flight) allowing to investigate shorter interrogation times. Additionally, the time-of-flight was long enough to significantly separate the two output ports. The ORI sequence began 15.5 ms after release from the trap. The atoms remained in the magnetically sensitive $m_f = 2$ state. The sequence consisted of two Gaussian pulses of $80 \mu s$ duration separated by an interrogation time of $150 \mu s$ to $500 \mu s$ incremented in $25 \mu s$ steps. After a time-of-flight of 43 ms the atoms were detected

from the secondary detection system. Each measurement was averaged 10 times. To the resulting sum of rows of the absorption image was the following function fitted

$$f(x) = A_G \exp \frac{-(x - x_c)^2}{2\sigma^2} + A_{TF} \left(1 - \frac{(x - x_c)^2}{R_{TF}^2} \right) \cdot (1/2 + C_{TF}/2) \left[\sin \left(2\pi \frac{x - x_c}{d} + \phi \right) \right], \quad (3.59)$$

where A_G is the amplitude of the Gaussian, x_c the cloud center, σ the width of the cloud, A_{TF} the amplitude of the Thomas-Fermi profile, R_{TF} the Thomas-Fermi radius, C_{TF} is the contrast of the Thomas-Fermi profile, d the fringe spacing, ϕ the phase of the sinusoidal modulation. The total contrast of the above function was calculated by $C = \frac{A_{TF} \cdot C_{TF} - A_G}{A_{TF} + A_G}$. An example of a fit can be seen in Figure 3.23 for an interrogation time of $500 \mu s$. The results are shown in Figure 3.24. The interrogation time T_e when the contrast falls to $1/e$ was determined to be $(585 \pm 25) \mu s$ leading to a coherence length of $(6.9 \pm 0.4) \mu m$. The Thomas-Fermi radius in y-direction was determined from a time-of-flight series to be $(92.7 \pm 7.3) \mu m$ at the time of the ORI pulses. This leads to a coherence length of $(7.4 \pm 0.7) \%$ of the Thomas-Fermi radius.

The fringe spacing calculated for a time-of-flight of 58.5 ms agrees with all measured values expect for interrogation times of $150 \mu m$, $175 \mu m$, and $200 \mu m$. At that data points the measured values are more than 3 standard deviations below the calculated values. Several issues can cause a reduction of the coherence length and uncertainties in the determination of the fringe spacing. A fully phase-coherent condensate would have a coherence length of the size of the Thomas-Fermi radius. The condensate fraction of the ensemble was only 40 % after acceleration on the trajectory *parabola2*. This is significantly lower than the 90 % condensate fraction after release from the trap at position a . The high thermal background is likely the main reason for the decoherence of ensemble. Further source of decoherence and uncertainties will be discussed below.

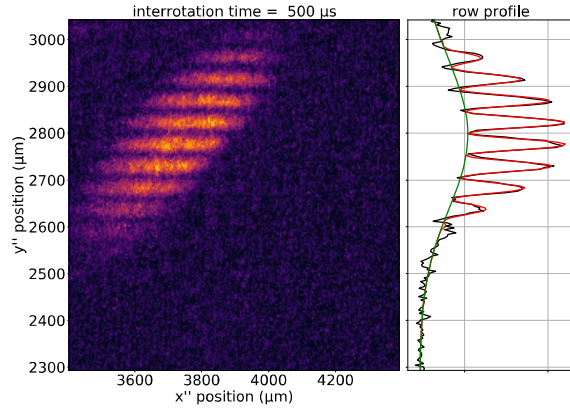


Fig. 3.23: Example of Equation 3.59 fitted to an absorption image with an interrogation time of $500 \mu s$. The resulting fringe spacing is $46.8 \mu m$ and the contrast is 0.35.

- **Dephasing:** According to Equation 3.34 the phase of a BEC changes in an external potential. This could be for example laser light or a magnetic potential. The atoms were in a magnetically sensitive state $m_f = 2$ and the shutter in front of AI fiber was open for 14.5 ms. The stray magnetic field gradients were measured to be below

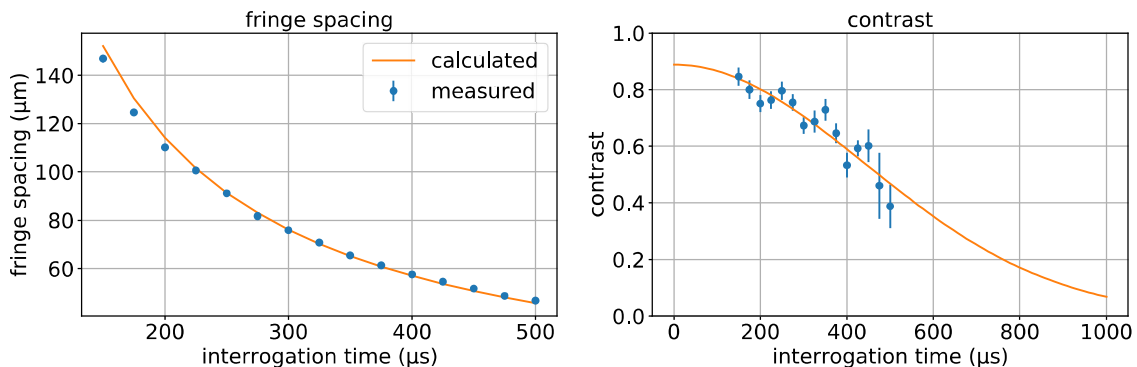


Figure 3.24: The fringe spacing and the contrast of an ORI with single diffraction. 14.5 ms after release from the magnetic trap was an Open-Ramsey type interferometer applied. The interrogation time was varied between 150 μs and 500 μs in 25 μs steps. The measurements were repeated 10 times. The total time-of-flight was 58.5 ms. To the sum of rows was Equation 3.59 fitted to extract the fringe spacing and the contrast.

1 G/m. The stray light was 1.2 GHz detuned to the $F=2 \rightarrow F'=3$ line. Both effects are likely negligible to the decoherence due to the high thermal fraction in the atomic ensemble. Additionally, the wavefront curvature of the beam with the $1/e^2$ -diameter of 3.31 mm is unlikely to significantly dephase a BEC with a Thomas-Fermi radius of $\sim 100 \mu m$.

- **$\pi/2$ - pulse variations:** Deviations of the $\pi/2$ - pulse diffraction efficiency from 50 % will cause different population sizes in the output ports. This means we have in each output port two overlapping BECs with different number of atoms. According to Equation 3.36 different number of atoms in the two BECs per output port should not change the contrast of the cross-term.
- **Resolution limit of the imaging system:** The resolution of the secondary imaging system was characterized in Reference [17]. A value of $7.81 \mu m$ was found. This value is almost six times smaller than the smallest measured fringe spacing. A fringe spacing in the order of the resolution would degrade the contrast. Hence, even considering a degrading resolution would not explain decreasing contrast due to the resolution limit.
- **Calibration of magnification:** The determination of the magnification of the optical system is described in Reference [17]. A value of $M = (1.77 \pm 0.03)$ was found. This translates to an uncertainty of the effective pixel size of $0.11 \mu m$. This does not significantly contribute to the fringe spacing determination.

This measurement showed an Open-Ramsey type interferometer with single diffraction beam splitting pulses. The fringe spacing agreed with the prediction for interrogation times greater than 200 μs . The deviation for shorter times could stem from the approximation made in the calculation of the fringe spacing, but was not further investigated. By measuring the contrast as a function the interrogation time a coherence length of $6.9 \pm 0.4 \mu m$ was determined. This is $7.4 \pm 0.7 \%$ of the Thomas-Fermi radius. The likeliest reason

for the short coherence length in comparison to the condensate size is decoherence due to a high thermal fraction (60 %). The next step will be to perform an Open-Ramsey type interferometer with double diffraction beam splitting pulses.

3.5 Open-Ramsey Type Interferometer with Double Diffraction

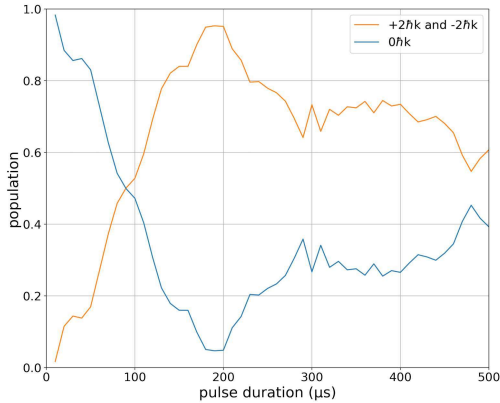


Fig. 3.25: Rabi oscillation with double diffraction at low laser power. The *steps* are due to fast oscillations with small amplitudes in the quasi-Bragg regime are visible. A diffraction efficiency of 95 % was reached at the $\pi/2$ -pulse.

power was chosen such that the $\pi/2$ - pulse is located around $200 \mu s$.

Shorter pulse durations were not favorable, because they led to losses due to operation in the quasi-Bragg regime. Even with lower power the fast oscillations in form of *steps* are visible. However, longer pulse durations are also problematic, because the detuning changes due to gravitational acceleration and can not be adjusted to both lattices simultaneously. A diffraction efficiency of 95 % was reached. Diffraction to higher orders was not observed.

To apply two pulses for an Open-Ramsey type interferometer a trade-off needs to be made, because only one of the pulses can be applied at the apex. It was decided to center the ORI sequence around the apex, where the first $\pi/2$ - pulse is applied before

the apex and the second after the apex. The trajectory *parabola2* was chosen over *parabola1* due to longer time-of-flight and larger Thomas-Fermi radius in the direction of the AI

To perform double diffraction in our setup is more challenging than single diffraction, because the atom interferometry axis shows in the direction of gravity (titled by 7°). To transfer the atoms from the $0\hbar k$ momentum states to the $\pm 2\hbar k$ states it is necessary that they interact with two lattices moving in opposite directions. Hence, the free falling atoms would always be detuned to one lattice. The solution is to accelerate the atoms after release from the magnetic trap upwards and apply the double diffraction pulse at the apex. Figure 3.25 shows the double diffraction efficiency at the apex. The trajectory *parabola1* was used for this purpose, because of smaller easier fit-able cloud sizes. This allowed to determine the population in the three output ports more precisely. For that measurement the pulse

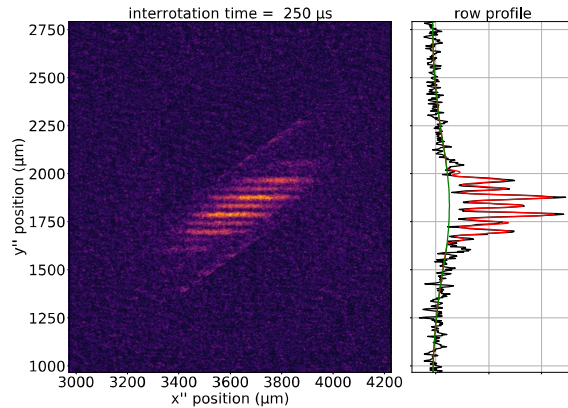


Fig. 3.26: Example of Equation 3.59 fitted to an absorption image with an interrogation time of $250 \mu s$. The resulting fringe spacing is $44.9 \mu m$ and the contrast is 0.74.

pulse. A shorter pulse duration of 100 μs was chosen due to the higher velocity spread of the ensemble. 200 μs pulses caused the outer fraction of the ensemble not being diffracted. The short pulse duration reduced the diffraction efficiency to 80 %. The ORI sequence was then applied around the apex at 30.144 ms after the release. Interrogation times between 150 μs and 300 μs in 25 μs steps were measured. Each measurement was 10 times repeated. After a total time-of-flight of 57.9 ms the three output ports were detected with the secondary imaging system. The time-of-flight of 27.8 ms after the ORI sequence was not enough to separate the three output such that the row profiles did not overlap. Further post-processing needed to be done to extract the fringe spacing and the contrast. Two triangular shapes covering the $|+2\hbar k\rangle$ and $|-2\hbar k\rangle$ were replaced with empty patches of the absorption image. An example is shown in Figure 3.26. To the sum of rows of each absorption image was a Gaussian profile plus a Thomas-Fermi profile modulated by two sinusoidal functions fitted

$$f(x) = A_G \exp \frac{-(x-x_c)^2}{2\sigma^2} + A_{TF} \left(1 - \frac{(x-x_c)^2}{R_{TF}^2} \right) (1/2 + C_{TF}/2) \cdot \left[(1-S) \sin \left(2\pi \frac{x-x_c}{d} + \phi_1 \right) + S \sin \left(2\pi \frac{x-x_c}{2d} + \phi_2 \right) \right], \quad (3.60)$$

where A_G is the amplitude of the Gaussian, x_c the cloud center, σ the width of the cloud, A_{TF} the amplitude of the Thomas-Fermi profile, R_{TF} the Thomas-Fermi radius, C_{TF} is the contrast of the Thomas-Fermi profile, S the fraction of the sinusoidal modulation with a double fringe spacing, d the fringe spacing, ϕ_1 the phase of the sinusoidal modulation with fringe spacing d , and ϕ_2 the phase of the sinusoidal modulation with fringe spacing $2d$. The second sinusoidal function was added to accommodate for atoms not diffracted by the first $\pi/2$ -pulse. These atoms are then diffracted by the second $\pi/2$ -pulse, due to the non-perfect diffraction efficiency this introduces a third atomic cloud to each output port. That third cloud is centered between the two initially diffracted clouds causing a diffraction pattern with double the fringe spacing (see Equation 3.42). The total contrast of the above function was calculated by $C = \frac{A_{TF} \cdot C_{TF} - A_G}{A_{TF} + A_G}$. Figure 3.27 shows the results of the measurement. The interrogation time T_e when the contrast falls to $1/e$ was determined to be $(825 \pm 138) \mu s$ leading to a coherence length of $(19.3 \pm 3.2) \mu m$. The Thomas-Fermi radius in y -direction was determined from a time-of-flight series to be $(159 \pm 8) \mu m$ at the time of the ORI pulses. This leads to a coherence length of $(12 \pm 2) \%$ of the Thomas-Fermi radius. The fringe spacing calculated for a time-of-flight of 57.9 ms agrees with all measured values.

Microgravity The next step was to perform beam splitter pulses and an Open-Ramsey type interferometer with double diffraction in microgravity. To achieve high diffraction efficiencies during a drop at position c a special calibration procedure was necessary. Due to the mechanical stress on the drop capsule and the day to day variations of the laser power the rf power for the AOM needed to be adjusted for each drop. Additionally, it is

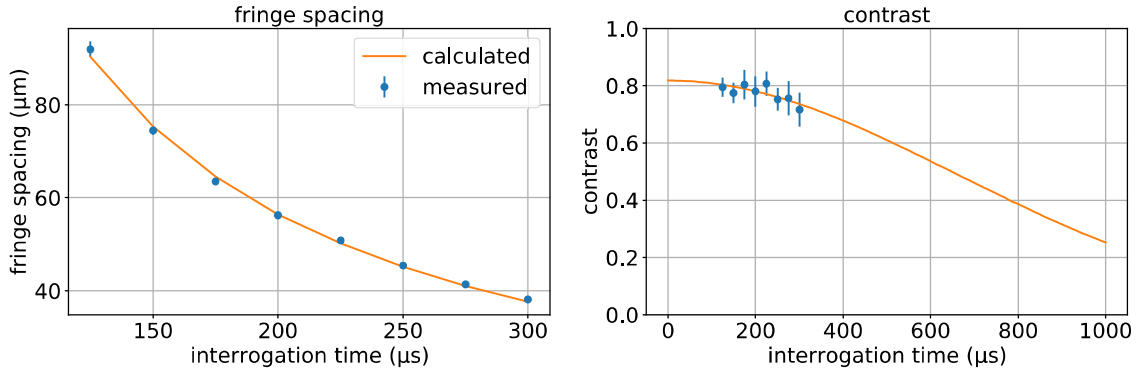


Figure 3.27: The fringe spacing and the contrast of an ORI with double diffraction. 30.144 ms after release from the magnetic trap was an Open-Ramsey type interferometer applied. The interrogation time was varied between 150 μs and 300 μs in 25 μs steps. The measurements were repeated 10 times. The total time-of-flight was 57.9 ms. To the sum of rows was Equation 3.60 fitted to extract the fringe spacing and the contrast.

not straight forward to perform a scan around the double diffraction $\pi/2$ pulse, because the magnetic trap at position c is not able to trap the atoms under gravity and the atoms need to be at rest at the frame of the atom chip coordinate system to be resonant to both Bragg lattices. A procedure was developed to achieve a free fall trajectory of the atomic cloud along the y -direction with little velocity in x - and z -direction. This was achieved by first accelerating the BEC on an upward trajectory and removing the x - and z -velocity with a short magnetic lens at the position c . Details of that procedure can be found in Reference [64]. The rf power for a single diffraction π - pulse was determined with a scan. According to Equation 3.17 the laser power necessary for for a double diffraction $\pi/2$ - pulse is the laser power necessary for a single diffraction π - pulse divided by $\sqrt{2}$. Table 3.3 shows the double diffraction efficiency in four drops of the campaign. The efficiency was 90 % or greater except during drop 309. The most likely reason for the diffraction efficiency of 73 % is hot weather. The diffraction efficiency could be improved by adjusting the cooling procedure.

Table 3.3: Double diffraction efficiency during the drop campaign. The $\pi/2$ - pulse in drop 281 was applied on an unlensed cloud. The rest of the measurements were performed with lensed clouds. The low diffraction efficiency in drop 309 was very likely caused by hot temperatures in the summer, which heated up the drop tower. The efficiency could be again increased to over 90 % by adjusting the cooling procedure of the drop capsule.

	Drop 281	Drop 286	Drop 309	Drop 312
Diffraction Efficiency (%)	90	91	73	92

In microgravity the BEC stayed resonant with the two lattices, because of the center-of-mass motion after the release from the magnetic trap was less than 156 $\mu\text{m}/\text{s}$ [25]. Five measurements were done where the BEC was release from the final magnetic trap at

position c and after 40 ms time-of-flight an Open-Ramsey type interferometer sequence with an interrogation time of $520 \mu\text{s}$. Afterwards, the clouds separated for 40 ms, 80 ms, and 120 ms. The measurement with a separation time of 40 ms was repeated with atoms in the $m_f = 2$ and the $m_f = 0$ state and the measurement with a separation time of 80 ms was repeated twice in the $m_f = 2$ state. The measurements with separation times of 120 ms was performed once in the $m_f = 2$ state. The absorption images of the visible diffraction orders are shown in Figure 3.29. To the sum of rows of each absorption image was Equation 3.60 fitted. The resulting fringe spacings and contrast of the images in Figure 3.29 are shown in Figure 3.30. The three (two in case of 160 ms time-of-flight) diffraction orders were fitted separately and the mean and standard deviation was plotted against the time-of-flight. Figure 3.28 shows the individual fits of the $2\hbar k$ and $0\hbar k$ order.

It is possible to estimate the coherence length by averaging the five measured contrast ($C = 0.76$) and assuming an initial contrast of 0.85 (average value between the single diffraction and double diffraction measurement on ground). This results in a T_e of $1410 \mu\text{m}$ and a coherence length of $33 \mu\text{m}$. A measurement of the Thomas-Fermi radius in the y -direction after a time-of-flight yielded a radius of $70 \mu\text{m}$. This would result in a coherence length of almost 50 % of the Thomas-Fermi radius. This value has very high uncertainty due to only a single interrogation time and an assumption on the initial contrast. If for example, the initial contrast is assumed to be 1.0 the coherence length decreases to 35 %. Nevertheless, it can be concluded that the coherence length is significantly higher than at the ground measurements.

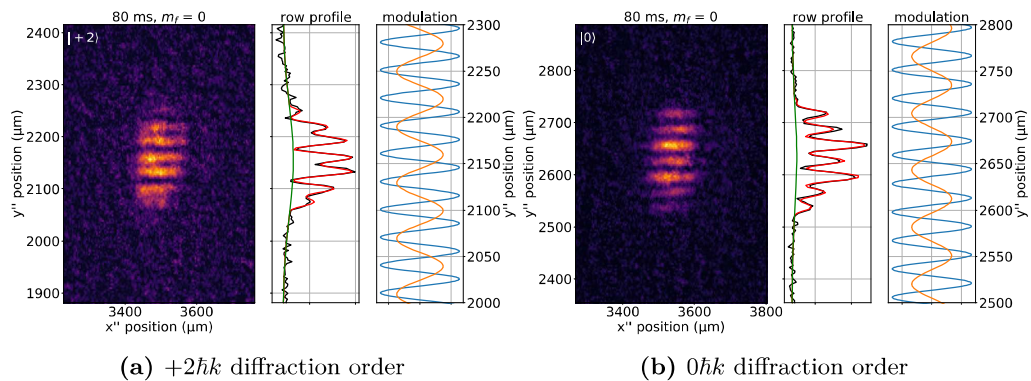


Figure 3.28: The $+2\hbar k$ and $0\hbar k$ diffraction order of an Open-Ramsey type interferometer in microgravity. Equation 3.60 was fitted to the row profile. The sinusoidal modulation is shown as well. The blue curve corresponds to the fringe spacing expected from the two BECs initially diffracted at the first $\pi/2$ -pulse, while the orange curve corresponds to the interference of the former two BECs with a BEC, which only (partially) diffracted at the second $\pi/2$ -pulse. More details in the text.

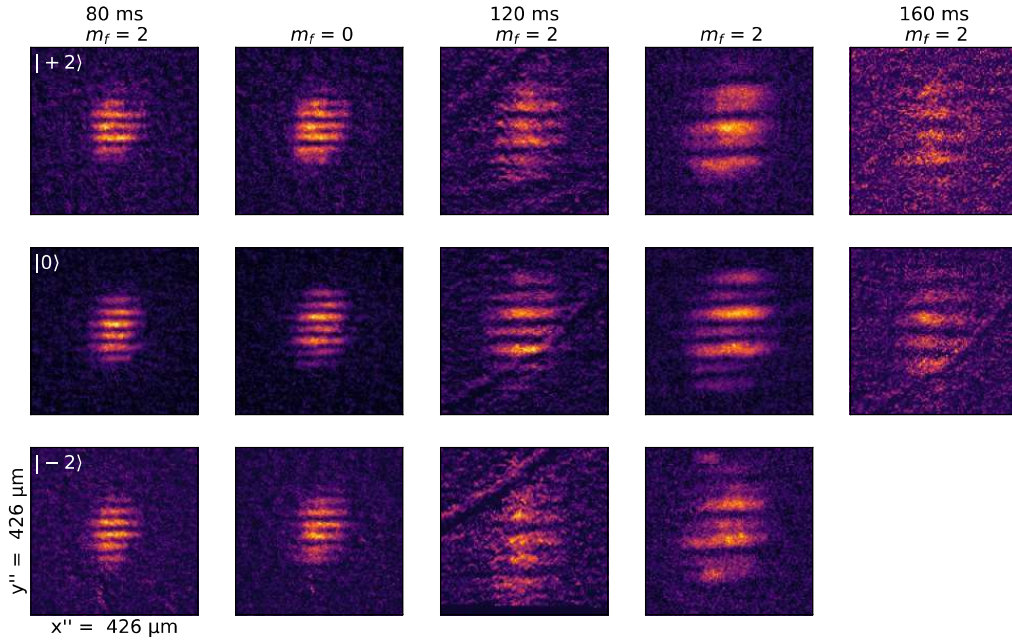


Figure 3.29: Open Ramsey type interferometer with unlened BECs in microgravity. The rows show BECs diffracted into the three orders $\pm 2\hbar k$ and $0\hbar k$ labeled $|\pm 2\rangle$ and $|0\rangle$, respectively. The first two columns show the absorption images after 80 ms time-of-flight and in the $m_f = 2$ and $m_f = 0$ states. The next two columns show atoms in the $m_f = 2$ after time-of-flight of 120 ms. The last column shows atoms in the $m_f = 2$ as well, but after a time-of-flight of 160 ms. The $|-2\rangle$ diffraction order was not visible due to the long time-of-flight. Experimental details and the discussion is in the text.

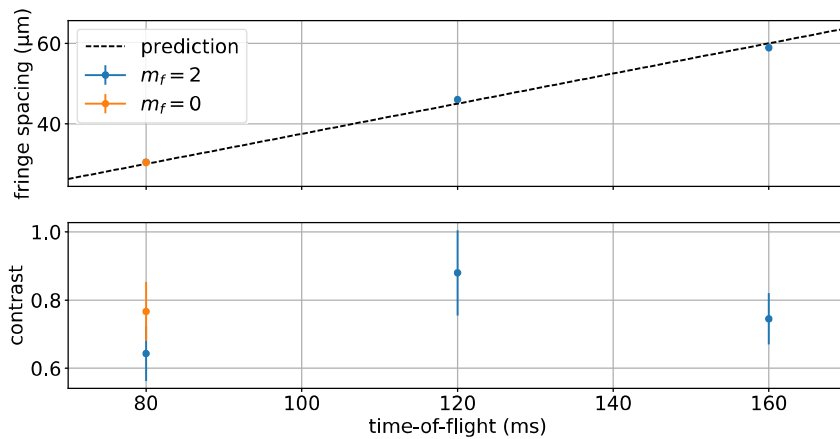


Figure 3.30: Analysis of the images from Figure 3.29. The images of the Open-Ramsey type interferometer sequence with unlened ensembles were analyzed. Equation 3.60 was fitted to all available diffraction orders. The mean and standard deviation of the resulting fringe spacing is plotted against the time of flight. The error bars in the fringe spacing plot are smaller than the markers. The prediction was calculated with Equation 3.42.

3.6 Atomic Shear Interferometer

In Section 3.1.4 the method of magnetic lensing was introduced. It allows to reduce the expansion velocity by several order magnitude. In the 2018 drop campaign the expansion velocity was reduced to $(v_x, v_y, v_z) = (77, 43, 53) \mu\text{m/s}$ [25] allowing for a detectability of the BEC after up to 17 s. The degree of collimation was determined by a time-of-flight series. For a fixed lens duration of 2.42 ms, which was determined before-hand by a simulation based the scaling-approach and ray-tracing, time-of-flight measurements between 200 ms and 2000 ms were performed. In analogy to optics, this corresponds to finding the optimal lens position of a collimator by minimizing the laser spot at a sufficiently great distance. During the 2020 drop campaign this method was verified by choosing magnetic lens durations of 2.0 ms, 2.2 ms, 2.42 ms, 2.70 ms, and 2.85 ms and determining the ensemble size after 1.5 s of time-of-flight with the secondary detection system. Figure 3.32 shows the gallery of the absorption images. The gallery verified that a magnetic lens of a duration of 0.22 ms shorter than the determined 2.42 ms lens and with a duration 0.28 ms longer leads to a greater spatial extent in the x'' - and y'' -direction. In optics the collimation of a laser beam is also often adjusted by a shear interferometer. In that case the laser beam is split and displaced by the two faces of a glass plate placed in the laser beam. The orientation of the interference pattern determines the degree of collimation. Figure 3.31 illustrates this method.

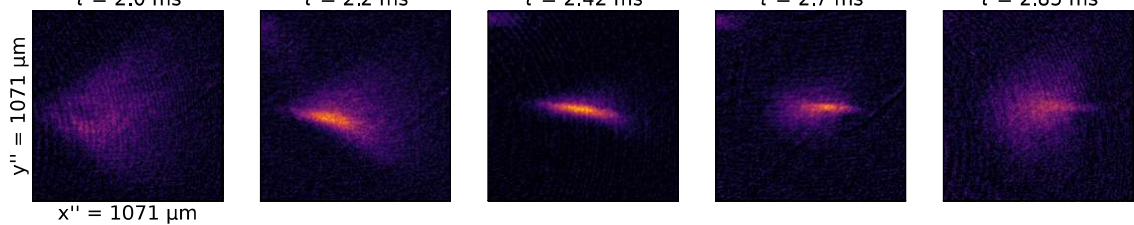


Figure 3.32: Cold atom clouds 1.5 s after the magnetic lens. The images were taken with the secondary detection system. The optimal lens duration is at 2.42 ms and measurements of two shorter and two longer magnetic lens durations were taken.

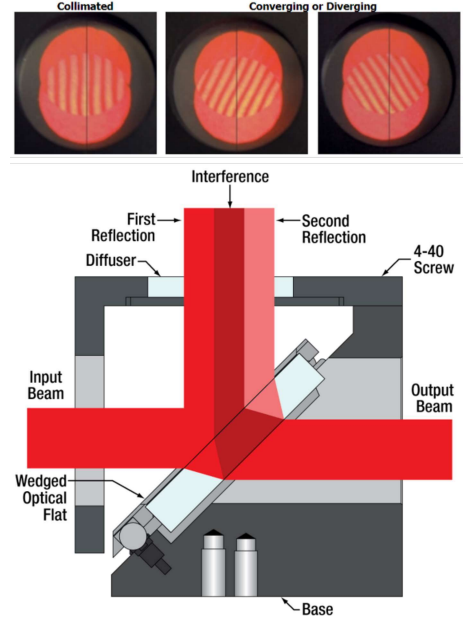


Fig. 3.31: Optical shear interferometer. Figure taken from thorlabs.com.

The displacement occurs as well in the Open-Ramsey type interferometer. The interrogation time T_{int} between the two $\pi/2$ -pulses can be seen as the thickness of the glass plate in the optical shear interferometer. From Equation 3.42 it follows that the fringe spacing is proportional to $1/T_{int}$ and to T_{TOF} , and independent of the magnetic trap prop-

erties. Hence, the Open-Ramsey type interferometer is not applicable for determination of the expansion velocity from a magnetic trap. Nevertheless, a magnetic lens changes the expansion velocity of the ensemble and this can be used to assign a *virtual time-of-flight* to a certain magnetic lens strength. Figure 3.33 illustrates this method. The better the ensemble is collimated the longer the *virtual time-of-flight* will be, leading to a greater fringe spacing. Therefore, the method of determining the collimation of a magnetic lens with an Open-Ramsey type interferometer was named *atomic shear interferometer* in analogy to the optical shear interferometer. The difference is the determination of the degree of collimation by the fringe spacing and not by the fringe orientation.

For the measurements the predictions from the *ParticleSim* [63] simulation were taken to calculate an interrogation time between the $\pi/2$ -pulses such that at least two fringes were visible in the resulting output ports. Hence, every lens duration had an individual interrogation time. The used separation times and expected fringe spacings are listed in Table 3.4. For the experimental sequence the BEC was released from the magnetic trap at position c , after 80 ms time-of-flight the magnetic lens¹ of varying duration was applied. Afterwards the atoms were transferred into the magnetic insensitive $m_f = 0$ state by means of an adiabatic rapid passage. 60 ms after the magnetic lens the Open-Ramsey type interferometer sequence was applied. The same pulse duration of 200 μs as in unlensed measurement was used. The interrogation times for the different lenses are listed in Table 3.4. After another 40 ms the atoms were detected with absorption imaging. The resulted absorption images of the three output ports taken with the secondary detection system are shown in Figure 3.34. Each column shows the primary shadows of the three output ports.

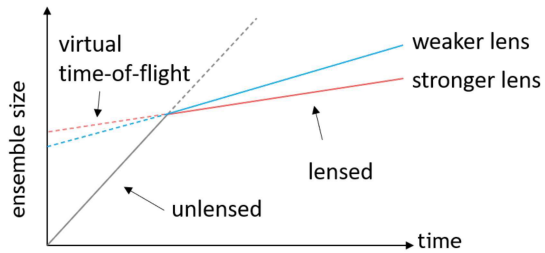


Fig. 3.33: Illustration of the *virtual time-of-flight* principle in the atomic shear interferometer.

¹ *BaseChip* Z current of 1.828 A, x-bias coil current of 0.1 A, y-bias coil current of -0.0754283 A, and z-bias coil current of -0.0038 A

Table 3.4: Measurement parameters and fit results of the atomic shear interferometer. The separation was calculated from the interrogation time by $4\hbar k T_{int}$. The cloud size and the expected fringe spacing d_{sim} was calculated with the *ParticleSim*. The fringe spacing d_{exp} was determined by fitting the images in Figure 3.34.

Drop	τ_{lens} (ms)	T_{int} (μs)	Separation (μm)	Cloud Size (μm)	d_{sim} (μm)	d_{exp} (μm)
289	0.75	780	9.2	230	62.2	59.8 ± 1.5
300	1.00	850	10.0	216	62.5	65.2 ± 3.6
291	1.50	1054	12.4	189	64.8	69.1 ± 4.8
292	2.00	1535	18.1	163	71.3	82.1 ± 0.8
294	2.20	2574	30.3	153	58.6	139.5 ± 4.5
313	2.70	2302	27.1	156	58.8	53.2 ± 7.0
296	2.85	1813	21.3	163	59.3	52.1 ± 7.4
295	3.25	1406	16.5	184	51.7	51.9 ± 11.0

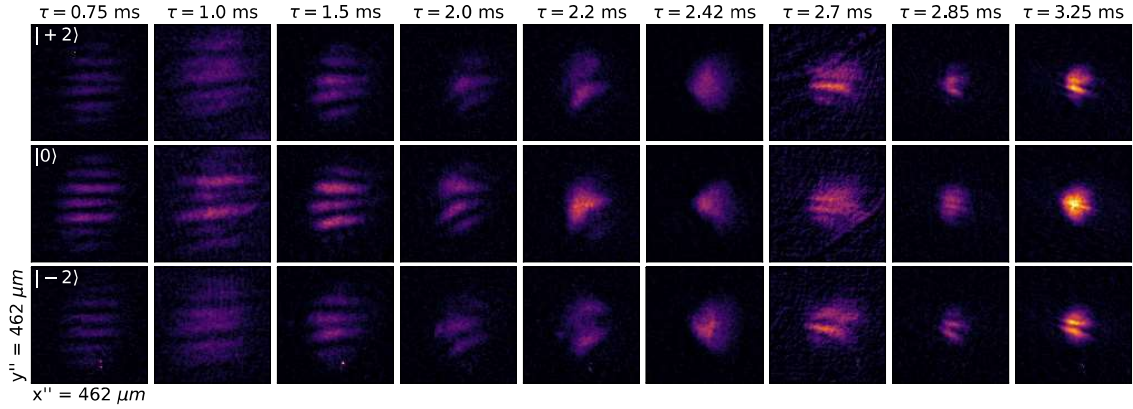


Figure 3.34: Atomic shear interferometer gallery. The three output ports of an Open-Ramsey type interferometer for different magnetic lens durations are shown. The magnetic lens was applied 80 ms after release from the final magnetic trap. After another 60 ms the two $\pi/2$ - pulses were performed. The absorption images were taken after 40 ms time-of-flight. The time between the $\pi/2$ - pulses was chosen such that two fringes would be visible according the particle simulation.

For the analysis the images were rotated such that the fringes were as horizontal as possible. The part of the rotated images containing the cold atom clouds were divided in four columns (see Figure 3.35). The rows of these columns were summed up and a Gaussian function modulated by a sinusoidal function was fitted to the data

$$f(x) = \left[1/2 + C/2 \sin \left(2\pi \frac{x - x_c}{d} + \phi \right) \right] \cdot A_1 \exp \frac{-(x - x_c)^2}{2\sigma^2}, \quad (3.61)$$

where C is the contrast, x_c the center of the Gaussian function, d the fringe spacing, ϕ the phase of the modulation relative to the center position, A_1 the amplitude of the Gaussian function, and σ the width of the Gaussian function. Equation 3.60 was not chosen as a fit-function, because the profile of the lensed ensemble does not agree with Gaussian plus Thomas-Fermi function due to anharmonicities of the lens potential.

The mean and standard deviation of the fitted fringe spacing were normalized to an interrogation time of $500 \mu\text{s}$ by $d_{norm} = d \cdot \frac{T_{int}}{500\mu\text{s}}$.

Figure 3.36 shows the normalized fringe spacings plotted against the lens duration and the expected fringe spacings calculated by the *ParticleSim* simulations. For lens durations smaller than 2.2 ms the data points agreed with the simulated curve and the error bars are small. Fringe spacing values for lens duration longer than 2.42 ms agree as well with the simulated curve, but have much greater error bars. This is consistent with the absorption images in Figure 3.34, where the interference pattern shows almost parallel fringes for up to 2.0 ms lens duration. Afterwards, the deformation of the wavefront decreases the certainty of the fit. The data point at 2.2 ms stands out at a fringe spacing of more than double the expected amount.

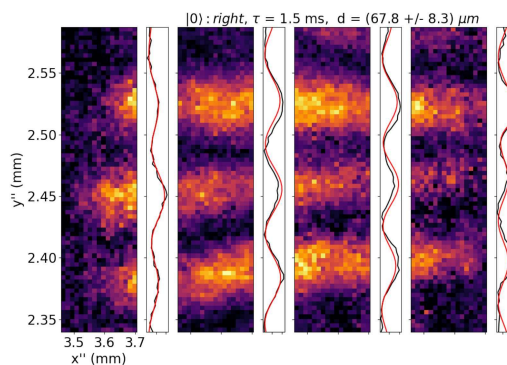


Fig. 3.35: Fit of the $|0\hbar k\rangle$ port for $\tau = 1.5$ ms.

Afterwards, the deformation of the wavefront decreases the certainty of the fit. The data point at 2.2 ms stands out at a fringe spacing of more than double the expected amount.

All of the error sources discussed in Section 3.5 also apply in this case. Additionally, the magnetic lens introduces a major source of uncertainties. Depending on the duration of the lens, inter-atomic interactions cannot be neglected. Additionally, the magnetic potential is not purely harmonic, but has anharmonicities of third and fourth order [34]. This leads to an asymmetric force on the atoms and causes a tail in the spatial atomic distribution. Moreover, the possibility of a fringe spacing having a two-fold size due to inefficient beam-splitter pulse needs to be considered and is especially important in case of the data point at a lens duration of 2.2 ms.

Additionally, the coherence length for lens duration of 0.75 ms to 2.00 ms were estimated by fitting Equation 3.60 to the sum of rows of the absorption images. With the interrogation time and the Thomas-Fermi radius in the y-direction listed in Table 3.4 the fit resulted in a coherence length of 20 % - 30 % of the Thomas-Fermi radius¹. This is lower than the 35 % - 50 % estimate for the unlensed Open-Ramsey type sequence. A possible reason for the decrease of the coherence length could be dephasing due to anharmonicities of the lensing potential. The potential further away from the atom chip is smaller and causes the phase of the atoms closer to the atom chip to evolve faster. Nevertheless, the coherence length should be sufficient to investigate an asymmetric Mach-Zehnder interferometer geometry

¹ The uncertainty stems from fits of different orders and variation of the initial contrast between 0.85 and 1.0.

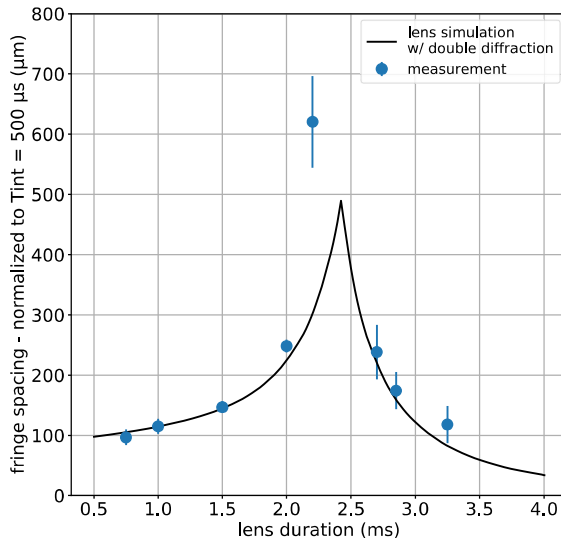


Figure 3.36: Evaluation of the atomic shear interferometer gallery (Figure 3.34). Each image of a cloud was rotated such that the fringes were as horizontal as possible. Afterwards each image was split into four columns. A Gaussian modulated by a sinusoidal function was fitted to the sum of rows in each column. The mean and the standard deviation of the fringe spacing for each lens duration was normalized for an interrogation time of $500 \mu s$. The solid black line shows the expected fringe spacing from the *ParticleSim* simulation. All data points except the data point at $\tau_{lens} = 2.2$ ms agree with the simulation within the uncertainty.

with magnetically lensed Bose-Einstein condensates where dephasing could additionally occur due to the greater spatial separation during an interferometer sequence.

3.7 Asymmetric Mach-Zehnder Interferometer

The next step towards implementing atom interferometers on long timescales is perform measurements with a Mach-Zehnder interferometer. The MZ interferometer can be executed in the symmetric and asymmetric configuration (see Section 3.1.5). The asymmetric MZ interferometer has the advantage of determining the contrast of the interferometer with one measurement. This is the same contrast as discussed in the previous sections, namely a contrast proportional to the coherence length of the ensemble at the time of the interference. To this contrast will now be referred as to single-shot-contrast. The term *contrast* in a symmetric MZ interferometer refers to the amplitude of the sinusoidal oscillation between the population of the output ports of the interferometer when changing a parameter like α (see Section 3.1.5).

By measuring the single-shot-contrast at the time of the beginning of the MZ interferometer sequence with an Open-Ramsey type interferometer and comparing this value to the single-shot-contrast of the asymmetric MZ interferometer one can deduce the dephasing of the BEC during the MZ interferometer sequence. This dephasing would also reduce the contrast of the symmetric MZ interferometer. This does not necessarily guarantee a measurable contrast in the symmetric configuration of the MZ interferometer. Vibrations of the retro-reflective mirror or drifts of the laser phase during the sequence would reduce the

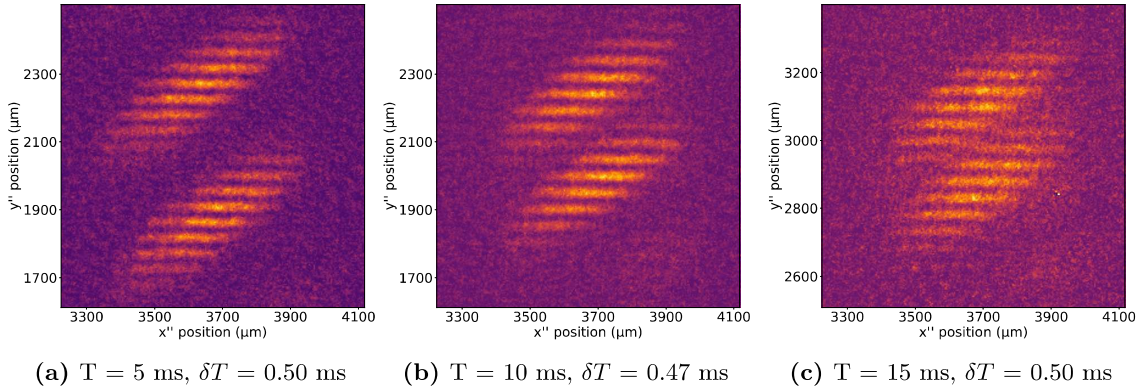


Figure 3.37: Asymmetric Mach-Zehnder interferometer with single diffraction. The measurement was performed for three different interrogation times of 5 ms, 10 ms, and 15 ms. The atoms were released from the magnetic trap such that they follow the trajectory *parabola2*. In the first two cases the first $\pi/2$ -pulse was applied 14.5 ms after release from the magnetic trap. In the last case the $\pi/2$ -pulse was applied 9.5 ms after release to maximize the separation between the two ports. For (a) and (b) the total time-of-flight was 57.5 ms and for (c) 60.5 ms. The absorption images were taken from the secondary detection system.

contrast further. Moreover, no measurable single-shot-contrast at the beginning of the MZ interferometer sequence does not imply no measurable contrast in the symmetric MZ interferometer sequence. The single-shot-contrast of ensemble with short coherence length, such as thermal ensembles, might not be measurable, but this does not imply a dephasing during the MZ interferometer sequence.

Measuring the contrast of a symmetric Mach-Zehnder interferometer in microgravity is very challenging. Due to the limit of 3 drops per day, a measurement of the contrast of the symmetric MZ interferometer would take several weeks. An asymmetric Mach-Zehnder interferometer offers the possibility to investigate the dephasing of the ensemble by performing single-shot-contrast measurements. This would allow to estimate the maximal possible interrogation time T of a symmetric Mach-Zehnder interferometer under the assumption that the vibration of the retro-reflective mirror and the laser phase are stabilized during the MZI sequence.

Measurements with the asymmetric Mach-Zehnder interferometer were performed on ground with interrogation times¹ $T = 5$ ms, 10 ms, and 15 ms. The trajectory *parabola2* was used to maximize the interferometer duration. For $T = 5$ ms and 10 ms the initial $\pi/2$ -pulse was applied at 14.5 ms after release from the magnetic trap at the same time as the Open-Ramsey type interferometer measurement. This allowed for investigation of the dephasing during the interferometer sequence. For $T = 15$ ms the initial $\pi/2$ -pulse was applied 5 ms earlier at 9.5 ms after release from the magnetic trap. This was done to maximize the separation between the output ports. The last $\pi/2$ -pulse was applied 0.5 ms to 0.2 ms earlier in case of $T = 5$ ms and $T = 15$ ms measurement and 0.47 ms to 0.17 ms

¹ The interrogation time in case of the MZ interferometer is different to the interrogation time of the Open-Ramsey type interferometer, which is denoted T_{int}

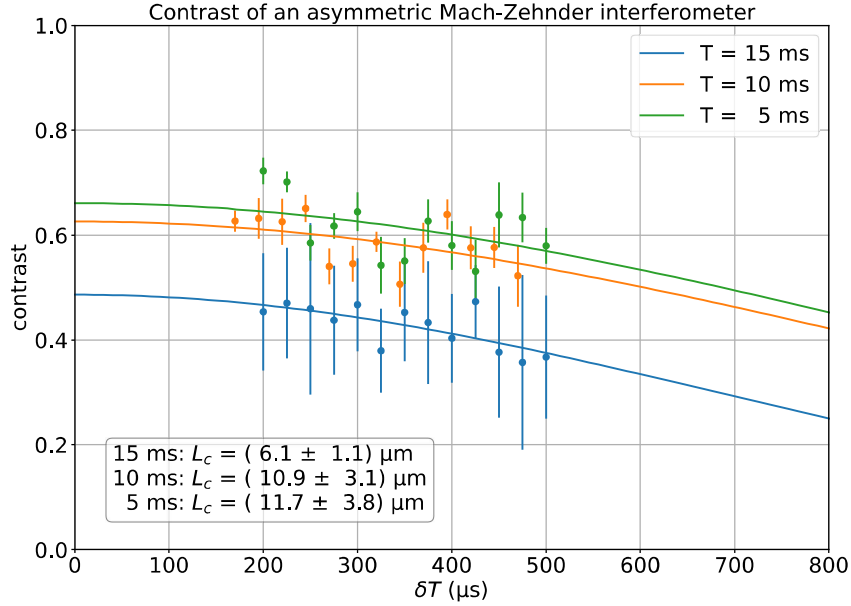


Figure 3.38: Contrast of the asymmetric Mach-Zehnder interferometer. For three different interrogation times the contrast as a function of the asymmetry of the last $\pi/2$ -pulse δT was measured. The contrast was determined by fitting Equation 3.59 to the sum of rows of the according absorption image. The contrast decay was modeled by a Gaussian as described in Section 3.4 and from the time δT , where the contrast reached a value of $1/e$ was the coherence length calculated.

earlier in case of $T = 10$ ms. The steps size was 0.025 ms. The difference in the $T = 10$ ms measurement is due to a mistake in the setting of the measurement. The atoms were not transferred to the $m_f = 0$ state and remained in the magnetically sensitive state $m_f = 2$. After a total time-of-flight of 57.5 ms in case of $T = 5$ ms and 10 ms and of 60.5 ms in case of $T = 15$ ms the atoms were detected from the secondary detection system. The measurements were repeated 10 times. The absorption images of for the longest δT are shown in Figure 3.37. To extract the contrast and the fringe spacing the images were processed like the images in Section 3.5. A triangular shaped covered the lower port with a region of the images without atoms and Equation 3.59 was fitted to the sum of rows. The resulting contrast is shown in Figure 3.38 and the fringe spacing in Figure 3.39. The fringe spacing was calculated the same way as in an Open-Ramsey type interferometer, because applying a $\pi/2$ -pulse δT seconds before the complete overlap of the two ports is equal to separating the BEC for a time $T_{int} = \delta T$. This introduces a center-of-mass difference of $\delta x = 2\hbar k\delta T$.

The decay of contrast as a function δT was fitted with a Gaussian function resulting in a coherence length of $L_c = (11.7 \pm 3.8) \mu\text{m}$, $(10.9 \pm 3.1) \mu\text{m}$, and $(6.1 \pm 1.1) \mu\text{m}$ for interrogation times of 5 ms, 10 ms, and 15 ms, respectively. In Section 3.4 a coherence length of $(6.9 \pm 0.4) \mu\text{m}$ was measured. This is two standard deviations below the coherence length for $T = 5$ ms and 10 ms, and equal within the uncertainty to the coherence length

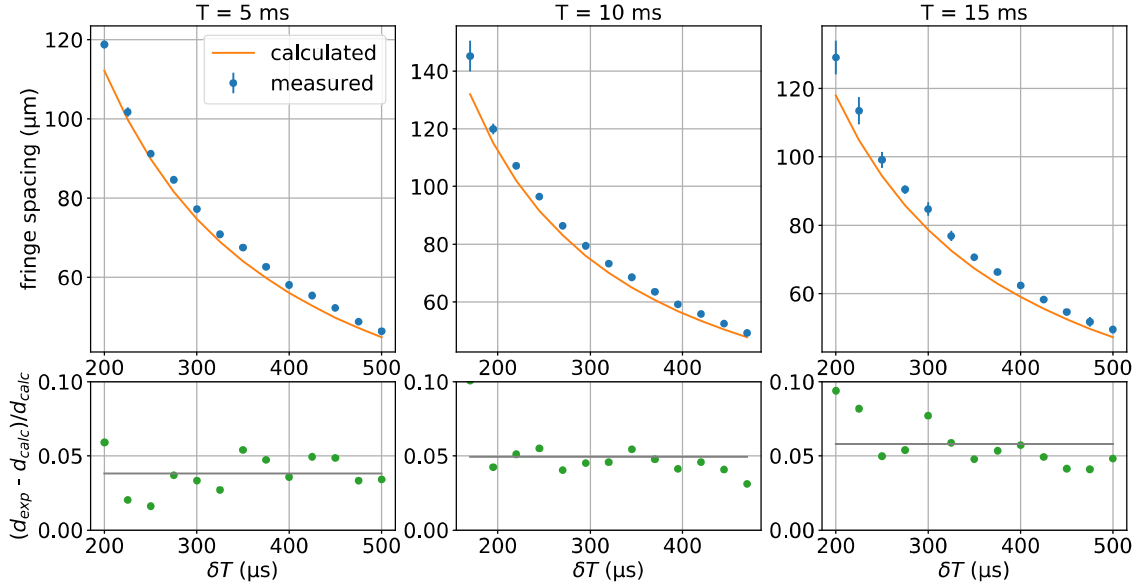


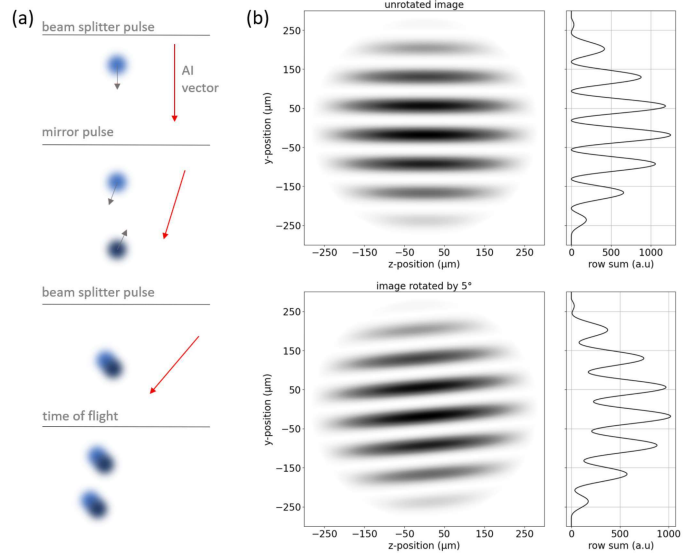
Figure 3.39: Fringe spacing in the asymmetric Mach-Zehnder interferometer. The time point of the last $\pi/2$ -pulse was varied for three interferometers with interrogation times of 5 ms, 10 ms, and 15 ms. The last $\pi/2$ -pulse was applied δT earlier. The fringe spacing was determined by fitting Equation 3.59 to the sum of rows of the according absorption images. The expected fringe spacing was calculated with Equation 3.42. The measured fringe spacing located systematically above the calculated one and the difference increases with the interrogation time.

for $T = 15$ ms. This leads to the conclusion that during the interferometer time $2T \approx 10$ ms, 20 ms, and 30 ms no dephasing is observed.

Figure 3.39 shows a deviation of the measured and calculated fringe spacing. The measured fringe spacing is always greater than the calculated one and the deviation increases with the time in the interferometer. The mean deviation $(d_{exp} - d_{calc})/d_{calc}$ is $(4 \pm 1) \%$, $(5 \pm 2) \%$, and $(6 \pm 2) \%$ for interrogation times of $T = 5$ ms, 10 ms, and 15 ms, respectively. Fringe spacing deviations were as well observed in the QUANTUS-1 experiment [67] in case of the asymmetric Mach-Zehnder interferometer. They could reduce the deviations between the prediction and the measurement by calculating the fringe spacing with a magnetic trap model instead of assuming a cigar shaped condensate with the weak axis perpendicular to the AI axis. The later case was used in this thesis to calculate Equation 3.42. The deviation between measured fringe spacing and calculated fringe spacing in the single diffraction and double diffraction Open-Ramsey type interferometer is $(-0.3 \pm 2) \%$ and $(0.3 \pm 1) \%$, respectively. In case of the asymmetric MZ interferometer and the OR type interferometer the BEC was released from the same magnetic trap excluding the the calculation of the fringe spacing as a source. Therefore, the reason for the deviation needs to stem from the Mach-Zehnder geometry, likely in the separation of the center-of-masses.

Rotation In microgravity another effect, which might reduce the contrast need to be considered. The normal vector of the fringe planes \vec{v}_f is parallel to the vector connecting the center-of-masses of the interfering BECs \vec{v}_c . On ground \vec{v}_c points in the direction of the AI beam. The AI beam is oriented in the x-y plane, with a 7° inclination to the y-axis. Hence, the \vec{v}_f vector is perpendicular to the z-axis along which the absorption imaging occurs. However, the capsule rotates during a drop. The rotation rate in the y-z plane is up to $0.1^\circ/\text{s}$. This rotation causes the \vec{v}_c vector to rotate and this in turn causes the \vec{v}_f vector to rotate with respect to the z-axis. Taking this together, leads to a reduction of the contrast as illustrated in Figure 3.40. The exact effect depends on the size of the ensemble in the z-direction and on the rotation rate, which varies from drop to drop. Additionally, the rotation causes a center-of-mass movement of the interfering BECs. This requires a modification of the derivation of Equation 3.42 for the fringe spacing.

Figure 3.40: Illustration of the effects of the capsule rotation on an asymmetric Mach-Zehnder interferometer. (a) illustrates the effect of AI vector rotation on the center-of-mass displacement after the second beam splitter pulse. (b) shows the reduction of contrast due to a center-of-mass vector rotated by 5° .



3.8 Mach-Zehnder Interferometer

In this section a symmetric Mach-Zehnder interferometer measurement will be presented. This will allow to compare the single-shot-contrast to the contrast of the sinusoidal oscillation between the population of the output ports of the symmetric Mach-Zehnder interferometer. Furthermore, this measurement will allow check the longterm stability, identify sources of noise, and to compare the performance of the QUANTUS-2 apparatus to the QUANTUS-1 apparatus [49]. A measurement of the gravitational acceleration along the Bragg lattice was performed. Due to 7° tilt of the atom interferometry (AI) beam to the atom chip and no reliable way to align the AI axis with gravity only the projection on the gravitational acceleration on the AI beam direction was measured. This measurement was sufficient to investigate the longterm stability and compare the apparatus to the QUANTUS-1 apparatus.

The Bose-Einstein condensate was accelerated on the trajectory *parabola1*. This trajectory was chosen, because it allowed for a more reliable determination of the atom number due

to its symmetric shape. On the way to the apex the atoms were transferred in the $F = 2$, $m_f = 0$ state by means of adiabatic rapid passage. After the apex the Mach-Zehnder sequence began. For the measurement Gaussian shaped pulses were used with a full duration of $80 \mu s$. The π -pulse was achieved by doubling the laser power. After a time-of-flight the population of the two output ports were determined with absorption imaging from the primary detection system. For a measurement the detuning of the second and third pulse was scanned. It was calculated in the following way:

$$\begin{aligned}\Delta_{2p} &= \Delta_{1p} + (T + 80\mu s)\alpha \\ \Delta_{3p} &= \Delta_{2p} + (T + 80\mu s)\alpha,\end{aligned}\tag{3.62}$$

where Δ_{1p} , Δ_{2p} , and Δ_{3p} are the detunings of the first, second, and third pulse. T is the interrogation time and α the detuning shift due to the gravitational acceleration. The detuning of the first pulse was determined to be 61 kHz by maximizing the diffraction efficiency of a π -pulse. For interrogation times of $T = 2$ ms, 3 ms, and 5 ms α was scanned from 24.87 kHz/ms to 25.07 kHz/ms in 0.002 kHz/ms steps. The resulting fringes can be seen in Figure 3.41. The function $C/2 \sin(\omega * x + \phi) + d$ was fitted to the data. C is the fringe contrast, x , the acceleration, ω , the angular frequency, ϕ the phase, and d the offset. This resulted in a contrast of 85 %, 75 %, and 62 % for interrogation times of 2 ms, 3 ms, and 5 ms respectively. The fringe minimum for $T = 5$ ms, which was a located closest to the minima of the other interrogation times was located at $9.7474 m/s^2$ or $\alpha = 24.986$ kHz/ms. A long term measurement was performed for $T = 5$ ms. Therefore, 21 data points around $\alpha = 24.986$ kHz/ms were measured and a sinusoidal fit was fitted to the data to determine the minimum. This resulted in a value for the acceleration. This procedure was repeated 93 times over 5h and 30 min. The resulting values for the acceleration and the overlapping Allan deviation [68] are shown in Figure 3.42. This measurement contrasted the other measurements presented in this chapter by extracting the fringes not from a single measurement, but taking a series of measurements with different detunings. Additionally, the duration of 5h30min allowed to benchmark the stability of the QUANTUS-2 apparatus on long time scale. The sensitivity of the experiment is $3.6 \cdot 10^{-3} (m/s^2)/\sqrt{Hz}$ and long term stability is $3.2 \cdot 10^{-5} m/s^2$ after 5h30min. During the measurement we were limited by the shot noise limit. While some of the sources of uncertainty of previous chapters do apply for this measurement, several others are not problematic in this measurement:

- **Resolution limit of the imaging system:** In this measurement the atom number in the two output port were determined by a fit to the sum of columns and rows. Details in the range of the resolution limit of $7.81 \mu m$ were not necessary for the analysis of the data.
- **Calibration of the magnification:** The atom number in the output ports were determined by fitting a gaussian function to the two output ports and determine the atom number by $N = \sqrt{2\pi} \cdot A \cdot \sigma$, where A is the amplitude of the Gaussian and σ the width. A systematic deviation of the calibration would lead to a deviation of the width, but due to the relative population determining the fringe position, it cancels out.

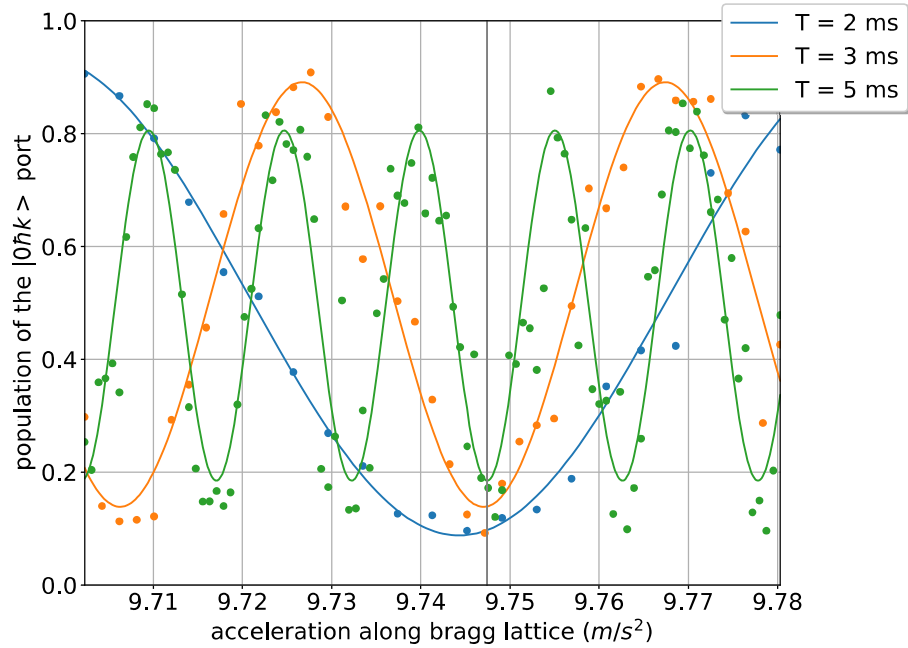


Figure 3.41: Fringe scan at different interrogation times of the Mach-Zehnder type Interferometer with single diffraction. Each data point was averaged three times. The common minimum of all three fringe scans is located between 9.74 m/s^2 and 9.75 m/s^2 . The contrast is 85 %, 75 %, and 62 % for interrogation times of 2 ms, 3 ms, and 5 ms respectively. The fringe minima at lower interrogation times are at a lower value due to non-negligible pulse duration to interrogation time ratios.

- **Thermal atom background:** The pulse duration was chosen short enough to depopulate the ground state to below 5 % (see Section 3.3). Typically, the ensemble contained over 10 % of thermal atoms. Hence, thermal atoms were as well diffracted as condensed atoms.

Other effects do contribute to the uncertainties of this measurement:

- **Variations in the diffraction efficiency:** Variations in the diffraction efficiency lead to the reduction of the contrast. Atom not diffracted at the π - pulse reduce the contrast by reducing the total number of atoms and atoms not correctly addressed by a $\pi/2$ - pulse reduce the contrast of the fringe pattern by not transferring all atoms to the ground state at the frequency rate compensating the gravitational acceleration. In addition, shot-to-shot variations of the diffraction efficiency lead a deviation from a sinusoidal fringe shape and an uncertainty of the determination of fringe minimum.
- **Phase of the laser beams:** Phase drifts of the two laser beams during the MZI sequence would add additional phases to Equation 3.53 and change the additional gravitational acceleration. Figure 3.16 shows the phase approximately in the same state as during this measurement (around 18:00 after a full day of measurements). The phase measurements are 8 s apart and show a shot-to-shot variations of 53 mrad.

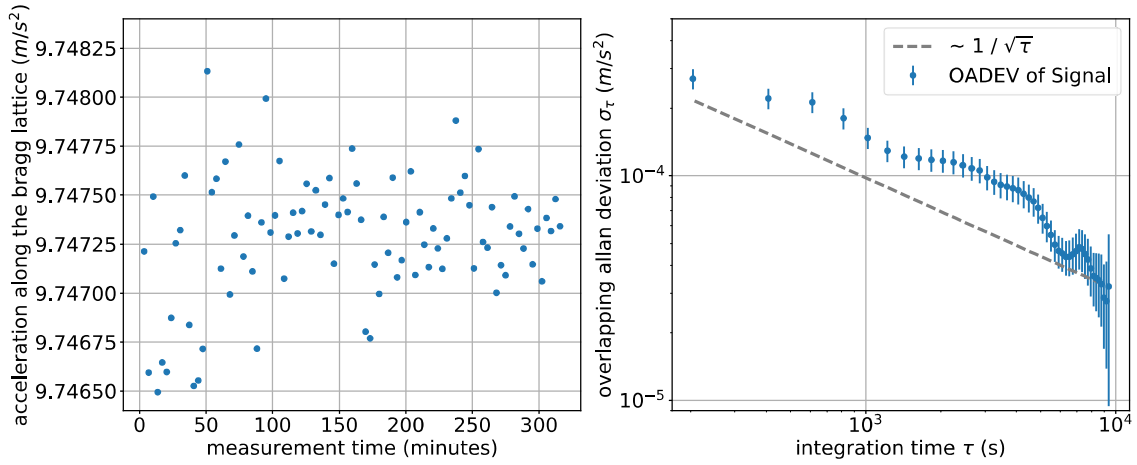


Figure 3.42: Measurement of the acceleration of the Bragg lattice. With an interrogation time of 5 ms 21 data points around the minimum found in Fig. 3.41 were taken. This measurement was repeated 93 times to determine the precision of the apparatus and to investigate contributing noise sources. The right graph shows the calculated Allan deviation and the shot noise limit for a contrast of 0.62 and an atom number of 40000. The experiment is running at the shot noise limit and its performance can only be increased by increasing the contrast, atom number, or the repetition rate.

If we assume the error between the MZI pulses is the same, although it is likely that it is smaller, because the pulses are 5 ms apart and not 8 s, we will get an uncertainty of $8.3 \cdot 10^{-4} \text{ m/s}^2$ per shot.

- **Wavefront aberrations:** The advantage of using BECs for atom interferometry is their small size compared to the beam profile. We used a collimator with an $1/e^2$ -diameter of 3.31 mm. Figure 3.43 shows the position and the size of BEC for a time-of-flight of 1 ms to 34 ms after release from the magnetic trap. The size of the ensemble is approximately $50 \mu\text{m}$ and hence 2 orders of magnitude below the diameter of the laser beam. The drift during the 3 pulse sequence in z direction is $37 \mu\text{m}$ and small as well. The laser beam is oriented in y-direction with a tilt of 7° in x-direction. The fall of the atoms along the y-direction is not problematic, because it is almost along the k-vector of the laser beam. The 7° tilt contributes to a drift in x-direction. The drift in x-direction amounts to $80.7 \mu\text{m}$ and is far below the laser beam diameter. Nevertheless, wavefront aberrations stemming from impurities on the vacuum windows or diffraction from the atom chip could have had an effect on the results.
- **Variation of the BEC release:** A variation of the detuning of 2.75 kHz was determined by investigating the release mechanism. This detuning does not influence the measurement of the α factor, because it only reduces the efficiency of the first $\pi/2$ - pulse.
- **Residual magnetic field gradients:** The residual magnetic field gradient was measured to be around 1 G/m. Due to the atoms being in the $m_f = 0$ state only

the quadratic Zeeman effect needs to be considered. With an value of $0.575 \text{ kHz}/G^2$ [69] and a constant bias field of 0.9 G. This only leads to an acceleration of $3.8 \cdot 10^{-7} \text{ m/s}^2$.

- **Fitting error - single shot:** Errors in the fitting process lead to uncertainties in the atom number determination. The cold atom clouds were fitted with a sum of two Gaussian function, although, they contained thermal atoms and condensed atoms. This was done due to fit stability. A fitting function with a sum of two functions consisting of a Gaussian function and a Thomas-Fermi profile is less stable. The deviation was estimated by comparing the total number of atoms with a pure Gaussian fit and a combination of a Gaussian and a Thomas-Fermi profile for 100 data points. This led to an offset of $(3.0 \pm 0.5) \%$. The offset cancels out in the determination of the relative population, but the standard deviation of the offset of 0.5 % contributes to the phase determination. However this averages out, because 21 data points are taken to determine the minimum of the fringe.
- **Fitting error - single fringe:** Per measured fringe was a sinusoidal function fitted to the 21 points. The uncertainty of this function is the first point in the Allan deviation plot: $2.7 \cdot 10^{-4} \text{ m/s}^2$

Taken together, the uncertainty in the phase of the laser beams at the times of the pulses and the single fitting errors should averaged out in a measurement of a fringe. Residual magnetic field gradients are 2 orders magnitude below the long time stability of $3.2 \cdot 10^{-5} \text{ m/s}^2$. The uncertainty of the fringe position determination is the greatest source of uncertainty and likely stems from the variation of the diffraction efficiency.

Contrast vs. single-shot-contrast In the previous section it was shown that no measurable dephasing during the $T = 5 \text{ ms}$ and 10 ms asymmetric Mach-Zehnder interferometer measurements was observed. This was done by measuring the single-shot-contrast of the spatial interference of a split Bose-Einstein condensate as a function of split distance. Hence, the decay of the single-shot-contrast is a measure for the coherence length. By investigating the coherence length at the beginning of the Mach-Zehnder interferometer sequence and at the end it is possible to determine the dephasing during the sequence. On the other hand, the contrast introduced in this section is the amplitude of the population oscillation due to variation of the α parameter. Loss of contrast occurs due to dephasing of the ensemble, vibrations of the retro-reflective mirror, drifts of the laser phase during the Mach-Zehnder interferometer sequence, and perturbations of the ensemble due to varying electric or magnetic fields.

In this measurement it was observed that the contrast decreases from 85 % to 62 % by increasing the interrogation time from 2 ms to 5 ms. Dephasing as a source was excluded by the single-shot-contrast measurement. The likeliest reason for the decrease of contrast are vibrations of the retro-reflective mirror and drifts of the laser phase. Residual magnetic fields have been excluded in the discussion before.

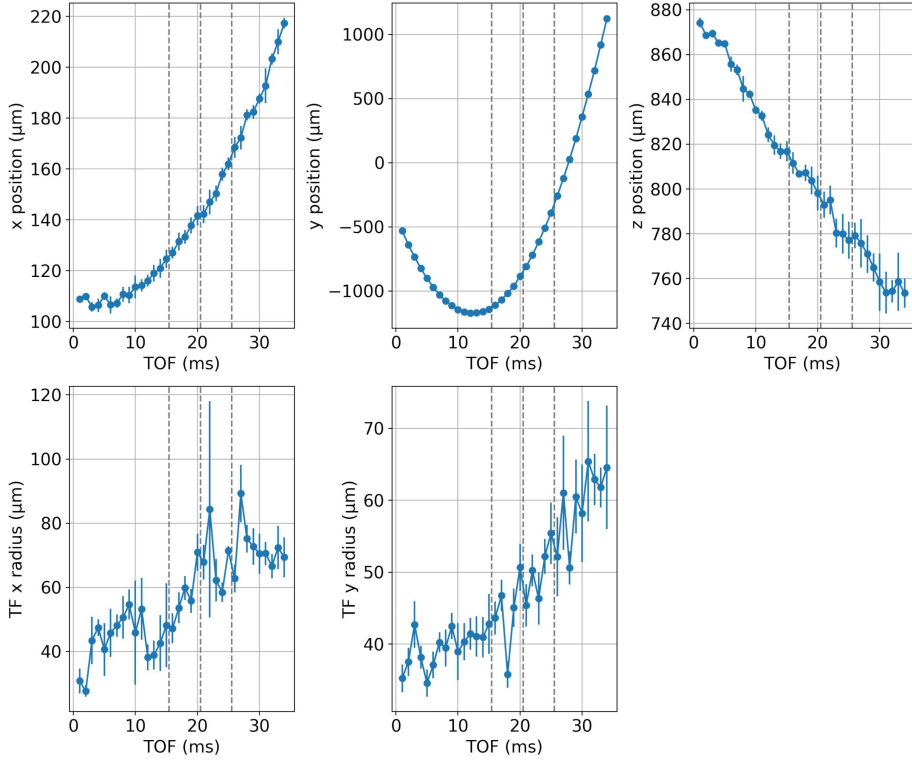


Figure 3.43: The position and the size of the BEC during the Mach-Zehnder sequence. The ensemble was imaged with the secondary detection system 1 ms to 34 ms in 1 ms steps after the release from the magnetic trap. The error bars were calculated from 3 measurements. The three dashed lines indicate the three pulses of the Mach-Zehnder interferometer. The middle line does not indicate that the atoms are $120 \mu\text{m}$ apart at the π - pulse in the y-direction (7° tilted in the y-x plane).

3.9 Summary and Conclusion

This chapter showed that it is possible to reproducibly achieve single and double diffraction efficiencies over 90 % on ground and in microgravity with the QUANTUS-2 apparatus. This allowed for implementation of Open-Ramsey type and Mach-Zehnder interferometers. The Open-Ramsey type interferometer measurements verified the predictions for fringe spacing. The coherence length of the ground experiments was between 7 % - 10 % of the Thomas-Fermi radius. In microgravity with unlensed BEC the coherence length was much higher at 35 % - 50%. The combination of the magnetic lens with the Open-Ramsey type interferometer showed a decrease of the coherence length to 20 % - 30 % for shorter lens durations. It was not possible to extract the coherence length from a BEC lensed with a duration close to optimal collimation from the current dataset. The atomic shear interferometer measurement showed a new method for determining the focus of a magnetic lens along the atom interferometry beam direction. This could be used in future measurements when characterizing a new magnetic lens. The asymmetric Mach-Zehnder measurements on ground showed little to no dephasing during the MZ sequence. While

the longest interrogation time of 15 ms showed a comparable coherence length to the Open-Ramsey type interferometer the two shorter interrogation times had higher coherence lengths. The comparison to the symmetric MZ interferometer allowed to exclude dephasing as the cause of the decrease of contrast with the interrogation time. The likely reason for the decreasing contrast are vibrations of the retro-reflective mirror and laser phase noise. Additionally, the long duration measurement of the gravitational acceleration along the atom interferometry axis showed that the long term stability improves at the shot-noise limit.

CHAPTER 4

Shell Potentials

Cold atoms are typically trapped with laser light or magnetic fields. Atoms can for example be trapped at the maximum of a Gaussian beam by dipole forces or at the minimum of a magnetic field. New methods of trapping atoms allowed to manipulate them in new ways and to investigate new phenomena. The magnetic trap allowed to cool atoms to degeneracy and to achieve the first Bose-Einstein condensate [56, 57]. Intersecting laser beams allow to trap atoms at the minima or maxima of the resulting interference pattern [70]. That allowed to study models of condensed-matter theory in an experimental setup, such as the Hubbard model [71].

In 2001 a new method of trapping atoms was proposed by Zobay and Garraway [28] and in 2004 realized by Colombe *et. al.* [72]. This method relies on transferring atoms from bare states trapped in a magnetic trap to dressed states by coupling magnetic sub-states of a hyperfine ground state with a radio frequency field or coupling different hyperfine states with microwave fields. Geometries such as a double well [73], a torus [74], or a shell [72] can be realized. Shell potentials have recently attracted more attention due to increasing number of experiments performed in microgravity [21, 22, 75]. The lack of gravity allows to distribute the atoms more evenly on the shell. By releasing ultra-cold atoms from the shell one could observe self-interference effects and investigate how different parts of the shell interfere with each other [29]. Another promising field of study are vortices on a curved surface. A different behavior in comparison to vortices on a flat surface is expected due to the curvature and the unbound surface [30].

The aim of this chapter is to describe the necessary steps to implement shell potentials at the QUANTUS-2 experiment in microgravity. With the help of a simulation, ellipsoid shaped shell potentials will be realized. Their dependence on the RF frequency and power will be studied. Different positions will be compared, and the occupation of the shell potentials with thermal atoms of different temperature will be investigated. Finally, in lifetime measurements the RF power will be identified as the limiting factor for successfully transferring Bose-Einstein condensates to shell potentials in the QUANTUS-2 apparatus.

This chapter will start with section 4.1, where a short overview of the theoretical background will be given. Section 4.2 will present the used hardware for the experiments. Then in Section 4.3 the implementation of the simulation and the according results will be treated. The experimental part of this chapter will start at Section 4.4, where preparatory measurements will be presented. Section 4.5 will present the method of transferring atoms from the bare states to dressed states. In Section 4.6 the measurements of the minimal coupling strength in microgravity will be presented. Different detunings in microgravity are

then presented in Section 4.7. Section 4.8 will compare gravity and microgravity results. Finally, Section 4.10 will conclude with the lifetime measurements in shell potentials under gravity.

4.1 Physical Background

This section will introduce the necessary physical concepts for understanding dressed state potentials. Initially starting with the Landau-Zener model [76], which is used to illustrate dressed states and to calculate expected losses due to flips from dressed states to bare states.

Landau-Zener model An uncoupled two state system can be described by a Hamiltonian represented by a diagonal matrix, where the diagonal elements are the eigenenergies of the system

$$H = \begin{bmatrix} \alpha(t) & 0 \\ 0 & -\alpha(t) \end{bmatrix}. \quad (4.1)$$

Without any coupling between the two states the eigenenergies would cross at a certain time t . By introducing a coupling between the two states, for example a microwave field between the two rubidium clock states, one introduces a non-diagonal element

$$H = \begin{bmatrix} \alpha(t) & \beta(t) \\ \beta(t) & -\alpha(t) \end{bmatrix}. \quad (4.2)$$

Diagonalizing the above matrix leads to new eigenenergies

$$\mathcal{E}(t) = \pm \sqrt{\alpha^2(t) + \beta^2(t)}. \quad (4.3)$$

Figure 4.1 illustrates this behavior for the Landau-Zener model, where $\alpha(t) = \lambda t$. An avoided-crossing at $t = 0$ for a constant coupling can be seen.

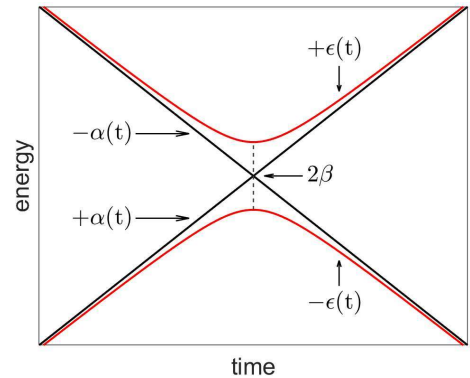


Fig. 4.1: Illustration of the Landau-Zener model.

Zeeman splitting The aforementioned coupling can be between different hyperfine states, where a microwave field needs to be used, or between magnetic sub-states of a hyperfine state. In that case it is sufficient to use a radio frequency field. The degeneracy of this magnetic sub-states, also referred to as Zeeman levels, can be canceled by applying a magnetic field. A magnetic field \vec{B} interacts with the magnetic moment of the nucleus and the (outer-)electron of an alkali atom such as rubidium. The Hamiltonian of this interaction

$$H = \vec{\mu}_F \cdot \vec{B} = g_f \mu_b \vec{F} \cdot \vec{B} \quad (4.4)$$

depends on the total angular momentum \vec{F} and the magnetic field \vec{B} in case of small magnetic fields (10^{-4} - 10^{-2} T in case of rubidium). This equation also depends on the Landé factor g_f and the Bohr magneton μ_b . By choosing the magnetic field direction along the z-axis $\vec{B} = B_0\vec{e}_z$ one gets the eigenenergies of the Hamiltonian

$$E = m_f g_f \mu_b \hbar B_0, \quad (4.5)$$

where m_f is the magnetic quantum number. The momentum eigenstate of the total angular momentum operator was used in this case: $F_z |F, m_f\rangle = m_f \hbar |F, m_f\rangle$, where $m_f = -F, \dots, +F$. The difference between these energy levels is in the range of RF frequencies (typically in the order of 1 MHz for rubidium).

Magnetic trap Before coupling different magnetic sub-states with a RF field and creating new states it is useful to trap the atoms beforehand in a magnetic trap. An atom in an inhomogeneous magnetic field is described by the following Hamiltonian

$$H = \frac{\vec{p}^2}{2m} + m_f g_f \mu_b \hbar |\vec{B}(t)|, \quad (4.6)$$

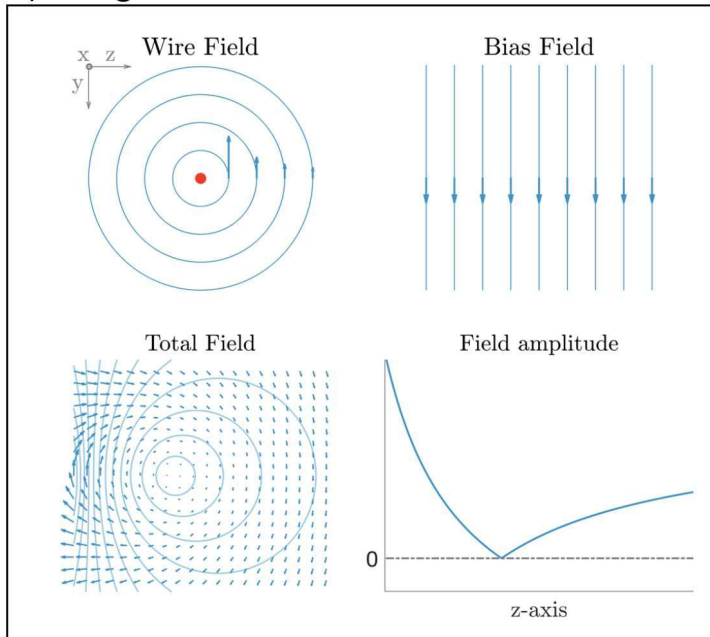
where \vec{p} is the momentum of the atom and m its mass. Here it was assumed that the change in the magnetic field due to the motion of the atom is less than the Larmor frequency $\omega_{Larmor} = g_f \mu_b \hbar |\vec{B}(t)| / \hbar$:

$$\frac{d/dt \vec{B}}{|\vec{B}|} < \omega_{Larmor}. \quad (4.7)$$

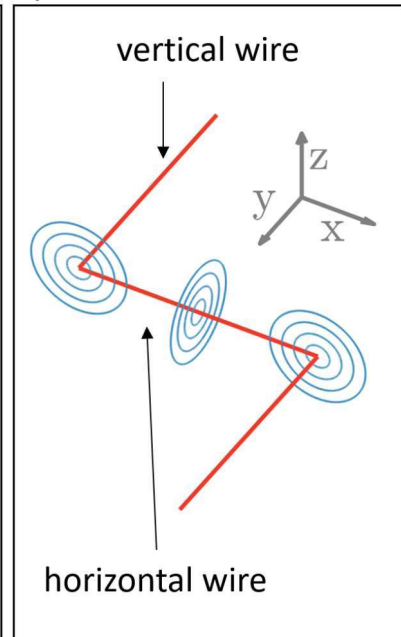
In that case, the eigenvalues $\hbar m_f$ can be treated as spatially independent, albeit a change in the direction of the quantization axis. From Equation 4.6 it follows that atoms with $m_f g_f > 0$ are drawn towards lower magnetic field amplitudes (low-field seeker) and atoms with $m_f g_f < 0$ towards higher magnetic fields (high-field seeker). The Earnshaw theorem [77] shows that there are no solutions of Maxwell's equations in free space with a local maximum. Hence, only atoms in the low-field seeking state can be magnetically trapped. Figure 4.2 illustrates how a local magnetic field minimum can be created with a Z-shaped wire of an atom chip and a bias field. The horizontal part of the wire combined with an bias field creates a magnetic field minimum, while the vertical wires lift the minimum value above zero. That configuration is of an Ioffe-Pritchard type magnetic trap [78] and has no zero-crossing and does not violate Equation 4.7 at its minimum.

Dressed state potential It is possible to create a dressed state potential by starting at a static magnetic trap as described in the previous paragraph and then couple the different Zeeman levels with a RF field. Furthermore, it is enough to consider only the oscillating magnetic field of the RF field, because transitions between the different Zeeman states are

a) Straight wire + bias field



b) Z-wire



c) Z-wire + bias field

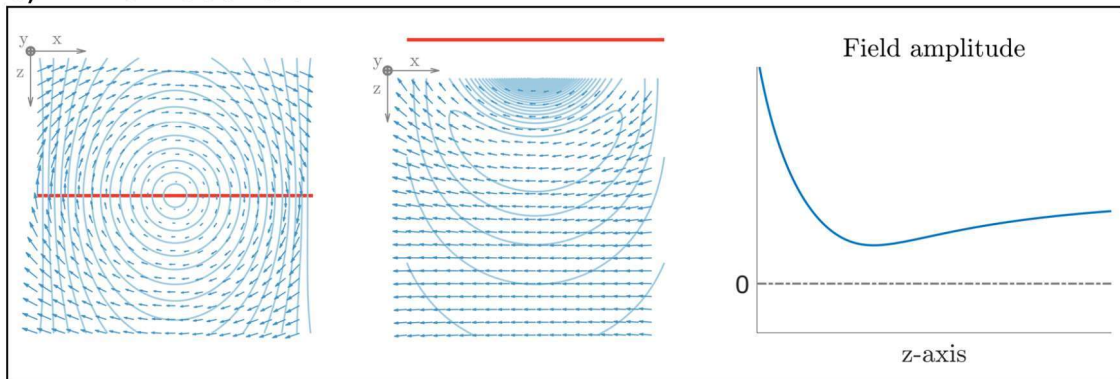


Figure 4.2: Illustration of an Ioffe-Pritchard magnetic trap created with a Z-wire and a bias field. The top left corner shows the magnetic potential created by an infinite long straight wire and a bias field. The resulting magnetic potential has an amplitude of 0 at its minimum. The top right corner shows the magnetic field of a Z-wire. By bending the wire in opposite directions one creates magnetic fields, which cancel at the center of the straight wire. The lower three images show on the left the magnetic field of the vertical wires, the total magnetic field with isopotential lines in the center, and a cut along the z-axis of the center image. The resulting potential has a non-zero potential minimum.

magnetic dipole transitions. The Hamiltonian describing the state of the atom is

$$H = g_f \mu_b \vec{F} \cdot \vec{B}_0(\vec{r}) + g_f \mu_b \vec{F} \cdot \vec{B}_1(\vec{r}, t), \quad (4.8)$$

where \vec{B}_0 is the static magnetic field and \vec{B}_1 the oscillating magnetic field of the RF field. The detailed solution to this Hamiltonian can be found in Reference [79]. The resulting potential is of the form:

$$V(\vec{r}) = \tilde{m} \hbar \sqrt{\delta^2(\vec{r}) + |\Omega_1(\vec{r})|^2}, \quad (4.9)$$

where \tilde{m} are the quantum number of the new dressed states. Typically, one would use the maximally polarized state $\tilde{m} = F$ to trap atoms. Details of the equation are discussed below.

- Detuning $\delta(\vec{r}) = \omega_{Larmor}(\vec{r}) - \omega_{RF}$. The Larmor frequency is spatially dependent due to the magnetic trap. On the other hand, the RF frequency is constant. This leads to a surface around the magnetic trap minimum, where $\delta = 0$. This surface is called the isomagnetic surface.
- Rabi frequency or coupling $\Omega_1(\vec{r}) = \frac{|g_f| \mu_b |B_\perp(\vec{r})|}{2\hbar}$, where $B_\perp(\vec{r})$ is the projection of the RF B-field on the static B-field.
- Equation 4.9 was calculated using the rotating wave approximation (RWA). Thus, the terms rotating with $2\omega_{RF}$ were omitted. This only holds for a detuning δ smaller than the RF frequency ω_{RF} .
- Non-RWA calculations lead to a shifted potential minimum [80].
- The dressed state system processes around a new quantization axis, which is tilted by an angle $\theta = \arccos(-\delta/\Omega_1) + (s-1)\pi/2$ to the quantization axis of the static magnetic field. The new spin states can be deduced from the initial spin states by a rotation operator $|\tilde{m}\rangle = e^{i\theta F_y/\hbar} |m_z\rangle$. Hence, the eigenvalues of the two spin states are identical [79]: $F_z |m_z\rangle = F_\theta |\tilde{m}\rangle = m\hbar |m\rangle$.

In short, the RF frequency ω_{RF} determines minimum of the dressed potential and the Rabi frequency Ω_1 the curvature around the minimum of the potential.

Adiabatic condition When transferring the atoms from the bare states to the dressed states or later changing the shape of the dressed state potential one needs to change the detuning and the Rabi frequency. Similar to the condition for the magnetic trap (see Equation 4.7) the rate of change of the quantization axis needs to be considered. The change of the θ angle between the new quantization axis and the quantization axis of the static magnetic field needs to fulfill [79]

$$|\dot{\theta}| \ll \Omega. \quad (4.10)$$

This condition, which states, that the change of angle of the new quantization axis and the quantization axis of the static magnetic field needs to be smaller than the effective

Rabi frequency $\Omega = \sqrt{\delta^2 + \Omega_1^2}$ is similar the condition for the magnetic trap (Equation 4.7), which states that the rate of change of the quantization axis direction needs to be smaller than the Larmor frequency. This can be interpreted as the precession around the quantization axis needs to be faster than the change of the quantization axis. Equation 4.10 can be expressed in terms of the detuning δ and the Rabi frequency Ω_1 :

$$\frac{\dot{\delta}\Omega_1 - \delta\dot{\Omega}_1}{\delta^2 + \Omega_1^2} \ll \sqrt{\delta^2 + \Omega_1^2}. \quad (4.11)$$

Leading to the criterion for adiabaticity:

$$|\dot{\delta}\Omega_1 - \delta\dot{\Omega}_1| \ll (\delta^2 + \Omega_1^2)^{3/2}. \quad (4.12)$$

Landau-Zener losses A major source of atom losses in a dressed state potential are Landau-Zener losses. The Landau-Zener model was briefly introduced in the first paragraph and losses occur at the minimum of the avoided-crossing region. This model is used to estimate non-adiabatic losses from RF dressed state potentials [81, 82]. Burrows *et. al.* [83] calculated the decay rate for the Landau-Zener model for a simplified RF dressed state trap. The underlying magnetic field gradient was linearized, the trap axis were chosen such that gravity does not contribute to the losses, and a trap with sufficiently strong coupling to be adiabatic was assumed. This results in a decay rate for an ensemble of atoms of mass M and in the hyperfine state F :

$$\Gamma \approx \frac{2\omega_z F}{\pi} \exp\left(-\frac{\pi\Omega_1^2}{2\alpha} \sqrt{\frac{M}{2E}}\right). \quad (4.13)$$

This equation states the decay rate in a RF dressed potential through non-adiabatic losses by incorporating the probability of remaining in the dressed states while passing the crossing point and the number of passes per unit time. The following factors are contributing to the losses:

- Oscillation frequency in RF dressed state trap ω_z : This frequency is determined by the curvature around the minimum of a shell potential. For a given detuning a higher Rabi frequency results in a smaller oscillation frequency.
- Rabi frequency Ω_1 : A higher Rabi frequency leads to smaller Landau-Zener losses.
- The curvature of the gradient underlying magnetic field α : Higher gradients lead to higher losses.
- The total energy E of the ensemble: Colder ensembles lead to smaller losses.

Atom density in the shell potential To be able to compare the simulation results to measurements it is possible to project the position of the isomagnetic surface on the primary and secondary detection system. This provides information on the position and shape of the shell potential. However, to get information on the atom density in the shell potential one needs to calculate the occupation of the shell potential with atoms for a given

temperature. Helmerson *et. al.* [84] performed the calculation for a magnetic trap with a 50 mK thermal ensemble. Starting with a general expression for the atom density in the trap

$$n(\vec{r}) = \frac{N}{Z} \int d^3p P(E), \quad (4.14)$$

where N is the total number of atoms, $P(E)$ the energy distribution of the trapped atoms with an energy of $E(\vec{r}, \vec{p}) = U(\vec{r}) + p^2/2m$. Here, $U(\vec{r})$ is the potential energy of the atoms and p and m their momentum and mass, respectively. The partition function Z is given by the following function

$$Z = \int d^3r \int d^3p P(E). \quad (4.15)$$

It is assumed that the energy distribution is given by the Boltzmann distribution. The integration is performed over all trapped atoms. In contrast to Helmerson *et. al.* the energy distribution is not truncated, because in our case the temperatures are much lower in the range of low μK or nK . Moreover, by just comparing the qualitative shape of the measured absorption image with the simulated absorption image one can set the constant prefactor for a given temperature to 1. The resulting atom density is given by the following simple expression

$$n(\vec{r}) = \exp\left(-\frac{U(\vec{r})}{k_B T}\right). \quad (4.16)$$

4.2 Hardware Setup

The same hardware setup as for evaporative cooling was used (see Section 2.5). The National Instruments *PXI 5421* arbitrary waveform generator (AWG) was already integrated in the PXI system and implemented in the control software. The RF frequency is generated by means of direct digital synthesis (DDS) and could reach up to 43 MHz. The peak-to-peak voltage is specified to 12 V at a 50 Ω load. The global gain of the amplifier, later referred just as gain, could be adjusted with a numerical value between 0 and 5. During the sequence the relative RF amplitude could be adjusted in each sequence step with numerical values between 0 and 1. The output power as a function of these numerical values will be shown in Section 4.4. For evaporative cooling and for the adiabatic rapid passage (ARP) the gain was kept at 3.5. The AWG is connected to the lower U-wire on the *Base Chip* (see Figure 4.3). The current flowing through the U-wire is strongly dependent on the impedance of cables, connectors, vacuum feed-through, and on the U-wire itself. The impedance of the whole RF chain as a function of the frequency is presented in Section 4.4. The antenna was not modified to match the 50 Ω impedance of the AWG, because the same setup was used for evaporative cooling and its modification would have tempered with the evaporation efficiency.

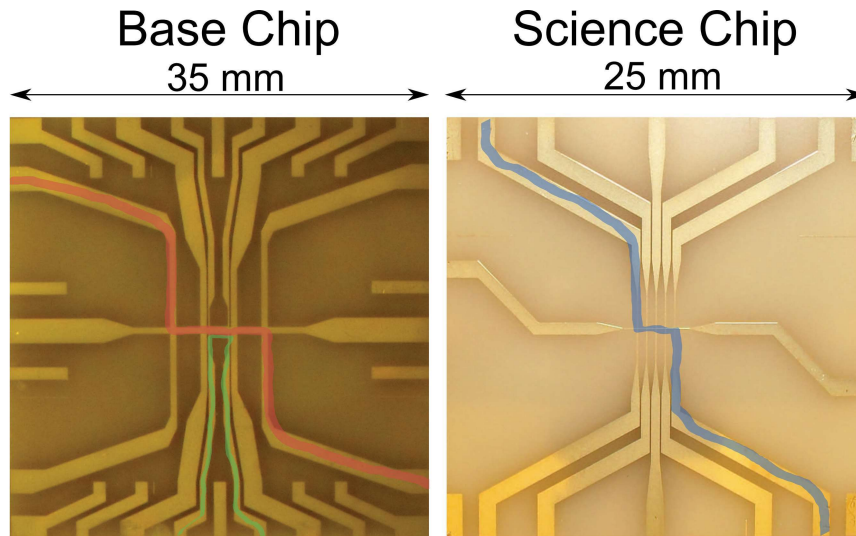


Figure 4.3: *Base* and *Science* Chip structures used for shell potentials. The Z structure of the *Base* Chip, indicated with red, contributes to the static Ioffe-Pritchard magnetic trap and the lower U-wire, indicated by green, creates the RF field. The U-wire part parallel to the horizontal part of the Z-wire is $20 \mu\text{m}$ wide and there is a $40 \mu\text{m}$ wide gap between the U-wire and the $500 \mu\text{m}$ Z-wire. The Science Chip is placed centered on the *Base* Chip. The Z-wire used as well for the Ioffe-Pritchard magnetic trap is indicated by the blue color. The distance between the structures on the *Base* Chip and the surface of the *Science* Chip is 1.02 mm . The $z = 0$ position is located on the surface of the *Science* Chip.

4.3 Simulation

The properties of the dressed state potential depend on the underlying static magnetic trap and the RF source. That allows for many possible combinations. The aim of this section is to find combinations, which are favorable for a shell potentials. Hence, the shape of the potential should be as *spherical* as possible, the potential values on the surface of the sphere should be as *homogeneous* as possible, and the *size* of the shell potential and the *thickness* of shell should be adjustable. In Section 4.1 it was found that the dressed state potential can be described by Equation 4.9 for a detuning $\delta = \omega_{RF} - \omega_{Larmor}$ smaller than the RF frequency ω_{RF} by

$$V(\vec{r}) = m\hbar\sqrt{\delta^2(\vec{r}) + \Omega_1(\vec{r})^2},$$

where m will be chosen to be equal to the highest polarization state $m = F = 2$, $\omega_{Larmor} = g_f\mu_b|\vec{B}_0(r)|$ depends on the static magnetic field B_0 , and the Rabi frequency $\Omega_1(\vec{r}) = g_f\mu_b B_\perp(\vec{r})/2\hbar$ depends on the projection of the RF magnetic field on the static magnetic field ($B_\perp = |\vec{B}_0 \times \vec{B}_{RF}|$). The static and RF magnetic fields are created with an atom chip and in case of the static field additional bias coils. That does not allow for a concise analytical expression for the magnetic fields and hence, a concise analytical expression for the dressed state potential. In contrast, Colombe *et. al.* [72] could utilize analytical expressions for their potential based on a QUIC magnetic trap [85] due to the simple

geometry of the trap consisting of only three coils. Additionally, that trap configuration allowed to align the trap axis with the gravity vector simplifying the discussion. Hofferberth *et. al.* [73] used a general expression for an Ioffe-Pritchard magnetic trap [78] to qualitatively discuss the geometry of their dressed state potential with the aim of realizing a double-well potential. Their setup was based as well an atom chip, making concise analytical expressions infeasible. In contrast to our setup, they used two U-wires to create the RF magnetic field allowing for a rotation of the RF magnetic field direction. Hence, allowing for circular polarization of the field. In our setup only one U-wire is used (see Figure 4.3) allowing only for linear RF field polarization. The qualitative discussion of the equation for the potential simplifies thus for only two cases. For a detuning δ below and above zero. When the detuning is above zero the minimum of the potential is located at the positions, where $\omega_{Larmor} = \omega_{RF}$ for a low enough Rabi frequency Ω_1 . This minimum determines a surface, called isomagnetic-surface, in case of conservative magnetic potentials, such as quadrupole or Ioffe-Pritchard type magnetic traps. Hence, creating a shell potential. The Rabi frequency adjusts the curvature around the minimum, thus, determining the thickness of the shell. To sum up: the detuning δ adjusts the *size* of the shell potential and the Rabi frequency Ω_1 adjusts the *thickness* of the shell. In case of the detuning below zero the geometry is determined by the Rabi frequency. The detuning only shifts the potential lower, while a big enough Rabi frequency increases the potential at minimum of the magnetic trap due to avoided crossing.

A simulation of the magnetic fields created by the atom chip and the bias coils was developed in the group of Reinhold Walser at the TU Darmstadt [43]. It uses the law of Biot-Savart to calculate the 3D magnetic fields for a given current.

Initially, it was investigated what magnetic field configuration is the most *spherical*. This can be quantified by the trapping frequencies ν_i ($i = x, y, z$), where in a perfectly spherical configuration all three trapping frequencies would be equal. From all possible magnetic field configurations the search was restricted to magnetic field of an Ioffe-Pritchard type with a Z-wire current of 2 A in the *Science Chip* and 6 A in the *Base Chip* Z-wire (see Figure 4.3). This configuration was chosen, because measurements in this configuration in microgravity conditions already exist and the excitations in the BEC are known [25, 34]. Due to the Ioffe-Pritchard type configuration it was expected that a perfectly spherical configuration can not be achieved. In this configuration two trapping frequencies are approximately equal and the third trapping frequency is significantly smaller. The spherical property of this configuration is quantified by the ratio of weak trapping axis to the two strong trapping axis: $2\nu_x/(\nu_y + \nu_z)$.

The x-bias-coils current was fixed to 0.1 A and the current through the y-bias-coils was varied between -1.5 A to -0.2 A to investigate properties such as the frequency offset at the potential bottom, the z position of the potential minimum, the rotation angle of the trap eigenaxes with respect to the atom chip coordinate system in the x-y plane, and the aforementioned ratio of the weak trapping frequency and the strong trapping frequencies for a potential without gravity. The limits of -1.5 A and -0.2 A were chosen, because at a y-bias-coils current of -1.5 A is the final magnetic trap position of the evaporation ramp and at -0.2 A the trap minimum is almost at the edge of the absorption detection system. The results are shown in Figure 4.4.

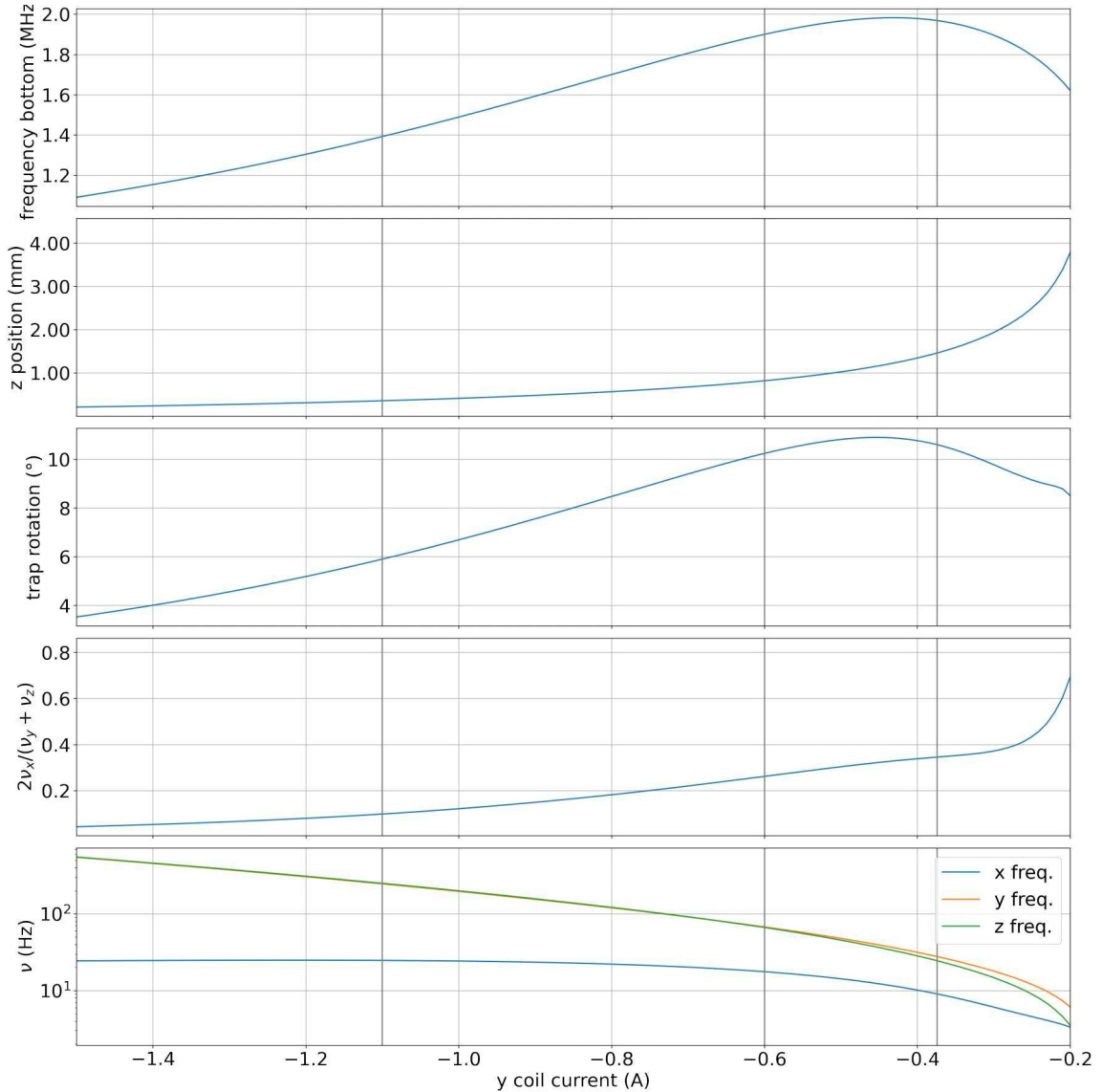


Figure 4.4: Magnetic trap configurations with different y -bias-coils currents. A simulation of an Ioffe-Pritchard type trap was created with the following parameters: *Base Chip Z* current = 6.0 A, *Science Chip Z* current = 2.0 A, x -bias-coils current = 0.1 A, z -bias-coils current = 0.0 A, and the y -bias-coils current was varied from -1.5 A to -0.2 A in 0.01 A steps. The potential was calculated without gravity. The frequency offset at the potential bottom, the z position of the trap minimum, the rotation angle of the trap eigenaxes with respect to the atom chip coordinate system in the x - y plane, the ratio of the weak trapping frequency to the strong trapping frequencies, and the three individual trapping frequencies are shown. The three vertical lines at y -bias-coils currents of -1.1 A, -0.6 A, and -0.374 A show the magnetic trap configuration used latter as a static magnetic field for shell potentials. The reason for the choice and the detailed discussion of the above curves is in the text.

It can be observed that the z-position increases monotonously with decreasing y-bias-coils current. Around a current of -0.4 A the increase of the z position accelerates significantly. The frequency offset at the potential bottom and the rotation angle of the trap increase up to a value of -0.5 A and decrease afterwards. The ratio of the weak trapping frequency to the strong frequency increases rapidly at a y-bias-coils current of -0.3 A and has a value of 0.7 at a current of -0.2 A. Nevertheless, this value is not representative of the approximation of a sphere, because the overall trapping frequency ratio changes. While at higher y-bias-coils currents the trap has a prolate form (two strong trapping frequencies and one weak trapping frequency) at lower y-bias-coils currents the shape is oblate (two weak trapping frequencies and one strong trapping frequency). For example, at a y-bias-coils current of -0.2 A the weak trapping axis (x-axis) has the same trapping frequency (3.5 Hz) as the former strong trapping frequency in z-direction, while the y-direction trapping frequency has a value of 6 Hz. Hence, the maximum ratio of the weak trapping frequency to the strong trapping frequencies can not exceed 0.4 by just decreasing the y-bias-coils current. For that reason, the lowest y-bias-coils current was set to -0.374 A. This position was already used in the magnetic lens measurements and a transport ramp from the evaporation position (y-bias-coils current of -1.5 A) was calculated with the method of shortcut-to-adiabaticity [42] to reduce the excitations in the Bose-Einstein condensate during transport. Choosing a position further away from the atom chip would require new calculations and would not improve the spherical shape of the shell potential significantly. The magnetic trap at that position cannot trap atoms under gravity and can only be realized in microgravity. To do measurements under gravity two other positions were chosen with y-bias-coil currents -0.6 A and -1.1 A. These positions can trap atoms under gravity, are approximately 0.5 mm apart, have significantly different ratios of the weak and strong trapping frequencies, and measurements at these positions were already performed prior to shell potential measurements. The x-bias-coils current for these two positions was set to remain at 0.5 A. This is the chosen current during the evaporation and changing this current to 0.1 A would change the stronger trapping frequencies from approximately 450 Hz to 550 Hz and 60 Hz to 65 Hz for positions with a y-bias-coils current of -1.1 A and -0.6 A, respectively. The weak trapping frequency stays approximately the same. This change of the trapping frequency excites oscillations and should be omitted, if possible. Nevertheless, due to comparability with former measurements [34, 40], where the x-bias-coils current was set to 0.1 A for a y-bias-coils current of -0.374 A to reduce the rotation in the x-z plane from 14.0° to 10.6° , the current was set here as well to 0.1 A. The simulated magnetic field configurations are summed up in Table 4.1. To the potentials with a y-bias-coils current of -1.1 A, -0.6 A, and -0.374 A will be from now on referred to as position *a*2, *b*, and *c*, respectively.

After identifying three different static magnetic traps. The shell potential based on these magnetic traps were calculated. For the RF magnetic field a current of 0.1 A through the lower U-wire was set. This value was chosen close to the typically experimental AC current values, but can be easily adjusted by multiplying the resulting magnetic field vector by a factor $f = \frac{I_{new}}{0.1A}$. This is not possible with the static magnetic field configuration, because it consists of the magnetic fields of 5 different structures. For the three configurations from Table 4.1 the static and RF magnetic field was simulated on a grid with a $2 \times 2 \times 2 \mu m^3$

Table 4.1: Properties of different positions dubbed position *a2*, *b*, and *c*. The currents through the Z-structures of the *base chip* and *science chip* for all positions were 6 A and 2 A, respectively. The z-bias-coils current was 0 A for all positions. The z-position of the minimum of the magnetic trap, the ratio of the trapping frequencies ($2\nu_x/(\nu_y + \nu_z)$), and the value of the potential bottom were calculated with the atom chip simulation from the group of Reinhold Walser [43].

Name	I_x (A)	I_y (A)	z (μm)	$2\nu_x/(\nu_y + \nu_z)$	f_{bottom} (MHz)
a2	0.5	-1.1	354	0.11	1.894
b	0.5	-0.6	813	0.29	2.452
c	0.1	-0.374	1462	0.34	1.969

resolution. The detunings were set to 406 kHz, 48 kHz, and 31 kHz for positions *a2*, *b*, and *c*, respectively. These values lead to an approximately equal size in the x-direction of 1 mm. The currents through the lower U-wire were set to 28.6 mA, 11.0 mA, and 7.5 mA. These values were experimentally determined to be the lowest possible currents to still transfer atoms into the shell potentials. The detuning and the Rabi frequency was calculated independently by

$$\begin{aligned} \delta &= \omega_{Larmor}(\vec{r}) - \omega_{RF} \\ \Omega_1 &= \frac{|g_F| \mu_B |B_{\perp}(\vec{r})|}{2\hbar} \end{aligned} \quad (4.17)$$

Using matlab's *isosurface*, *patch*, and *isonormals* functions the surface, where $\delta = 0$ Hz was plotted (see Figure 4.5). This surface is the potential minimum of the shell potential in the rotating wave approximation. The Rabi frequency Ω_1 was projected on the surface with the *isocolors* functions. This procedure allows to observe the shape of the potential in 3D and to view the Rabi frequency on the surface. Ideally, the Rabi frequencies would be equal everywhere on the surface to achieve equal potential values around the minimum. This is not possible in our setup due the location of the RF antenna on the atom chip. This leads to an asymmetric Rabi frequency distribution on the potential surface due to the side of the shell potential closer to the atom chip having a higher RF B-field value.

As expected, the higher ratio of the weak trapping frequency to the strong strapping frequency at a position further away from the atom chip lead to a more *spherical* shell geometry. Furthermore, the distribution of the Rabi frequency on the isosurface is getting more symmetrical further away from the atom chip. At position *a2* the highest coupling is at the positive x-direction and decreases in direction of increasing z and decreasing x. Additionally, two bands of higher coupling are observed at positive and negative y-direction. At position *b* the coupling is more symmetrically distributed on the isosurface, albeit being stronger on the positive x-direction and lower z-direction values. Further away from the atom chip at position *c* the x-direction Rabi frequency asymmetry has mainly vanished, only a Rabi frequency asymmetry between smaller and higher z-direction values is observed. Nevertheless, the difference is lower. At position *c* the difference is 0.4 kHz, at the position *b* the difference is 0.95 kHz, and at position *a2* 4.7 kHz. Hence, the shell potential at

position *c* is the most *spherical* and *homogeneous* of the three investigated potentials.

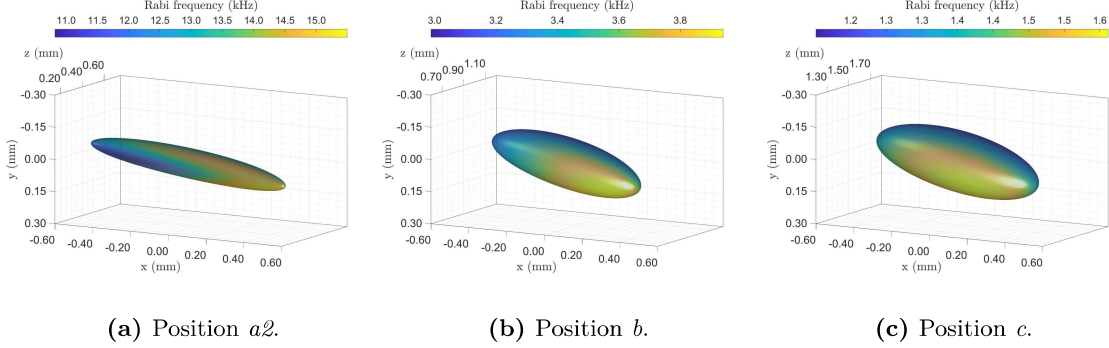


Figure 4.5: Simulation of the shell potentials at positions *a2*, *b*, and *c*. The trap parameters of the static magnetic traps at those positions are listed in Table 4.1. The RF frequency was chosen to be 2.3 MHz, 2.5 MHz, and 2.0 MHz for the positions *a2*, *b*, and *c*, respectively. This value lead to a detuning of 406 kHz, 48 kHz, and 31 kHz for the positions *a2*, *b*, and *c*, respectively. The x- and y-axis dimensions were fixed to -0.6 mm to 0.6 mm in the x-direction and -0.3 mm to 0.3 mm in the y-direction for all 3 plots. The length of the z-axis was chosen to be 0.6 mm and centered at the minimum of the magnetic trap. The RF frequencies were chosen such that the extension in the x-direction was approximately the same. The RF power was chosen to be the minimal necessary RF power to transfer the atoms to dressed states. The RF power for position *a2* corresponded to an AC current of 28.6 mA, for position *b* the RF power corresponded to an AC current of 11.0 mA, and for position *c* the RF power corresponded to an AC current of 7.5 mA.

The detuning and the Rabi frequency from Equation 4.17 were combined to calculate the full potential: $2\hbar\sqrt{\delta^2 + \Omega_1^2}$. Slices were calculated in the x-y plane, x-z plane, and the y-z plane. The location of the x-y plane was set to $z = 0.354$ mm, 0.813 mm, and 1.462 mm for positions *a2*, *b*, and *c*, respectively. For the x-z and y-z plane the other coordinate was set to 0 mm. The calculation was performed with an increased resolution of $1.0 \mu\text{m}$. Additionally, the potential along the z-direction for $(x, y) = (0, 0)$ mm was calculated with a resolution of $0.5 \mu\text{m}$ ($0.125 \mu\text{m}$ in case of position *a2*). Figures 4.6, 4.7, and 4.8 show the plots for position *a2*, *b*, and *c*, respectively. In addition to the observations from the isomagnetic-surface plots the following remarks can be added

- **Potential difference along z-direction:** The potential was calculated at $(x, y) = (0, 0)$ mm. The Rabi frequency at position *a2* is not symmetrical along the z-direction. Hence, the potential along the z-direction does not show the highest and lowest potential value. This leads to a smaller potential difference at position *a2* than at *b* (0.755 kHz and 1.506 kHz, respectively).
- **Flattened shape at the atom chip facing side:** The plots of the x-z planes in Figures 4.6, 4.7, and 4.8 show less curvature in the x-direction at the atom chip facing side of the potential. This curvature decreases with decreasing distance to the atom chip. This is due to the influence of the vertical wire-parts of the Z-wire. For future measurements with Bose-Einstein condensates and observations of vortices on the shell surface position *c* could be beneficial, because the curvature exerts a force

on these vortices [30].

- **Rotated shape in the x-y plane:** The rotation of the eigenaxes of the magnetic trap with respect the axes of the atom chip coordinate system in the x-y plane are reflected in the rotated shape of the shell potential. This rotation is not an issue in microgravity, but under gravity this rotation is significant, because the shift of the potential values due to gravity depends on the y-position. Hence, the rotation introduces a potential shift.

In the discussion so far it was concluded that position *c* is beneficial in regard to how *spherical* and *homogeneous* the potential is. Additionally, it is trivial to conclude that shell potentials based magnetic traps with lower trapping frequencies result in a greater *size* of the shell potential for the same detuning, because the curvature of the magnetic field around the magnetic trap minimum is smaller. Figures 4.6, 4.7, and 4.8 verify this reasoning.

At last, the *thickness* property needs to be investigated. The potential around the minimum of position *a2* and *c* along the z-direction for $(x, y) = (0, 0)$ mm was calculated for the maximal possible RF power and the lowest possible RF power, where atoms are still transferred to the dressed states (this was determined in Section 4.6). For the detunings the same values as in the previous calculations were chosen (406 kHz and 31 kHz). For position *a2* the minimal and maximal AC currents are 28.6 mA and 78.8 mA, respectively. For position *c* this values are: 7.5 mA and 82.0 mA. Figure 4.9 shows the resulting potential values. The y-axis range was set to 20 kHz and the minimal y-axis value to the minimum of the potential. The x-axis range for position *a2* is 4 μm and for position *c* 40 μm . From the x-axis range it is already obvious that the *thickness* of the shell potential - which for example can be defined as the distance from the potential minimum, where the thermal atom density falls below $1/e$ - is at position *a2* is much smaller than at position *c*. Assuming an ensemble temperature of 100 nK and using Equation 4.16 one can calculate the $1/e$ - distance for the four above potentials: for position *a2* 1.6 μm in the low power case and 2.3 μm in the high power case. In case of position *c* these values are 32 μm and 53 μm .

4.3.1 Effects of Gravity

To include the effect of gravity one need to modify Equation 4.9 by the gravitational potential term:

$$V(\vec{r}) = m\hbar\sqrt{\delta^2(\vec{r}) + |\Omega_1(\vec{r})|^2} - m_{Rb}\vec{g} \cdot \vec{r}, \quad (4.18)$$

where m_{Rb} is the mass of the rubidium 87 atom and \vec{g} the gravitational acceleration vector. The gravitational acceleration causes a relative potential shift of 2136 kHz/mm. Figures 4.10 and 4.11 show the calculated potentials under gravity and in microgravity at position *a2* and *b*. Position *c* is not possible under gravity and thus was not considered. The potential at position *a2* is only slightly deformed: the overall shell shape was preserved, but the potential values are lower the bottom of the shell potential. On the other hand, the potential at position *b* is changed significantly: the shell shape has deformed into a half-shell and at the lower part is an elongated deformation in the positive x-y direction

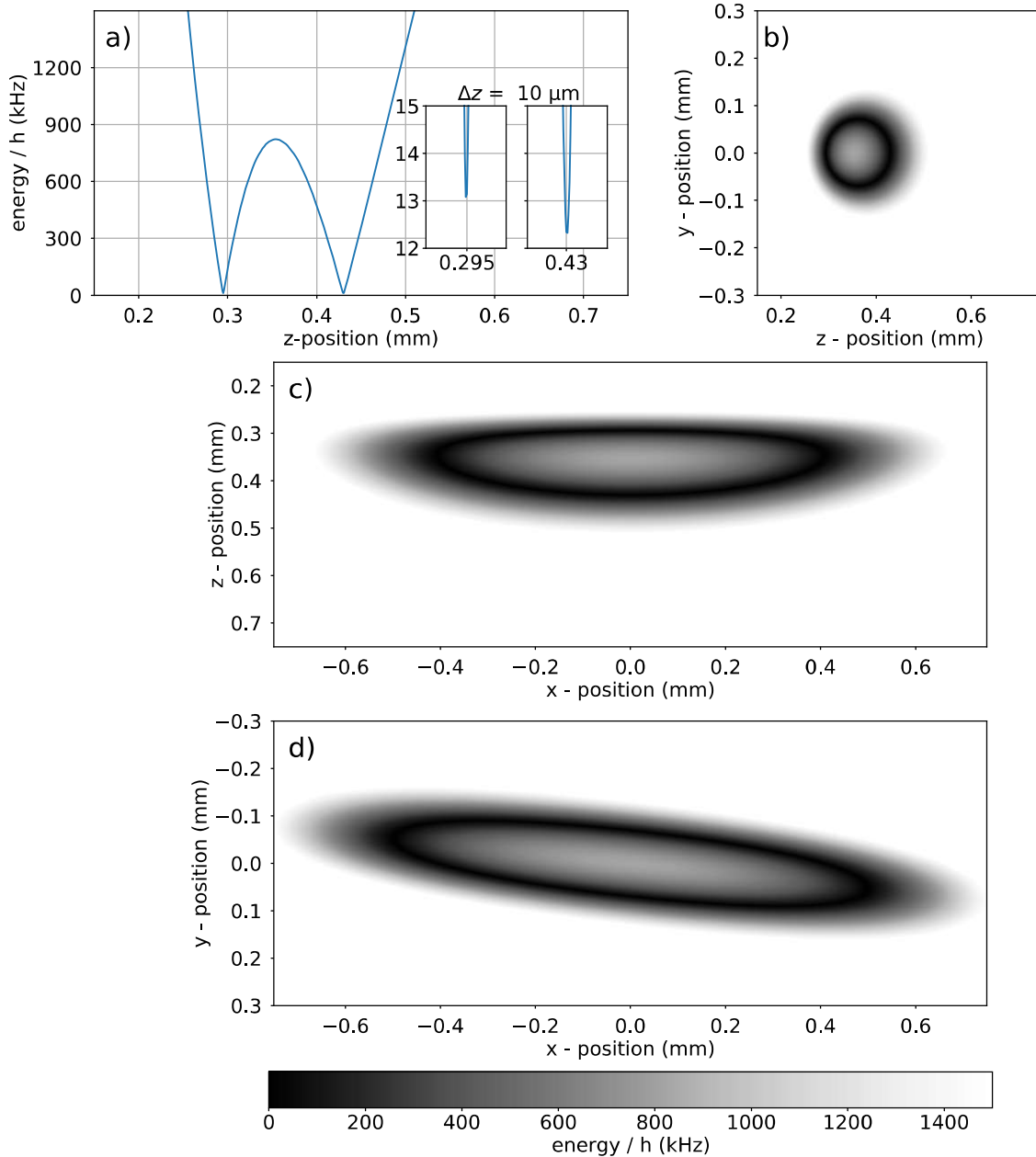


Figure 4.6: Slices through the shell potential at position $a2$. The potential was calculated for a detuning of 406 kHz and a RF power corresponding to an AC current of 28.6 mA. Image **a**) shows the potential along the z -direction for $(x, y) = (0, 0) \mu\text{m}$. The potential minimum at greater z -distance is lower than the potential minimum at smaller z -distance. This is due to location of the RF antenna at the atom chip and the decreasing magnetic field amplitude along the z -direction. The potential difference is 755 Hz. Furthermore, the potential minimum at greater z -direction distance is wider than the potential minimum closer to the atom chip. This shape stems from the static magnetic field, which was created by a Z -structure on the atom chip and has a steeper curvature closer to the atom chip (see Figure 4.2). Images **b**) and **c**) show slices through the x - z and x - y plane. In the first image the plane was located at $y = 0 \mu\text{m}$ and in the latter image at $z = 354 \mu\text{m}$ (the minimum of static magnetic trap). In Image **b**) the cigar-shape of the potential is very well visible. This is due to Ioffe-Pritchard type configuration of the static magnetic trap. The elongated form reflects the ratio of 0.11 between the weak trapping axis and the strong trapping axes. Additionally, image **c**) shows the tilt of the potential due to the Z -structure. The potential is tilted in the direction following the vertical wires of the Z -structure (see Figure 4.2).

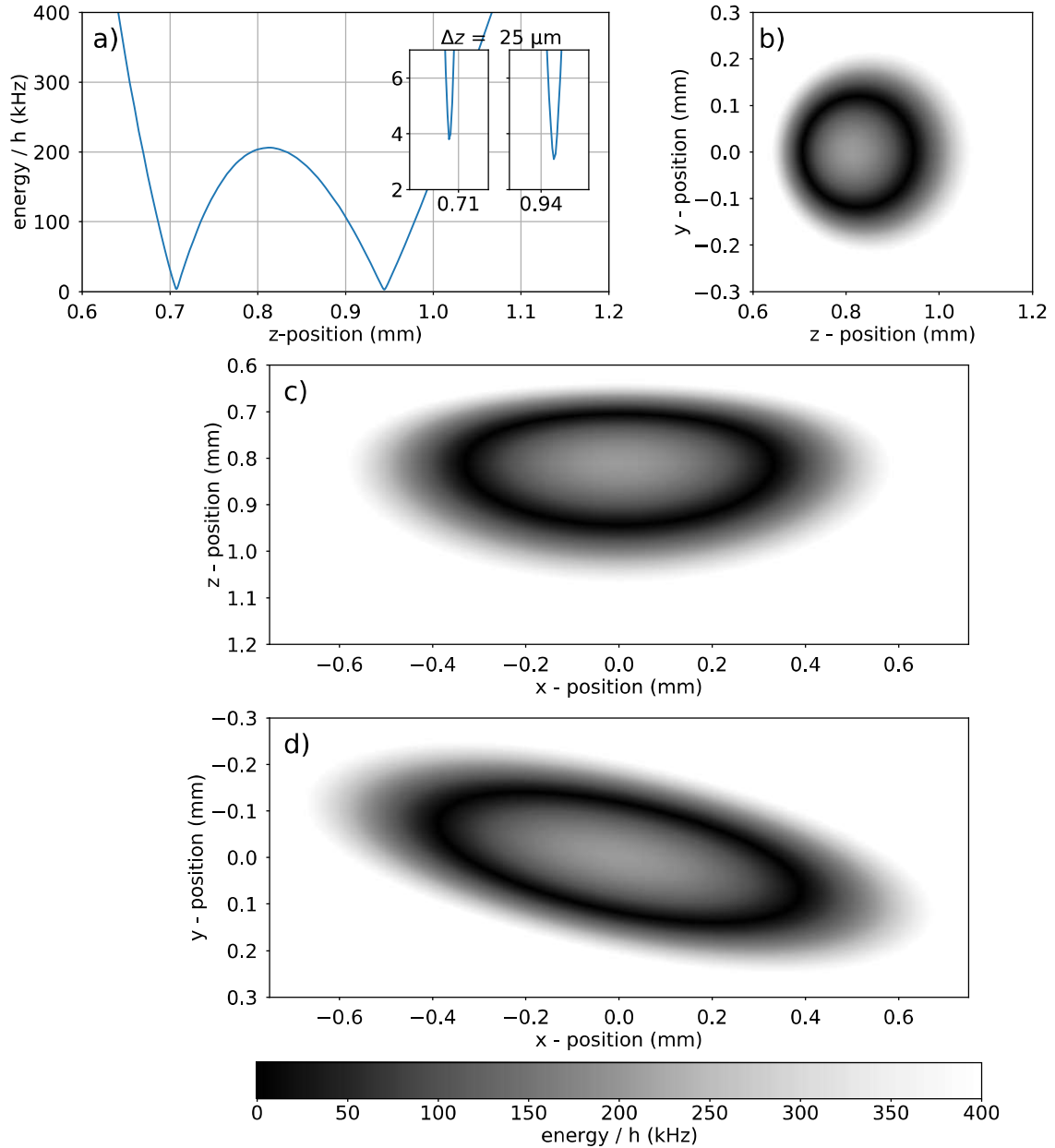


Figure 4.7: Slices through the shell potential at position *b*. The potential was calculated for a detuning of 48 kHz and a RF power corresponding to an AC current of 11.0 mA. Image **a**) shows the potential along the *z*-direction for $(x, y) = (0, 0) \mu\text{m}$. The potential minimum at greater *z*-distance is lower than the potential minimum at smaller *z*-distance. This is due location of the RF antenna at the atom chip and the decreasing magnetic field amplitude along the *z*-direction. The potential difference is 1506 Hz. Furthermore, the potential minimum at greater *z*-direction distance is wider than the potential minimum closer to the atom chip. This shape stems from the static magnetic field, which was created by a Z-structure on the atom chip and has a steeper curvature closer to the atom chip (see Figure 4.2). In Image **b**) the cigar-shape of the potential is very well visible. This is due to Ioffe-Pritchard type configuration of the static magnetic trap. The elongated from reflects the ratio of 0.29 between the weak trapping axis and the strong trapping axes. Additionally, image **c**) shows the tilt of the potential due to the Z-structure. The potential is tilted in the direction following the vertical wires of the Z-structure (see Figure 4.2).

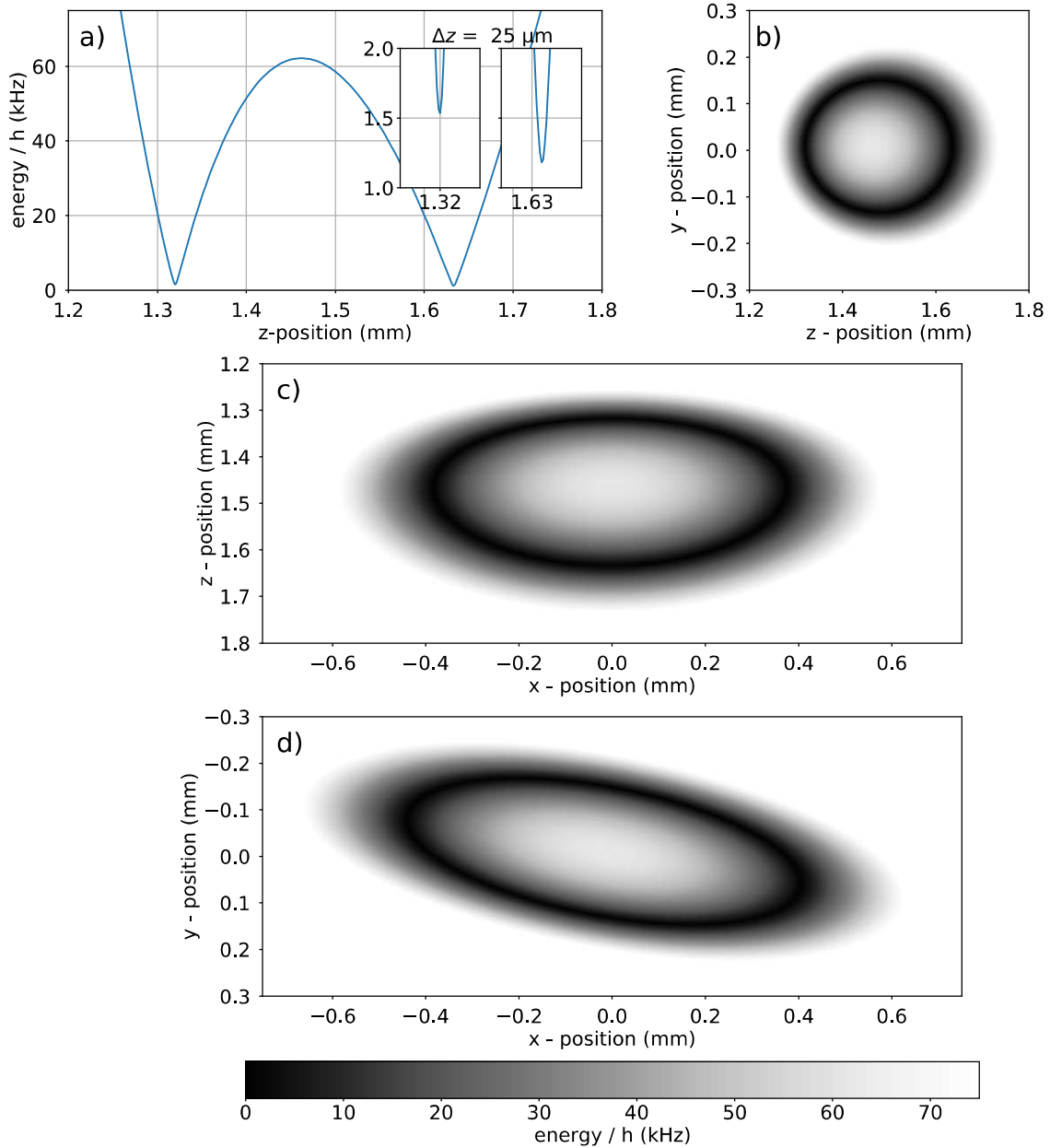


Figure 4.8: Slices through the shell potential at position *c*. The potential was calculated for a detuning of 31 kHz and a RF power corresponding to an AC current of 7.5 mA. Image **a**) shows the potential along the *z*-direction for $(x, y) = (0, 0) \mu\text{m}$. The potential minimum at greater *z*-distance is lower than the potential minimum at smaller *z*-distance. This is due to the location of the RF antenna at the atom chip and the decreasing magnetic field amplitude along the *z*-direction. The potential difference is 351 Hz. Furthermore, the potential minimum at greater *z*-distance is wider than the potential minimum closer to the atom chip. This shape stems from the static magnetic field, which was created by a Z-structure on the atom chip and has a steeper curvature closer to the atom chip (see Figure 4.2). In Image **b**) the cigar-shape of the potential is very well visible. This is due to the Ioffe-Pritchard type configuration of the static magnetic trap. The elongated form reflects the ratio of 0.34 between the weak trapping axis and the strong trapping axes. Additionally, image **c**) shows the tilt of the potential due to the Z-structure. The potential is tilted in the direction following the vertical wires of the Z-structure (see Figure 4.2).

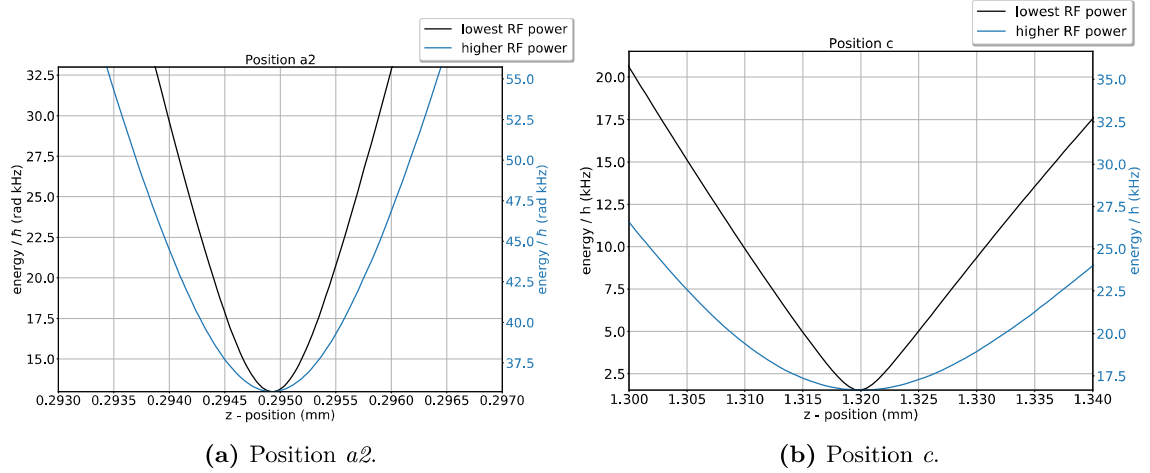


Figure 4.9: Comparison of the curvature at the minimum of the shell potentials. The potential was calculated along the z -direction for $(x, y) = (0, 0)$ mm for a detuning of 406 kHz and 31 kHz in case of position $a2$ and c , respectively. The two figures shown the region around the minimum closer to the atom chip. The black curves shows the potential for the lowest possible RF power, where atoms are still transferred to shell potentials. The blue curves show the potentials for the highest possible RF power in the setup. The y-axis is set to a range of 20 kHz. The x-axis range is $4 \mu\text{m}$ in case of position $a2$ and $40 \mu\text{m}$ in case of position c .

observable. The atom occupation of the shell potentials at position $a2$ and b under gravity and microgravity was calculated with Equation 4.16. A temperatures of $4 \mu\text{K}$ was chosen for both potentials. This temperature is close to the typical temperatures of the investigated thermal ensembles and illustrate the difference in occupation of the shell potential in microgravity and under gravity. The results are shown in Figures 4.12 and 4.13. As expected, the atoms are mainly occupying the lower part of the shell under gravity. Furthermore, the tilt in the x - y plane causes the atoms to have a higher density in the positive x -direction under gravity as well. Finally, the small *thickness* of the shell potential at position $a2$ confines the atoms closer to the minimum of the shell potential than at position b .

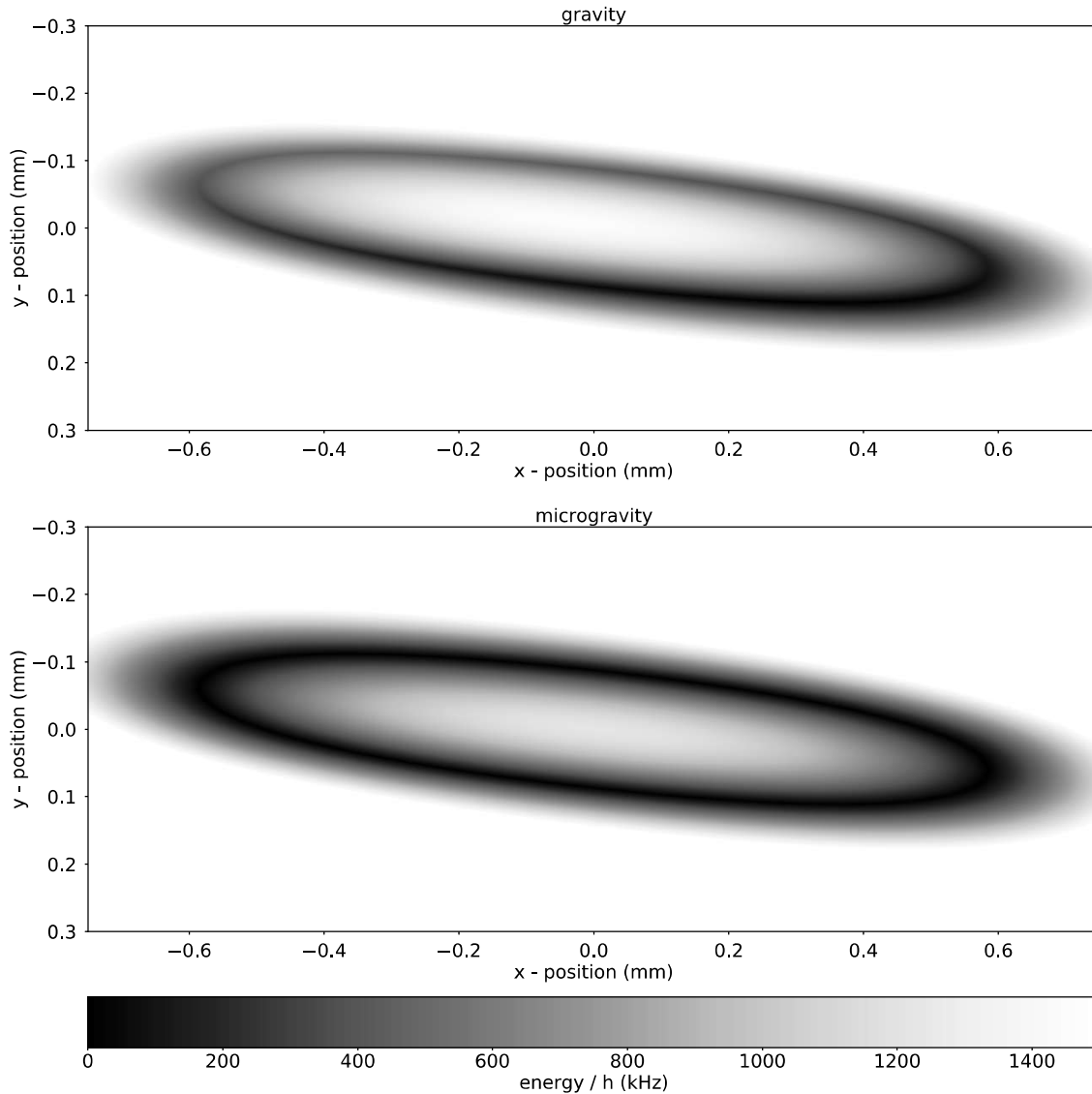


Figure 4.10: Shell potential at position $a2$ under gravity and in microgravity. Shown is a x-y plane at $z = 354 \mu\text{m}$. A detuning of 406 kHz and a RF power corresponding to an AC current of 28.4 mA was chosen. The potential was calculated according to Equation 4.18, where the magnetic quantum number was chosen to $m = 2$. The lower image was calculated without the gravitational part of the equation. Under gravity lower potential values are shifted towards the positive y-direction. However, the overall shape of the potential is preserved.

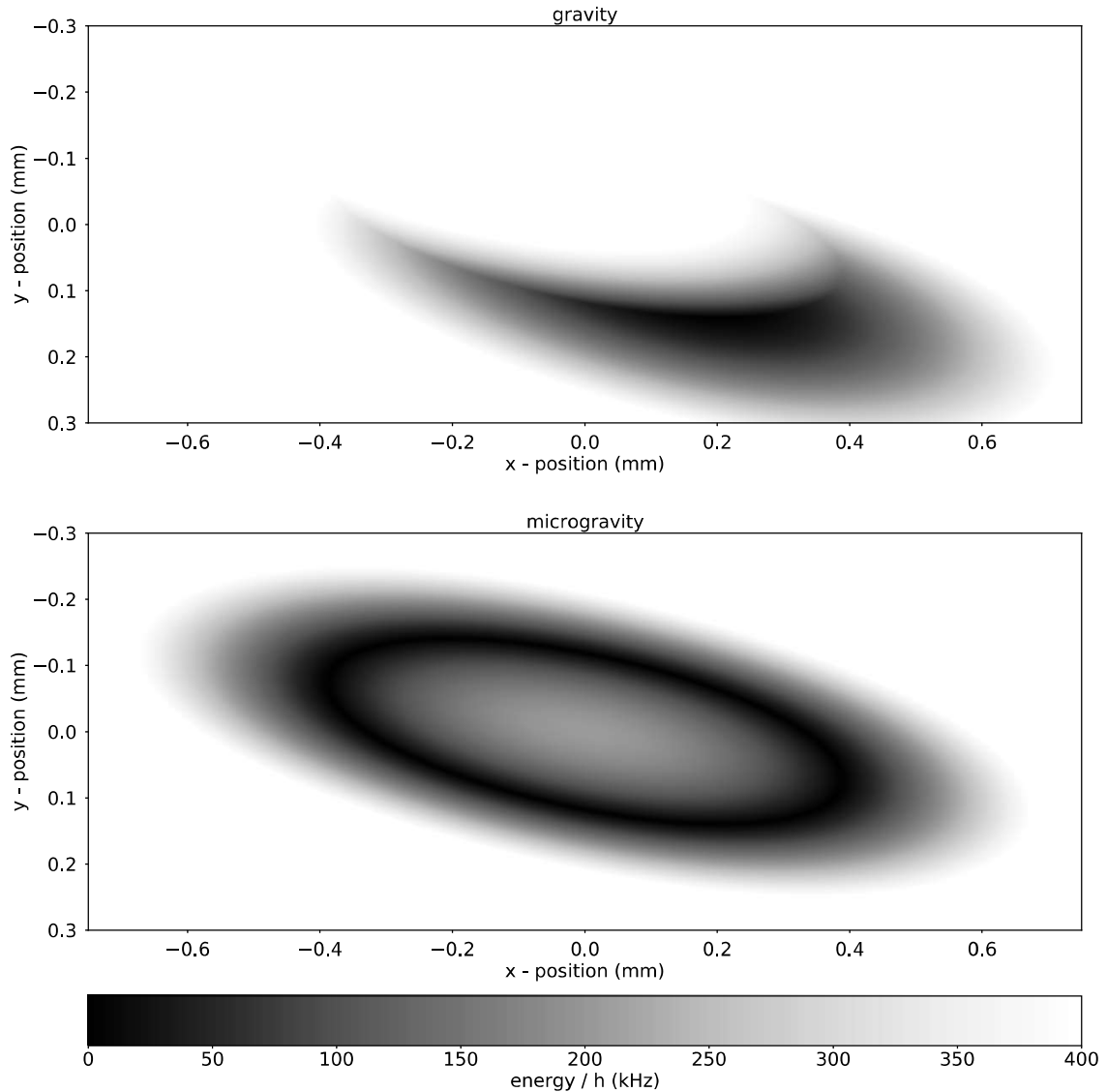


Figure 4.11: Shell potential at position b under gravity and in microgravity. Shown is a x - y plane at $z = 813 \mu\text{m}$. A detuning of 48 kHz and a RF power corresponding to an AC current of 11.0 mA was chosen. The potential was calculated according to Equation 4.18, where the magnetic quantum number was chosen to $m = 2$. The lower image was calculated without the gravitational part of the equation. The potential under gravity is significantly deformed and does not resemble a shell geometry anymore. This is due to the potential energy across the potential being around the same magnitude as the relative potential shift due to the gravitational acceleration.

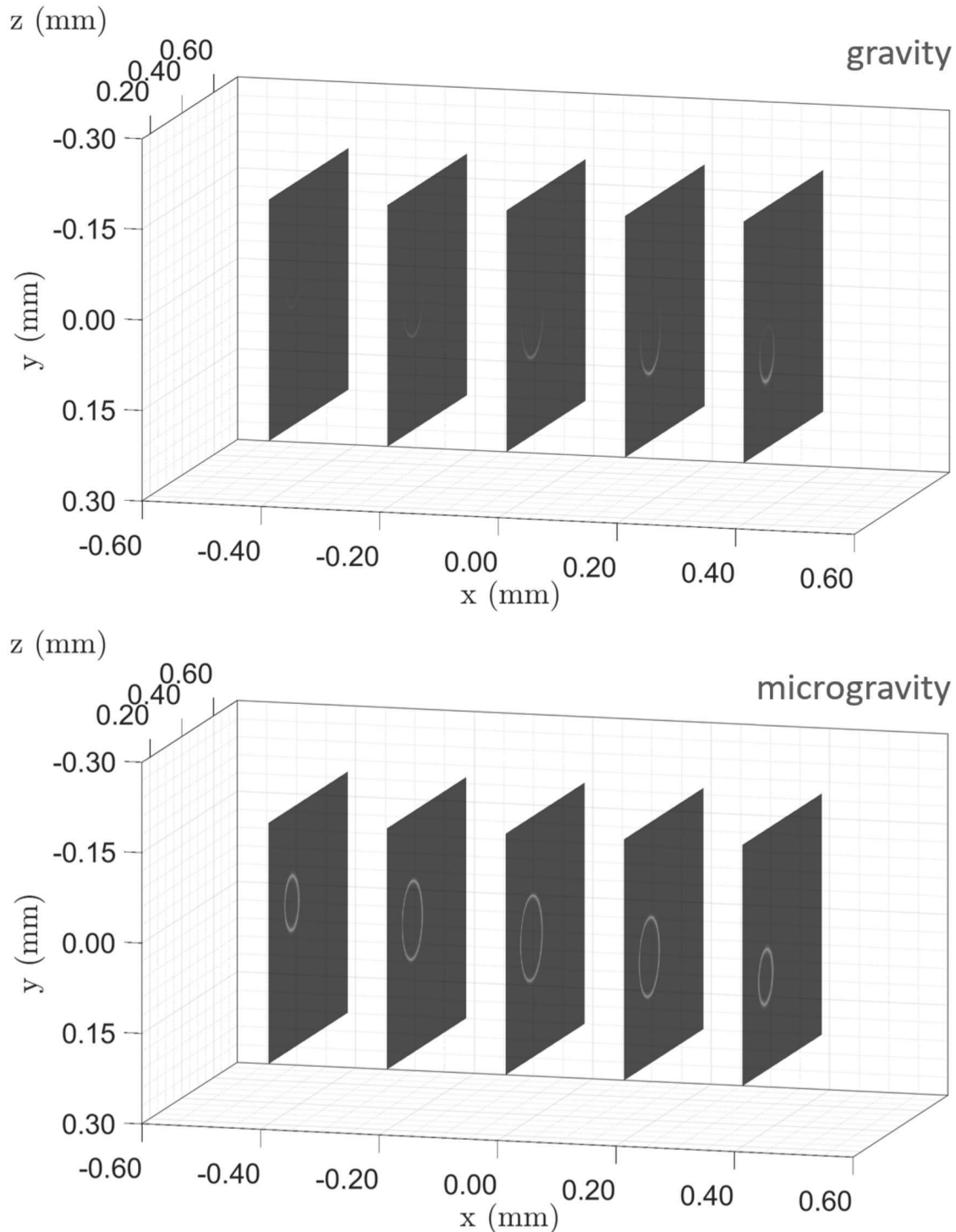


Figure 4.12: Atom occupation in the potential at position $a2$. Comparison of the distribution of thermal atoms with a temperature of $4 \mu\text{K}$ in the shell potential at position $a2$ with a detuning of 406 kHz and a RF power corresponding to an AC current of 28.4 mA with and without gravity. This potential is the same as shown in Figure 4.5(a). The slices are in the y - z plane and located at x position from -0.4 mm to 0.4 mm in 0.2 mm steps. The atom occupation in the potential is calculated with Equation 4.16. The color code indicates the normalized probability of finding an atom at the spatial position. Black on the gray scale represents a value of zero and white represents a value of one. With a temperature of $4 \mu\text{K}$ the whole potential could be occupied in microgravity. On the other hand, under gravity the atoms located at the lower part of the shell (gravity showing in the positive y -direction). The rotation of the potential in the x - y plane leads to a higher occupation of the part of the potential located at positive x -direction.

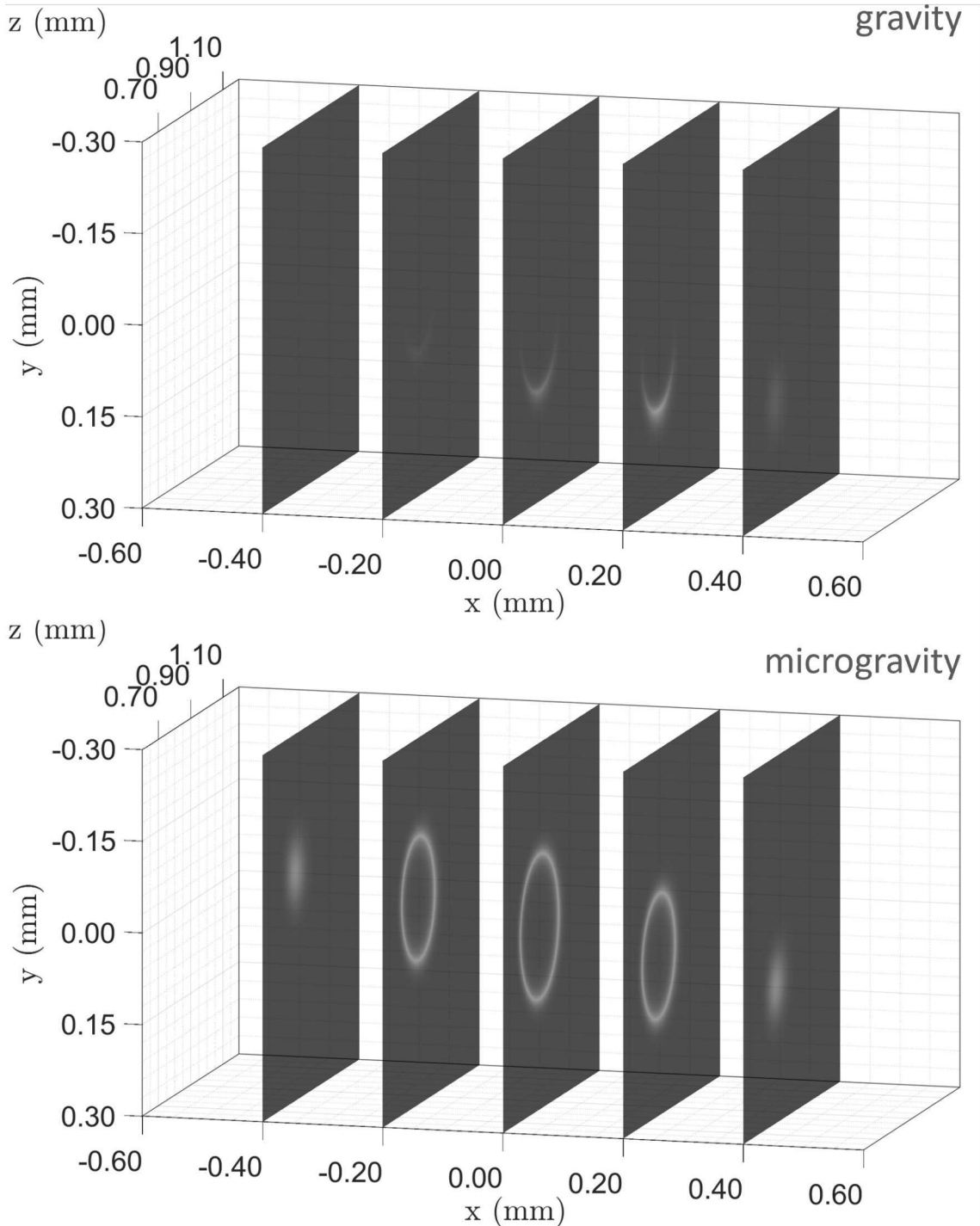


Figure 4.13: Atom occupation in the potential at position b . Comparison of the distribution of thermal atoms with a temperature of $4 \mu\text{K}$ in the shell potential at position b with a detuning of 48 kHz and a RF power corresponding to an AC current of 11.0 mA with and without gravity. This potential is the same as shown in Figure 4.5(a). The slices are in the y - z plane and located at x position from -0.4 mm to 0.4 mm in 0.2 mm steps. The atom occupation in the potential is calculated with Equation 4.16. The color code indicates the normalized probability of finding an atom at the spatial position. Black on the gray scale represents a value of zero and white represents a value of one. With a temperature of $4 \mu\text{K}$ the whole potential could be occupied in microgravity. On the other hand, under gravity the atoms located at the lower part of the shell (gravity showing in the positive y -direction). The rotation of the potential in the x - y plane leads to a higher occupation of the part of the potential located at positive x -direction.

4.4 Preparatory Measurement

RF source measurements To compare shell potential measurements and simulations knowledge of the AC current through the U-wire as a function of RF frequency and RF power is necessary. The impedance of the RF U-wire on the base chip and the connecting coaxial cable was measured with network analyzer (HP 3577A). The RF power output of the National Instruments PXI 5421 arbitrary waveform generator was measured with the Rhode & Schwarz FSH6 spectrum analyzer. The power measurement was performed at a frequency of 2 MHz. The results are shown in Figure 4.14. A polynomial of 2nd degree was fitted to the RF power as a function of the LabView power setting. The fitting results are shown in Equation 4.20. The AC current through the U-wire is calculated by

$$I(P_{50\Omega}, R_L) = 2 \frac{\sqrt{P_{50\Omega} \cdot 50\Omega}}{50\Omega + R_L}, \quad (4.19)$$

where $P_{50\Omega}$ is the measured power shown in Figure 4.14(a) and R_L the impedance shown in Figure 4.14(b).

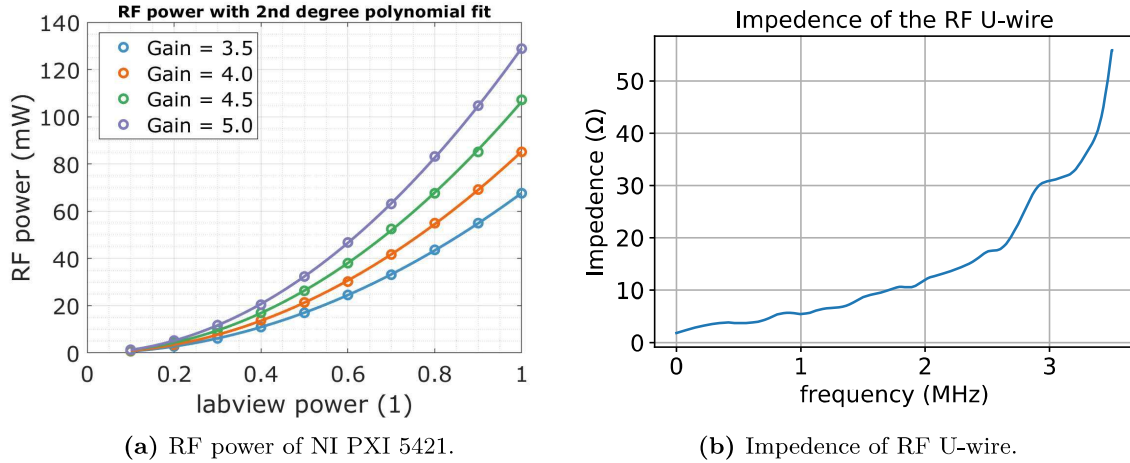


Figure 4.14: RF power and impedance of the RF setup. The RF power was measured with a *Rhode & Schwarz* FSH6 spectrum analyzer. The input impedance of the device was 50Ω . For each gain setting a 2nd degree polynomial function was fitted to the data. The resulting parameters are shown in Equation 4.20. The impedance of whole RF chain starting from the RF source (cables, connectors, vacuum feed-through, U-wire) was measured with a network analyser (HP 3577A).

$$\begin{aligned} \text{Gain} = 3.5 : \text{power} &= -0.0428 + 0.6207 \cdot x + 67.15 \cdot x^2 \text{ mW} \\ \text{Gain} = 4.0 : \text{power} &= +0.1150 - 0.3704 \cdot x + 85.54 \cdot x^2 \text{ mW} \\ \text{Gain} = 4.5 : \text{power} &= +0.5081 - 2.3230 \cdot x + 108.2 \cdot x^2 \text{ mW} \\ \text{Gain} = 5.0 : \text{power} &= -0.0861 + 0.7703 \cdot x + 128.4 \cdot x^2 \text{ mW} \end{aligned} \quad (4.20)$$

Temperature measurements The temperature of a cold atom cloud can be decreased by slowly decreasing the trapping frequencies of a magnetic trap. Shell potentials were created

after evaporating cooling of cold atoms and transporting them with a sigmoid current ramp to the final position. This leads to different temperatures at different positions. Furthermore, atoms can only be trapped at position c in microgravity and a time-of-flight measurement to determine the temperature at that position was not possible due to limited number of drops. To estimate the temperature in microgravity and to have a model for the temperature at different positions time-of-flight measurements after current ramps to different y-bias-coils currents were performed.

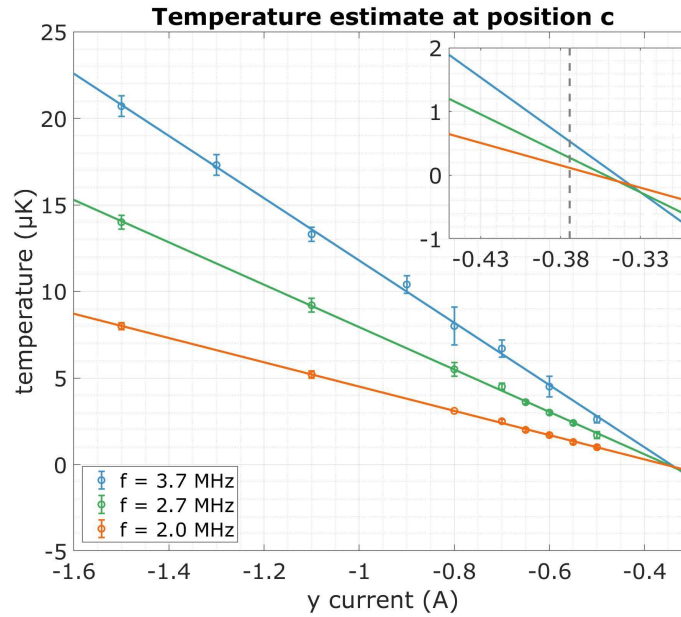


Figure 4.15: Cold atom cloud temperature after transport. The temperature after transport to a position further away from the atom was measured for three different final evaporation frequencies. First the atoms were cooled by evaporative cooling at a magnetic field configuration with a y-bias-coils current of -2.1 A and then transported with a sigmoid ramp in 150 ms to the final position determined by a y-bias-coils current between -1.5 A and -0.5 A. Afterwards a time-of-flight series was taken to determine the temperature of the cold atom cloud. To estimate the ensemble temperature at y-bias-coils current of -0.374 A a linear fit was applied to the data.

The measurement was performed for three different final RF frequencies of a short evaporation ramp (2.0 MHz, 2.7 MHz, and 3.7 MHz). The final magnetic field configuration at the end of the evaporation ramp was (*Base Chip Z*, *Science Chip Z*, x-bias-coils, y-bias-coils) = (6, 2, 0.5, -2.1) A. With a sigmoid current ramp the y-bias-coils current was reduced from -2.1 A to a final value between -1.5 A and -0.5 A in 150 ms. After a hold time of 10 ms the atoms were released from the trap and a time-of-flight series was measured. To the resulting absorption images was a Gaussian profile fitted. The temperature of the ensemble can be calculated from the kinetic energy in one dimension: $\frac{1}{2}m_{Rb}v^2 = \frac{1}{2}k_bT$. For a sufficiently long time-of-flight the σ -width of the Gaussian profile depends linearly on the time-of-flight and thus, the change of σ is the velocity. Taken together, this leads to

the following equation

$$T = \dot{\sigma}^2 m_{Rb} / k_b \quad (4.21)$$

where m_{Rb} is the mass of the rubidium 87 atom and k_b the Boltzmann constant. The temperature plotted against the y-bias-coils current is shown in Figure 4.15. A first degree polynomial was fitted to the data to estimate the temperature at a y-bias-coils current of -0.374 A (position c). This resulted in temperatures of 530 nK, 270 nK, and 110 nK for a final evaporation frequency of 3.7 MHz, 2.7 MHz, and 2.0 MHz, respectively. This are only rough estimates of the temperatures in the magnetic trap at position c , because of three reasons. First, the measurements were performed under gravity. This deforms the potential due to gravitational tilt (e.g. (17.5, 61.1, 59.8) Hz for position b in microgravity and (17.4, 54.4, 61.7) Hz under gravity). Second, the measurements were performed with a x-bias-coils current of 0.5 A. During the drops at position c the x-bias-coils current was 0.1 A and thus the trapping frequencies were higher ((9.1, 27.8, 24.6) Hz instead of (8.4, 24.9, 21.0) Hz). Third, the linear model for the temperature losses validity close to 0 K. Nevertheless, taking the good agreement with the linear model for the measured values and the consistent dependence of lower final evaporation frequency and the lower temperature it was decided that the above estimated temperature are good enough for a rough estimate of the temperature.

4.5 Transfer to Shell Potentials

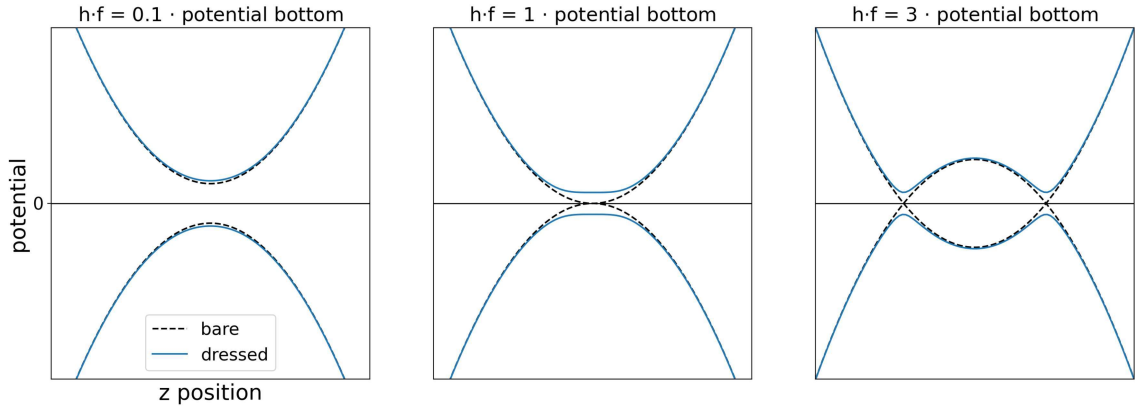


Figure 4.16: Illustration of the transfer to the dressed states. The different lines illustrate bare and dressed states in a harmonic magnetic potential with a radio frequency (RF) coupling. The title of each plot indicates the RF frequency in relation to the offset frequency of the potential bottom. This could be the situation of an atom in the $F = 1$ state in an Ioffe Pritchard magnetic trap, where the $m = 0$ state is not indicated. The cross section would be along one confining axis. The bare states $m = 1$ and $m = -1$ are indicated with a black dashed line and the dressed states $\tilde{m} = 1$ and $\tilde{m} = -1$ with the solid blue lines. Initially in the left picture a Rabi frequency with a frequency of 5 % of the potential bottom offset frequency and a RF frequency of 10 % of the potential bottom frequency is applied. The dressed state already deviate slightly from the bare states due to avoided crossing of coupled states. By increasing the RF frequency (and keeping the Rabi frequency constant) the bare states are shifted to the zero potential line and for RF frequency greater than the potential bottom offset frequency a crossing occurs. Due to avoided crossing of coupled states two minima are formed. Atoms formerly located in the $m = 1$ state are thus transferred into the $\tilde{m} = 1$ state. The energy difference at the minimum of the dressed state potential between the $\tilde{m} = \pm 1$ states is twice the Rabi frequency.

To transfer atoms from the bare states to the dressed states a coupling between different Zeeman states needs to be established. The rubidium 87 atoms are initially in the magnetic trap in the $F = 2$, $m_f = 2$ state. The atoms at the bottom of the magnetic trap at position $a\bar{2}$ have a frequency offset of 1.894 MHz. This is the energy difference between different m -states. To adiabatically transfer the atoms from the highest bare state to the highest dressed state one needs to start with a frequency below the potential bottom and ramp the frequency through the potential bottom to a frequency above it. This process is illustrated for a harmonic trapping potential in Figure 4.16. The duration of the ramp needs to be slow enough such that the atoms follow the potential adiabatically as described with Equation 4.12. Furthermore, the Rabi frequency needs to be high enough such that the Landau-Zener losses (see Equation 4.13) are minimized.

This Section limits the description of the transfer to dressed states to position $a\bar{2}$. The objective was to transfer as many atoms to dressed states as possible. Initially, after a short evaporation sequence, $7 \cdot 10^6$ atoms were in the magnetic trap. The transfer ramp needs to take the following points into account

- The RF frequency needs to be set before the RF power is ramped up. Doing it the other way round would violate the adiabaticity criterion (see Equation 4.12). Additionally, the aforementioned equation determines how fast the frequency and power is allowed to change.
- RF power: The Rabi frequency is proportional to the RF power. Thus, higher RF power leads to less Landau-Zener losses (see Equation 4.13) and a more efficient transfer to the shell potential.
- Opening of the shell: When the RF frequency passes the potential bottom offset frequency the potential starts to significantly deform and the trapped atoms are accelerated to follow the potential minimum. This process could excite oscillations and even lead to a loss of atoms. Hence, the opening time of the shell needs to be adjusted with respect to the loss of atoms and induced oscillations.
- Lifetime in the shell potential: Typically, the lifetime in shell potentials is in the order of seconds [72] and one does not need to take the shell opening time into account. Due to limiting RF power in this experiment some shell potentials have a lifetime in the order of the shell opening time. Hence, the acceleration of the atoms during the shell opening needs to be weighted against the lifetime in the shell. For lifetime measurements see Section 4.10.

Two different transfer procedures were tested. The first procedure, referred to as *procedure1*, combined the passing of the RF frequency through the potential bottom offset frequency with the opening of the shell. The starting frequency and the opening time were varied. The second procedure, referred to as *procedure2*, separated out the passing of potential bottom in an additional ramp. The shell opening time in this case was fixed to 150 ms and the start and stop frequency around the potential bottom was varied.

Procedure1 started with ramping up the frequency linearly in 1 ms to an initial value and afterwards ramping the RF power to its final value linearly in also 1 ms. The ramp of the RF power does not violate the adiabaticity criterion, because it is far above the minimum RF power changing time of $1 \mu\text{s}$ calculated by Equation 4.12 for typical detunings and Rabi frequencies. The RF frequency was then linearly ramped from the initial value to a final value located above the potential bottom offset frequency. Figure 4.18(a) shows the measurement performed in a shell potential with a detuning of 206 kHz and maximal possible RF power. The initial RF frequency was varied from 0.3 MHz to 1.8 MHz. Finally, the frequency was ramped in 150 ms to a final value of 2.1 MHz to open the shell. The value of 150 ms

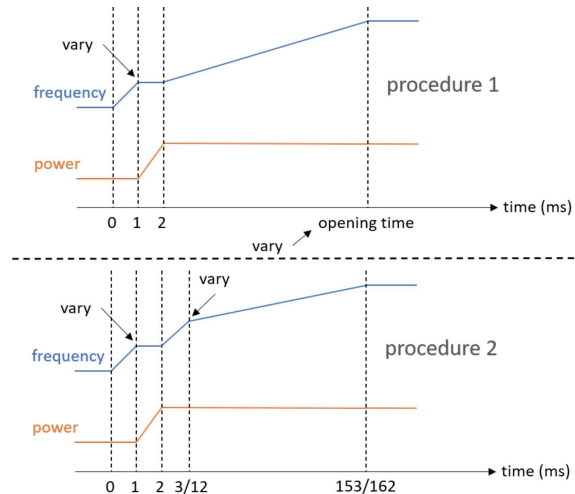


Fig. 4.17: Illustration of two transfer ramps.

The value of 150 ms

was found by trying out several durations; later the opening time will be systematically investigated. After a hold time of 10 ms the atoms were released from the shell potential by instantaneously switching off the RF power and the bias coils. The Z-structures of the atom chip were switched of 0.4 ms later. The response of the bias coils lead to an acceleration away from the atom chip. After 12 ms time-of-flight the atomic cloud was detected with absorption imaging. No dependence on the initial frequency to the detected atom number could be observed.

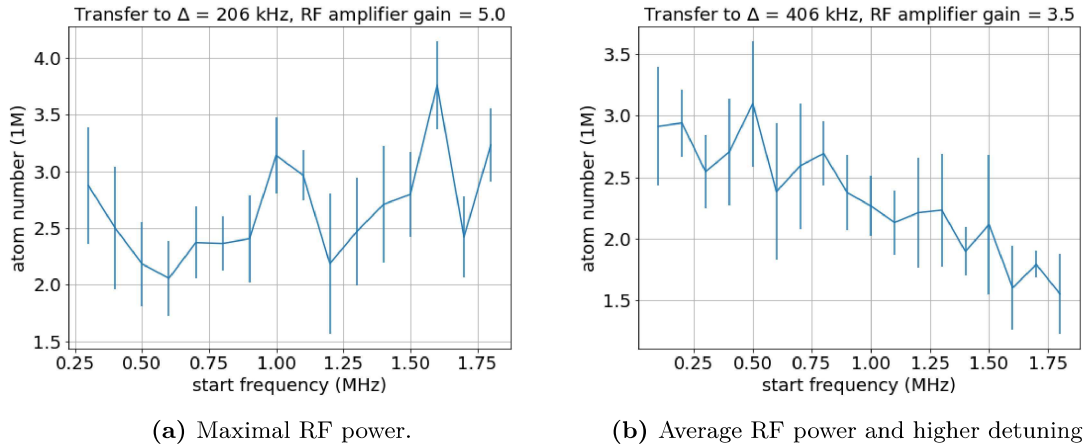


Figure 4.18: Simple transfer procedure from bare states to dressed states. To transfer atoms from the bare states to the dressed states the RF frequency was ramped from a frequency below the potential bottom offset frequency of 1.894 MHz, called "start frequency" here, to the final RF frequency of 2.1 MHz (a) or 2.3 MHz (b) within 150 ms linearly. Further difference between (a) and (b) was a higher RF power achieved by increasing the RF amplifier gain from 3.5 to 5.0. In (a) no clear dependence on the "start frequencies" is visible. The fluctuations are within 2 standard deviations. In (b) there is a decline towards higher "start frequencies" observable. The most likely explanation for the difference between (a) and (b) is the much higher lifetime of 430 ms in (a) in comparison to (b) 80 ms. Due to the ramp duration of 150 ms the decline in atom number for (b) is much more significant than (a). Hence, a lower start frequency causes the atoms to be for a shorter period of time in dressed state potential with a higher detuning. For details of the lifetime dependence on RF power and detuning see Section 4.10.

In contrast, with a lower RF power and higher detuning a dependence can be observed. For a final RF frequency of 2.3 MHz and a RF power corresponding to a Rabi frequency of 25 kHz a significant dependence can be observed in Figure 4.18(b). The reason is the short lifetime, which will be discussed in Section 4.10. In the case of the maximal RF power the lifetime was around 400 ms, while for the lower RF power the lifetime was around 80 ms. Hence, by changing the initial frequency and keeping the ramp duration constant one changes the time in the shell potential. To investigate whether a shorter ramp duration is possible a scan of the ramp duration between 10 ms and 300 ms in 10 ms steps was performed. By calculating the standard deviation of the x' - and y' -position for hold times between 0.1 ms and 20.1 ms it was concluded that 150 ms were enough to not excite oscillations in x' -direction and to reduce them by a factor of three in the y' -direction

compared to a ramp duration of 10 ms. The results are shown in Figure 4.19.

For *procedure2* the shell opening time was kept constant at 150 ms and started at a frequency slightly above the potential bottom offset frequency. Similarly to *procedure1* the RF frequency was linearly ramped to the "start frequency" value within 1 ms and afterwards the RF power was ramped linearly to the maximal value within 1 ms. The frequency was ramped linearly in 1 ms / 10 ms from the start value to the "stop frequency" value above the potential bottom offset frequency. The "start frequency" was scanned from 1.4 MHz to 1.9 MHz in 0.1 MHz steps and the "stop frequency" was scanned from 1.90 MHz to 2.00 MHz in 0.02 MHz steps. The final shell configuration had a detuning of 206 kHz (RF frequency of 2.1 MHz) and the maximal RF power was used. Both for a duration of 1 ms, shown in Figure 4.20, and for a duration of 10 ms, shown in Figure 4.21, no higher transfer efficiency than with *procedure1* (shown in Figure 4.18(a)) could be achieved. Furthermore, it can be observed that the transfer efficiency declines for increasing "stop frequency" values.

Procedure1 was chosen for all future measurements, because the additional ramp through the potential bottom at *procedure2* did not improve the efficiency. Moreover, *procedure1* allowed to use the same ramp for all shell potentials, because it did not need to be adjusted for different potential bottoms. For all future measurements a start frequency of 0.3 MHz and a ramp time of 150 ms was chosen. The only exception was the shell potential at position *c* in microgravity. Due to the limited number of available measurements the initial frequency was chosen closer to the potential bottom (start frequency of 1.8 MHz) to avoid opening the shell to quickly in case of a lower potential bottom than the simulation predicted. A too quick opening would lead to loss of atoms due non-adiabatic transfer of the atoms. The dependence of the transfer procedure on the RF power will be discussed in the next section.

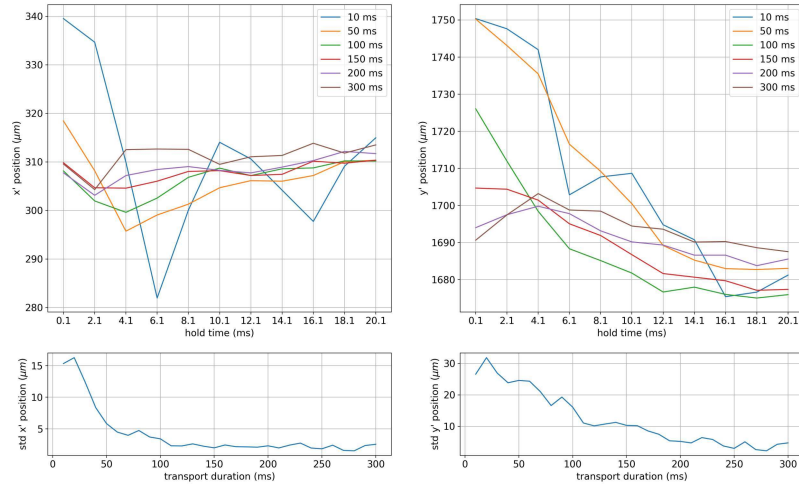


Figure 4.19: Transport duration scan of *procedure1* for a final frequency of 2.3 MHz (406 kHz detuning). The RF frequency was set to 0.3 MHz. Linear ramp durations between 10 ms and 300 ms in 10 ms steps were measured. For each ramp duration the hold time in the final dressed state trap was varied between 0.1 ms and 20.1 ms in 2 ms steps. At the end of the hold time all magnetic fields and the RF field were turned off instantaneously. After 6 ms an absorption image of the cloud was taken. The upper graphs show the center x' - and y' -position of the cloud. A clear oscillation is visible for a ramp duration of 10 ms in the x' -direction. In the y' -direction no oscillation is visible, but a drift in one direction. The oscillation amplitude decreases with increasing ramp duration. The standard deviation of the positions of each ramp duration are shown in the lower two graphs. A ramp duration of 150 ms was chosen, because no further decrease in the standard deviation in the x' -direction is visible.

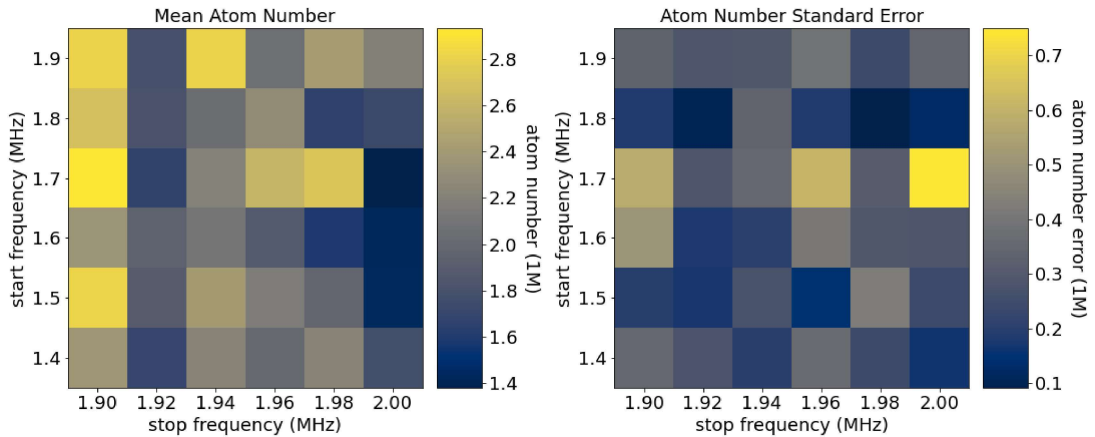


Figure 4.20: Transfer procedure (*procedure2*) from the bare states to the dressed states with an additional ramp through the potential bottom offset frequency (1 ms duration). The same final shell potential values as in Figure 4.18(a) were used. In contrast to *procedure1* the opening shell time was kept at 150 ms starting at a frequency slightly above the potential bottom offset frequency. An additional ramp through the frequency bottom was added. More details are provided in the text. It can be concluded that the transfer efficiency was not increased in comparison to *procedure1*.

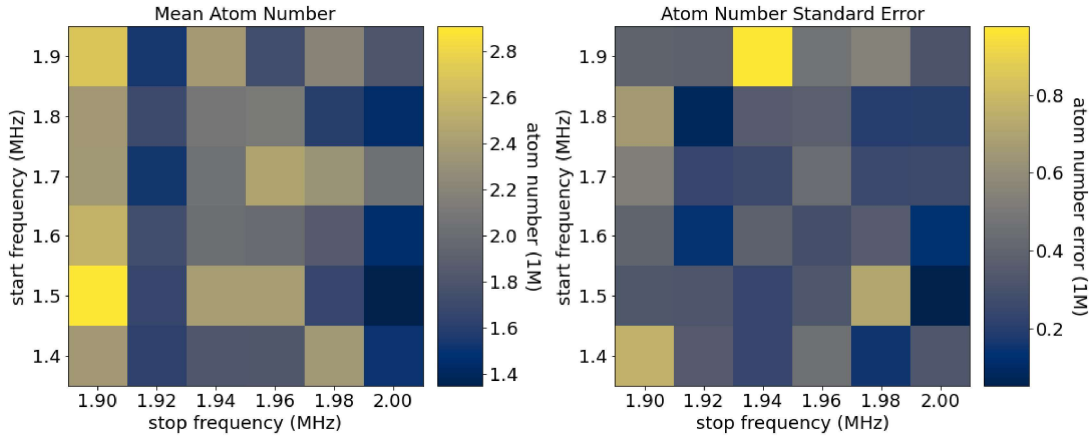


Figure 4.21: Transfer procedure from the bare states to the dressed states with an additional ramp through the potential bottom offset frequency (10 ms duration). The same measurement as in Figure 4.20, but with a duration of 10 ms instead of 1 ms. More details are in the aforementioned figure and in the text.

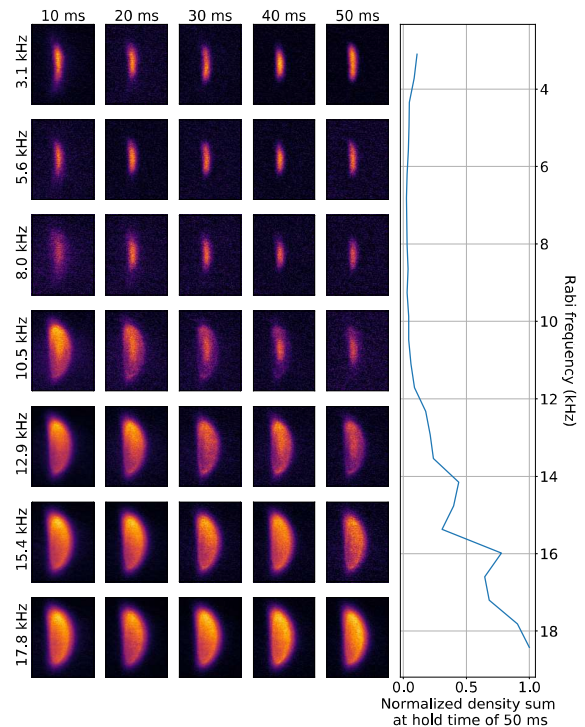
4.6 Rabi Frequency

In the simulation section the Rabi frequency was identified to be connected to how *homogeneous* the potential is on the surface and to the *thickness* of the shell surface. Furthermore, Landau-Zener losses are proportional to the Rabi frequency as described in Section 4.1.

The Rabi frequency is determined by the RF power and by the distance of the shell potential to the atom chip. Shell potentials closer to the atom chip demand higher detunings to achieve similar size. Hence, a higher Rabi frequency is necessary to achieve the same shell thickness as shown in Section 4.3.

The minimal Rabi frequency necessary for positions *a2* and *c* were determined. For position *a2* the measurements were performed on ground and for position *c* in microgravity. For position *a2* the transfer *procedure1* described in Section 4.5 was used: In 1 ms the RF frequency was ramped linearly to 0.3 MHz, afterwards the RF power was increased to the final value with a 1 ms linear ramp. Afterwards, the RF frequency was ramped to the final value of 2.3 MHz in 150 ms and held for 10 ms to 50 ms in the shell potential. Finally, an in-situ absorption image with a laser frequency detuned 12.15 MHz to the $F=2 \rightarrow F'=3$ was taken (see Figure 4.22). The LabView RF power settings were scanned from 0.1 to 0.6 in 0.02 steps. The global RF gain setting was set to 3.5 This corresponded to a Rabi frequency of 3.1 kHz to 18.4 kHz in 0.63 kHz steps. By visually inspecting the absorption images one concludes that at a Rabi frequency of around 10 kHz the atoms are starting to be transferred to the dressed states. At around 18 kHz most of the atoms are transferred to dressed states. The minimal Rabi frequency will be defined as the Rabi frequency, which was sufficient to transfer atoms to the shell potential and create an absorption image visible deviating from absorption images with a lower Rabi frequency at a hold time of 10 ms. Hence, the minimal Rabi frequency is 10.5 kHz corresponding to an AC current of 28.6 mA or a LabView power setting of 0.5.

Figure 4.22: Rabi frequency scan at position a2. The transfer procedure described in Section 4.5 was used. Hence, the RF power was initially set to 0.3 MHz, then the RF power was ramped to the final value. RF power LabView settings from 0.1 to 0.6 in 0.02 were scanned. For each power setting 5 different hold times from 10 ms to 50 ms were measured. The final RF frequency was 2.3 MHz corresponding to a detuning of 406 kHz. After the hold time an in-situ absorption image was taken. The columns of absorption images on the right show different hold times and the rows show different Rabi frequencies. Around a Rabi frequency of 10.5 kHz the transfer to the shell potential is beginning to be visible. The longer hold time show that only part of the atoms were transferred to the dressed states and a part of the atoms remained in the bare states and are still trapped in the magnetic trap. The line plot on the right shows the sum of all pixel density values in the shown absorption image for a hold time of 50 ms normalized to the highest value. This plot as well confirms that starting around a Rabi frequency of 10.5 kHz the transfer to dressed states starts to occur.



The minimal Rabi frequency at position *c* was measured for a detuning of 31 kHz. The transfer to dressed states was performed slightly different to *procedure1*. Instead of choosing the initial frequency to be 0.3 MHz it was chosen to be 1.8 MHz due to the shallow magnetic trap and a small detuning of 31 kHz. If the initial frequency was chosen to be 0.3 MHz the frequency would be most of the shell opening time below the frequency bottom offset of 1.969 MHz the shell opening would happen very quickly. A systematic determination of the transfer procedure was not possible due to the limited number of drops. Five different LabView power settings were chosen: 0.010, 0.025, 0.075, 0.125, and 0.250. This corresponds to Rabi frequencies of: ~ 0.0 kHz, 0.1 kHz, 0.6 kHz, 1.0 kHz, and 2.0 kHz. Figure 4.23 shows the result of these measurement. The simulated isomagnetic surface is projected on those images. The images with a Rabi frequency of up to 0.6 kHz indicate that no significant amount of atoms were transferred to dressed states. Starting at a Rabi frequency of 1.0 kHz most of the atoms are transferred to the dressed states. The overall shape of the atomic cloud in relation to the isomagnetic surface indicated by the white line at Rabi frequencies 1.0 kHz and 2.0 kHz is comparable and it is concluded that 1.0 kHz is the minimal necessary Rabi frequency. This corresponds to a LabView power

setting of 0.125 at a global RF gain setting of 3.5. The according AC current is 7.5 mA.

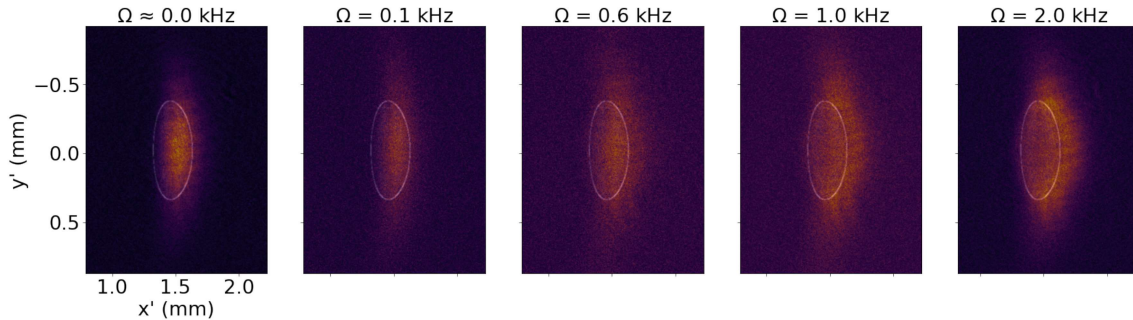


Figure 4.23: Scan of the Rabi frequency at position c and a detuning of 31 kHz in microgravity. The RF frequency was ramped linearly from 1.8 MHz to 2.0 MHz in 150 ms. The rf power was kept constant. The five shown Rabi frequencies were tested. At a Rabi frequency of 0.6 kHz part of the atoms are being transferred to the dressed state. At 1 kHz most of the atoms are transferred to the dressed states.

At position c the minimal Rabi frequency was additionally determined for a detuning of 231 kHz. In the sequence only the final RF frequency was changed from 2.0 MHz to 2.2 MHz. Measurements with LabView RF power of 0.025, 0.250, and 1.000 were performed, corresponding to a Rabi frequency of 0.1 kHz, 1.3 kHz, and 5.3 kHz. The result can be seen in Figure 4.23. At a Rabi frequency of 1.3 kHz part of the atoms are transferred to the dressed states and a part stays in the bare states. Due to the size of the shell potential they can be clearly distinguished. At a Rabi frequency of 5.3 kHz all atoms are transferred to the dressed states. Thus, the minimal Rabi frequency is between 1 kHz and 5 kHz, but due to the limited amount of possible measurements this was not further investigated. In comparison to a shell potential with a detuning of 31 kHz the minimal Rabi frequency is likely higher. This could result, because of two reasons. First, atoms in bare states could not clearly be distinguished from atoms in dressed states at absorption images with a detuning of 31 kHz. Hence, the minimal Rabi frequency is higher in that case. Second, with a higher detuning at the same Rabi frequency leads to steeper curvature around the shell minimum ($V \sim \sqrt{\delta^2 + \Omega_1^2}$). This in turn leads to higher Landau-Zener losses (see Equation 4.13).

Another observation should be mentioned: it is clearly visible that the shape of the isomagnetic surface deviate from the atom distribution. This measurement was repeated for a hold time of 50 ms instead of 10 ms. The result can be seen in Figure 4.28 (second image from the left). The simulation agrees with the measurement better in the x' -direction, but still deviates in the y' -direction. This indicates that the deviation could stem from atoms moving on the shell surface. The atoms are stronger confined in the x' -direction in comparison to the y' -direction. The hold time of 50 ms was probably not enough to move the atoms to the minimum of the shell potential in the y' -direction.

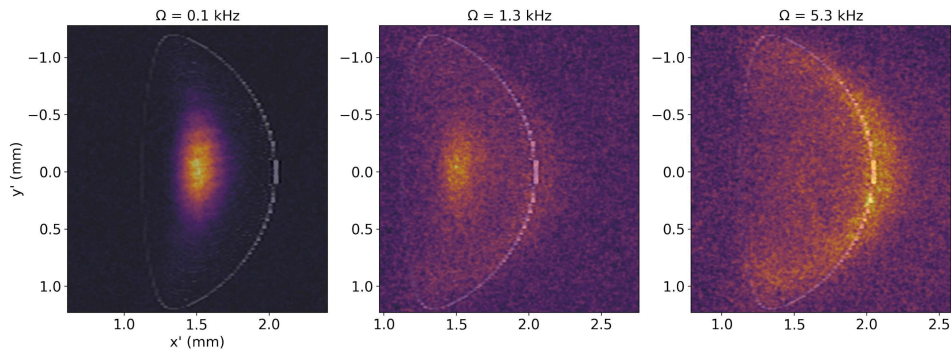


Figure 4.24: Scan of the Rabi frequency at position c and a detuning of 231 kHz in microgravity. The RF frequency was ramped linearly from 1.8 MHz to 2.2 MHz in 150 ms. The rf power was kept constant. The three shown Rabi frequencies were tested. At a frequency of 1. kHz part of the atoms are being transferred into the dressed state, but a significant part remains in the bare states in the center of the image. At at a Rabi frequency of 5.3 kHz the atoms are fully transferred into the dressed states.

4.7 Detuning

In this section the dependence of the shell potential on the RF frequency is investigated. The RF frequency will be given in terms of the difference between the frequency offset at the trap bottom of the magnetic trap and the used RF frequency. To satisfy the RWA criterion the detuning needs to be smaller than the RF frequency. This was satisfied in all cases.

The size of the detuning determines the *size* of the shell potential, because according to Equation 4.9 the shell potential has a minimum at the points in space where the Larmor frequency equals the RF frequency. In a sense the shell potential probes the shape of magnetic trap by trapping atoms on a surface of equal Larmor frequency dubbed the isomagnetic surface. From Equation 4.9 it is also obvious that the detuning determines the thickness of the shell for a constant Rabi frequency, because for a greater detuning δ the Rabi frequency Ω_1 has a smaller contribution.

The shell potentials at the positions $a2$, b , and c with different detunings were investigated. The position $a2$ was investigated on ground, while the position b and c were investigated in microgravity. The shell potential at position b was as well investigated in microgravity, because gravity distorts the shell potential at that position significant as can be seen in Figure 4.11. In-situ absorption images of the shell potentials at position $a2$ were taken simultaneously from the primary and the secondary imaging system. For positions b and c the images of the secondary detection system had a very low signal-to-noise ratio and are not shown here.

For the position $a2$ three different detunings are shown in Figure 4.25 and 4.26: 200 kHz, 400 kHz, and 800 kHz. This detunings were realized with RF frequencies of 2.194 MHz, 2.394 MHz, and 2.794 MHz. Figure 4.25 and 4.26 show the measurements taken from the primary and secondary detection system, respectively. The measurements were performed for three different hold times of 10 ms, 30 ms, and 50 ms to account for atom movement in

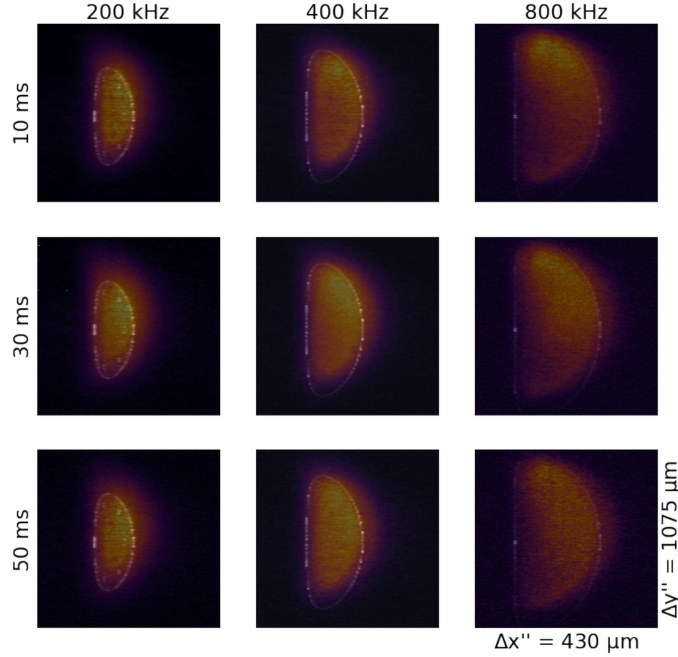


Figure 4.25: Scan of the detuning at position *a2* under gravity viewed from the primary detection system. The images were taken in-situ simultaneously from the primary and the secondary detection system with a detection frequency sweeping from a detuning -20 MHz to 20 MHz of the $F=2 \rightarrow F'=3$ line in 40 μs . The absorption images of the secondary detection are shown in Figure 4.26. The white line indicates the projection of the simulated isomagnetic surface on the detection system. Three different detunings (horizontal axis) and three different hold times (vertical axis) were scanned.

the trap and for short lifetimes. The measurements at position *b* (see Figure 4.27) were performed in microgravity with detunings of 48.1 kHz, 348.1 kHz, and 748.1 kHz realized with RF frequencies of 2.5 MHz, 2.8 MHz, and 3.2 MHz. The Rabi frequencies were 19 kHz, 17 kHz, and 16 kHz. The temperatures were 5 μK in case of a detuning of 48.1 kHz and 26 μK in case of the other two detunings. The reason for the much higher temperature were the restricted microgravity duration during that two drops. The evaporation stage was omitted and atoms were transferred to shell potentials directly from the magnetic trap.

At position *c* (see Figure 4.28) four different detunings were investigated: 31.2 kHz, 231.2 kHz, 431.2 kHz, and 631.2 kHz. This corresponds to a RF frequency of 2.0 MHz, 2.2 MHz, 2.4 MHz, and 2.6 MHz. In case of the first two detunings the temperature of the ensemble was estimated to be 0.5 μK (see Section 4.4). For the last two detunings only an upper limit of 16 μK can be given, though, the temperature was likely lower, because the 16 μK correspond to an ensemble at a steeper potential at position *b*.

The experimental results agreed with the simulation. Deviations were observed at position *a2* with a detuning of 200 kHz from the secondary detection system and at position *c* with a detuning of 231.2 kHz. In the first case the potential tilt due to gravity pulling the atoms to lower parts of the potential plus the small size and hence higher

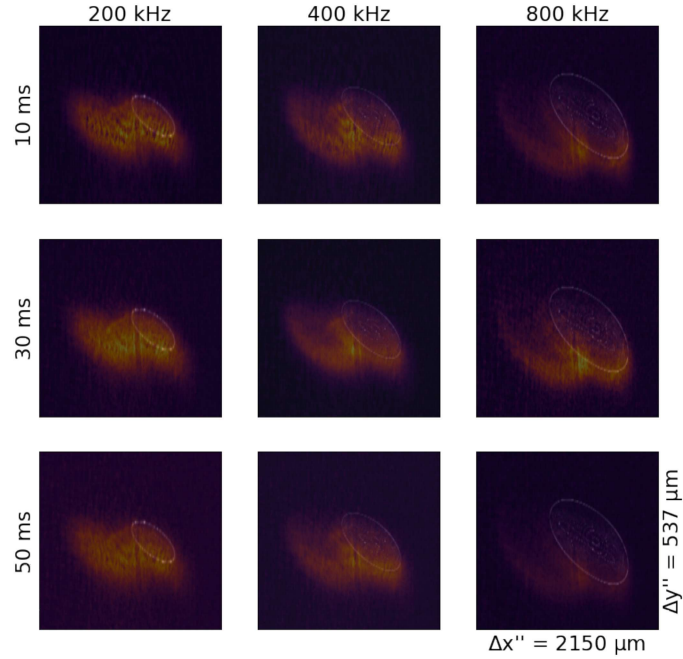


Figure 4.26: Scan of the detuning at position $a2$ under gravity viewed from the secondary detection system. The images were taken in-situ simultaneously from the primary and the secondary detection system with a detection frequency sweeping from a detuning -20 MHz to 20 MHz of the $F=2 \rightarrow F'=3$ line in $40 \mu s$. The absorption images of the primary detection are shown in Figure 4.25. The white line indicates the projection of the simulated isomagnetic surface on the detection system. Three different detunings (horizontal axis) and three different hold times (vertical axis) were scanned.

susceptibility to position correction uncertainties could explain the deviation. In the second case the size of the potential might be the cause. The absorption image presented in this section was taken after a hold time of 50 ms and in the previous section after a hold time of 10 ms. With a hold time of 50 ms the deviation in the x' -direction decreased in comparison to the hold time of 10 ms. Hence, the deviation in the x' -direction could stem from the ensemble not being at the minimum of the potential. The greater deviation in the y' -direction might be explained by the size of the potential in that direction. 50 ms hold time could have been not long enough for the atoms to reach the minimum of the potential.

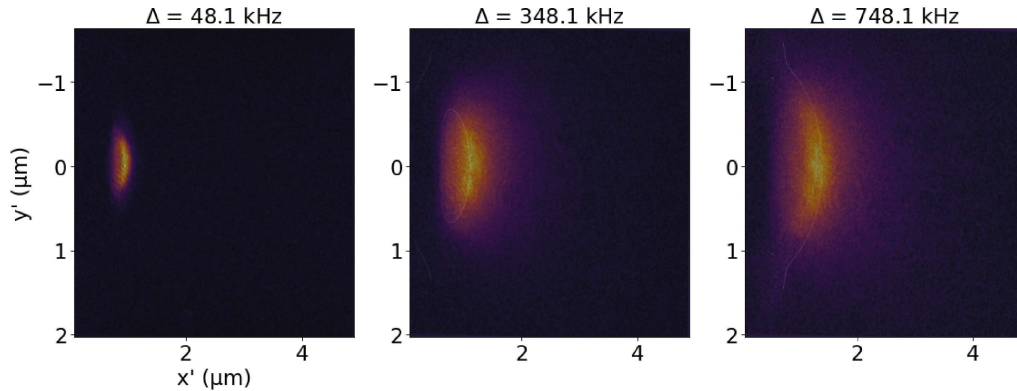


Figure 4.27: Scan of the detuning at position b in microgravity. The first two images show a closed shell potential, while the projection of the isomagnetic surface indicate an opening up of the potential. The atoms are mainly located at the atom chip opposing site of the potential.

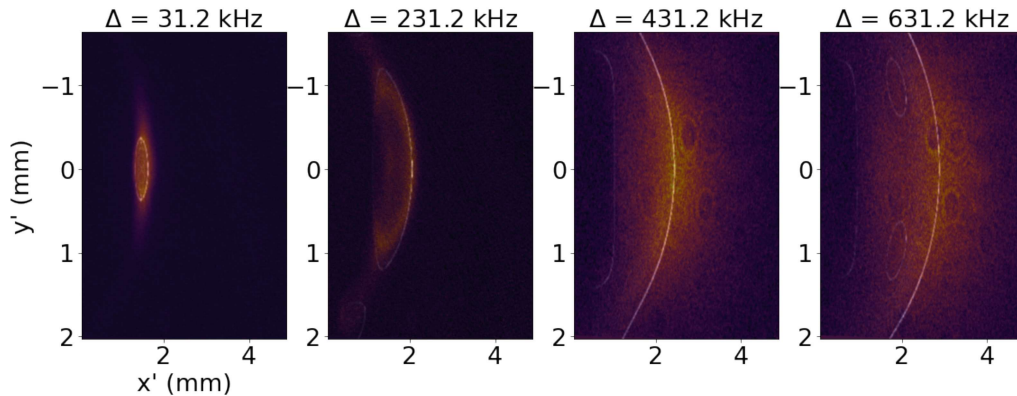


Figure 4.28: Scan of the detuning at position c in microgravity. The Rabi frequency at the minimum of the shell potential in the images with a detuning of 31.2 kHz and 231.2 kHz were 1.0 kHz and 5.3 kHz, respectively. The RF power in the last two images stayed the same as in the second image, but the simulation indicate that the isomagnetic surface was not a closed surface and we had not a shell potential, but an open potential with a minimum at the furthest distance from the atom chip.

4.8 Comparison - Gravity / Microgravity

A microgravity environment is beneficial for shell potential, because the potential tilt due to gravity is not distorting the the potential, atom are more homogeneously distributed on the shell, and shell configurations further away from the atom chip can be realized. The effects of gravity have already been discussed in the simulation section (see Section 4.3.1). Figures 4.29 and 4.30 show the comparison between a microgravity and gravity environment of shell potentials at positions $a2$, b , and c in the in-situ images from the primary and secondary detection system, respectively. The projection of the isomagnetic surface from the simulation on the absorption image is indicated with the white line. Detunings of 406 kHz, 48 kHz, 31 kHz, and Rabi frequencies of 31 kHz, 19 kHz, 1 kHz were chosen

for configurations at position a , b , and c , respectively. The thermal atoms in the bare states had a temperature $12 \mu\text{K}$ at position a , $5 \mu\text{K}$ at position b , and $0.5 \mu\text{K}$ at position c . The atoms at position a and b were transferred to dressed states by ramping the RF frequency from 0.3 MHz to a frequency of 2.3 MHz and 2.5 MHz in 150 ms, respectively. The configuration at position c was transferred to dressed states by ramping the frequency from 1.8 MHz to 2.0 MHz in 150 ms. In-situ images of the atoms were taken simultaneously from the primary and secondary detection system by sweeping the detuning from -20 MHz to 20 MHz in reference to the the $F=2 \rightarrow F'=3$ line. The images under gravity were taken just before the drop and are only minutes apart from the images in microgravity.

At position a no clear distinction between gravity and microgravity images is visible from the primary detection system. The difference is visible in the secondary detection system. While under gravity the atom density is higher at positive x and y direction in the images in microgravity the regions of higher atom density is at negative x and y direction. This agrees with the simulation results shown in Figures 4.10 and 4.5(a). The difference at position b is more obvious and can be seen in the primary detection and secondary detection images. In the primary detection system in microgravity the atom density is higher on the atom chip opposing side of the isomagnetic surface, while under gravity the atom density shape is less clearly distributed with respect to the isomagnetic surface. From the secondary detection system under gravity the atom density is located mainly below the isomagnetic surface, while in microgravity the atom density is located around the isomagnetic surface. This is consistent with the simulations shown in Figures 4.10 and 4.5(a), where the gravitational acceleration significantly tilts the potential. At position c no shell potential under gravity is possible.

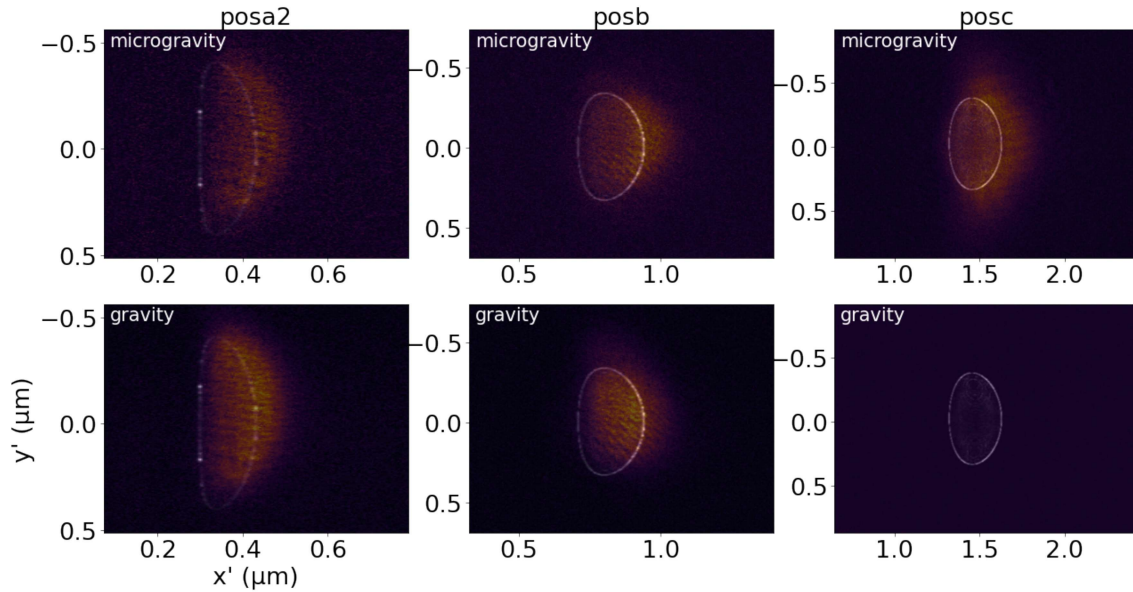


Figure 4.29: Comparison of shell potentials at positions $a2$, b , and c in microgravity and under gravity from the primary detection system. The white line indicates the position of the isomagnetic surface. The shell potential under gravity at position c contains no atoms, because the magnetic trap at that position is too weak to trap atoms.

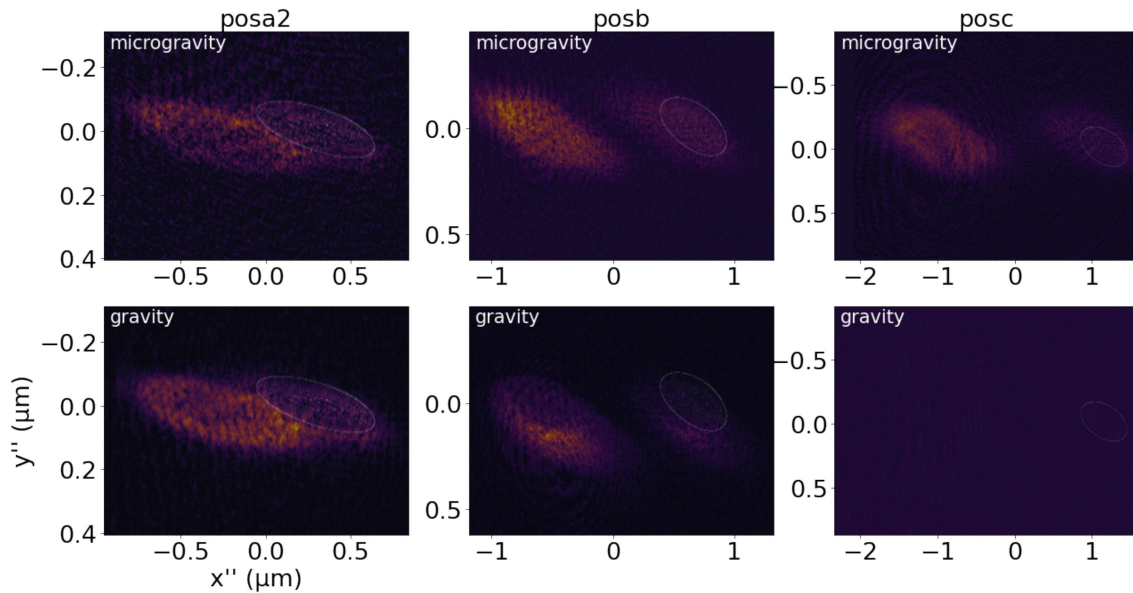


Figure 4.30: Comparison of shell potentials at positions $a2$, b , and c in microgravity and under gravity from the secondary detection system. The white line indicates the position of the isomagnetic surface. The shell potential under gravity at position c contains no atoms, because the magnetic trap at that position is too weak to trap atoms.

4.9 Temperature Dependence

The temperature of a thermal ensemble determines how far a shell potential is occupied with atoms and hence the absorption image shape. The occupation is described with Equation 4.16. The occupation of the shell potential at position c with a detuning of 31 kHz and a Rabi frequency of 1.0 kHz was investigated. The temperature was adjusted by changing the final RF frequencies of the evaporation ramp to 3.7 MHz, 2.7 MHz, and 2.0 MHz. By extrapolating temperature measurements on ground the following temperatures were estimated: $T_1 = 530$ nK, $T_2 = 270$ nK, and $T_3 = 110$ nK, respectively. Details on the measurement can be found in Section 4.4.

The atoms were transferred to the shell potential at position c the same way as described in Sections 4.7 and 4.6. The shell potential was detected with the primary detection system after a hold time of 10 ms in-situ by sweeping the detection frequency in $40 \mu\text{s}$ from -20 MHz to 20 MHz of the $F=2 \rightarrow F'=3$ line. The resulting images are shown in Figure 4.31. Additionally, the same images for the temperatures $T_1 = 530$ nK and $T_2 = 270$ nK were taken with a constant detection frequency 12.15 MHz detuned to the $F=2 \rightarrow F'=3$ line ($40 \mu\text{s}$ detection duration). These images are shown in Figure 4.32.

All images show an approximately equally sized ellipsoidal area. In images with a temperature of 530 nK a tail in positive and negative y' -direction can be observed. This tail is less pronounced at the images with a temperature of 270 nK and not visible in the image with a temperature of 110 nK. In images with a temperature of 530 nK and 270 nK an increased density can be seen at the ends the positive and negative y' -direction for the sweeping and constant detection. In case of the 110 nK image the signal-to-noise ratio is too low to identify the increased density. Aside from that, in the images taken with a sweeping detection frequency the atom density is equally distributed over the images. The image

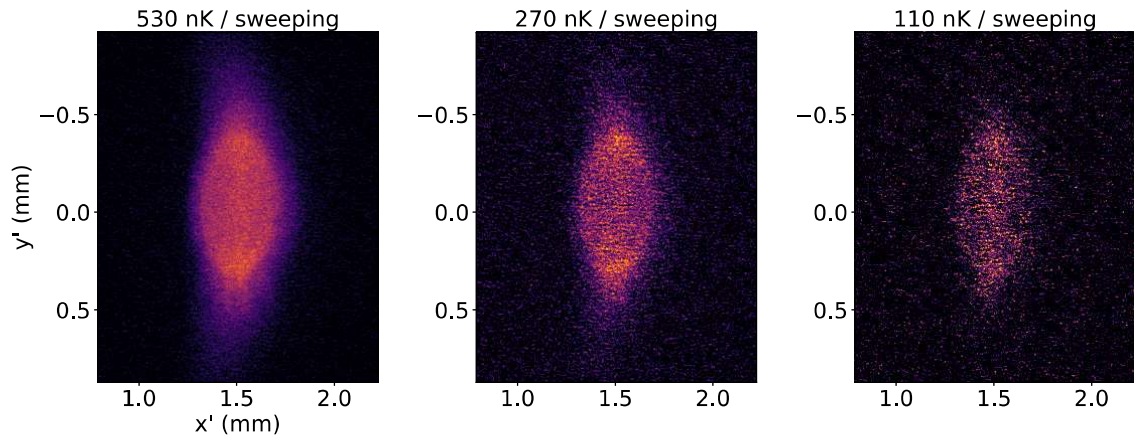


Figure 4.31: Different ensemble temperatures at position c . The shell configuration had a detuning of 31 kHz and a Rabi frequency of 1.0 kHz. The in-situ images were taken by sweeping in $40 \mu\text{s}$ the detection frequency from -20 MHz to 20 MHz of the $F=2 \rightarrow F'=3$ line. The temperature of the ensembles were determined by extrapolating the data from Figure 4.15. Lower temperatures were achieved by setting the final evaporation frequency lower. That in turn lead to a lower atom number and hence lower signal-to-noise ratio.

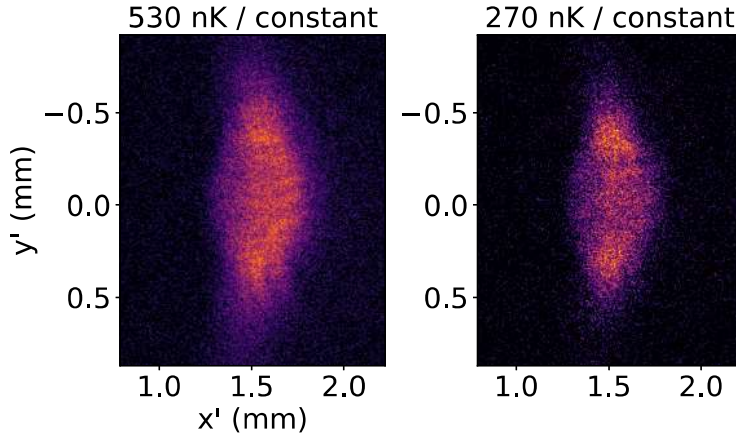


Figure 4.32: Different ensemble temperatures at position c. The shell configuration had a detuning of 31 kHz and a Rabi frequency of 1.0 kHz. The in-situ images were taken with a constant detection frequency of 12.15 MHz detuned to $F=2 \rightarrow F'=3$ line. The temperature of the ensembles were determined by extrapolating the data from Figure 4.15. Lower temperatures were achieved by setting the final evaporation frequency lower. That in turn lead to a lower atom number and hence lower signal-to-noise ratio.

taken with a constant detection frequency and an ensemble temperature of 530 nK shows an increased density in the positive x' -direction. At a temperature of 270 nK this is not observed anymore. To sum up, the images show increased density at positive and negative y' -direction and only for a temperature of 530 nK and constant detection frequency an increased density in positive x' -direction can be observed.

To compare the results qualitatively with the expected atomic distribution on the shell potential simulated absorption images were created. The potential was calculated on a $2 \times 2 \times 2 \mu m^3$ grid and the occupation with atoms was calculated with Equation 4.16. By summing up the calculated values along primary detection system direction (45° rotated in the x - y plane, see Figure 2.3) simulated absorption images were created. To recreate the pixel size of the experimental setup the simulated images were projected on an array with a pixel size of $3.58 \mu m$ using 3rd order spline interpolation. The simulated absorption images for temperatures of 530 nK, 270 nK, and 110 nK are shown in Figure 4.33(a). Due to the resolution of $2 \mu m$ a sharp edge can be seen. When the QUANTUS-2 apparatus was constructed in 2010 the resolution of the primary detection system was measured to be $5.52 \mu m$ [86] at the focus of the system located at $(x, y, z) = (0, 0, 0) \mu m$. Ensemble size and interference measurements indicate that the resolution has degraded and is likely around $20 \mu m$. This could possibly stem from a shift of the focus due to mechanical stress during the drop operation. To account for a lower resolution, the images were blurred with a Gaussian filter with a width of $11 \mu m$, $21 \mu m$, $32 \mu m$, $43 \mu m$, and $54 \mu m$. The results are shown in Figure 4.33(b). With increasing Gaussian width an increased density at positive and negative y' -direction can be observed. Nevertheless, an increased density at the outer parts of the shell can be here as well observed. Furthermore, to account for image noise a Poissonian distribution was added to the image. The mean of the distribution was chosen

to be located at 10 % to 50 % of the maximal pixel value of the image, hence, simulating a signal-to-noise ratio of 10 to 2. The results for a Gaussian width of $32 \mu m$ and $54 \mu m$ are shown in Figure 4.33(c) and 4.33(d), respectively. The images with added noise and a Gaussian width of $54 \mu m$ resemble the measurement with a constant detection frequency and an ensemble temperature of 530 nK the most. On the other hand, the simulated images agree less with the images taken with a sweeping detection frequency, because the experimental images show an equal density distribution aside from the increased density at positive and negative y' -direction.

The comparison of the simulation with the experimental images showed that the increased density at the positive and negative y' -direction could be explained by the resolution limit of the imaging system. Furthermore, the higher density at the region at higher x' -direction values (further away from the atom chip) visible in the images with the constant detection frequency could be reproduced in the simulated images. On the other hand, this asymmetry was not visible in images with the sweeping detection frequency. In general, it is not straight forward to extract the atomic density from in-situ absorption images due to different local quantization axes. The transition probability between two states ψ_i and ψ_j depends on the electric dipole moment \vec{d} and the polarization of the laser beam $\vec{\varepsilon}$

$$d_{ij} = \langle \psi_j | \vec{d} | \psi_i \rangle \cdot \vec{\varepsilon}$$

Hence, a lower density in the image could stem due to the product $\vec{d} \cdot \vec{\varepsilon}$ being lower. Furthermore, during the $F=2 \rightarrow F'=3$ transition the transition probability depends on detuning of the sub-states to the $F=2/F'=3$ line. Hence, at different potential values the transition probability and thus the imaged density is different. For that reason, it was expected that by sweeping the detection frequency one would image the atoms independent of the local detuning. Nevertheless, the constant detection frequency resulted in better qualitative agreement with the simulation.

To further investigate the atomic density in the images it would be beneficial to increase the signal-to-noise ratio by averaging several in-situ images. Additionally, by considering the local quantization axis and potential value on the simulated grid while adding the atomic density one could improve the prediction from the simulation.

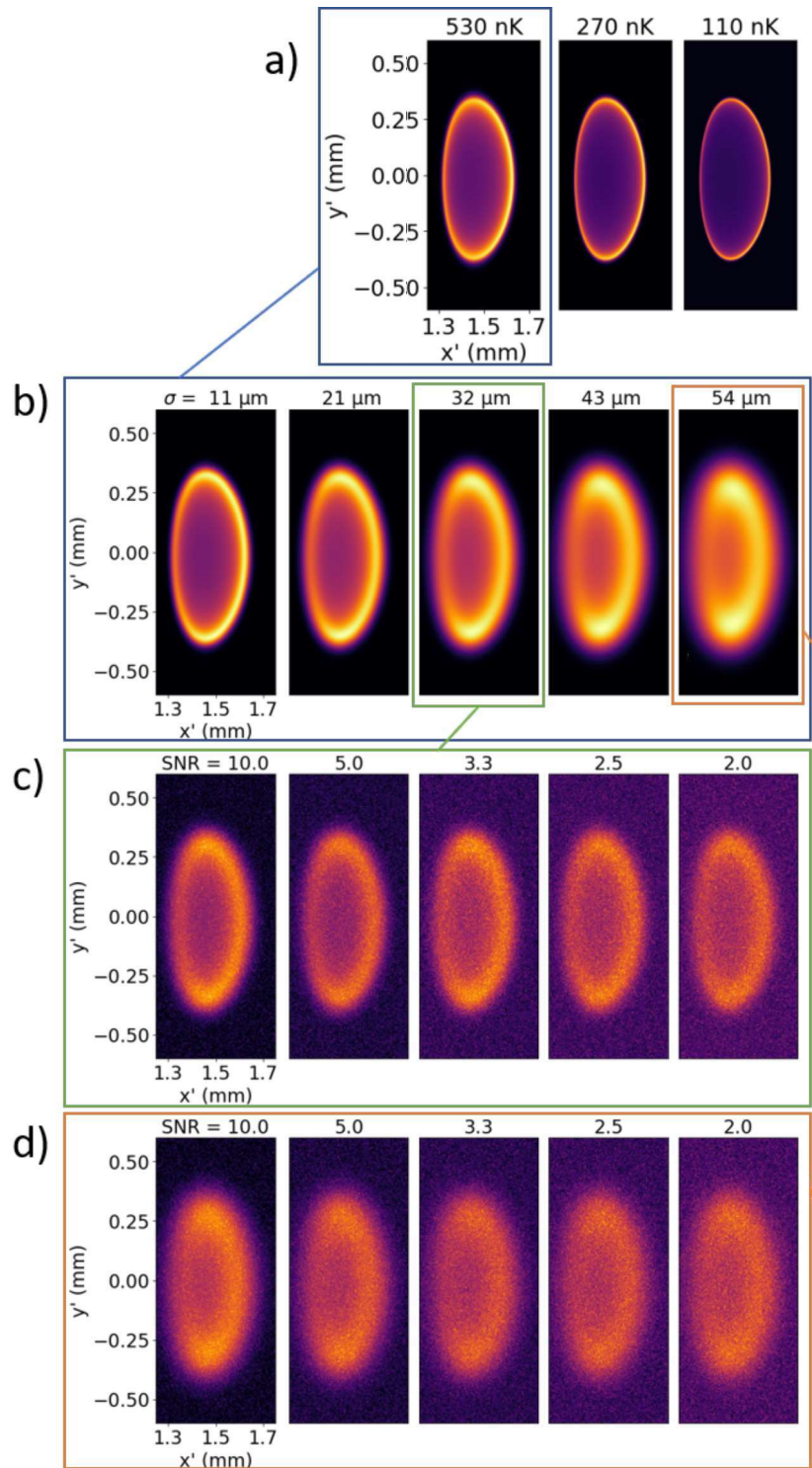


Figure 4.33: Simulation of the occupancy with thermal atoms of the shell potential at position c. The shell was simulated with a detuning of 31 kHz and a RF power corresponding to an AC current 7.5 mA, resulting in a Rabi frequency of 1 kHz. The occupancy with thermal atoms was calculated according to Equation 4.16. **a)** shows three columns with ensemble temperatures of 530 nK, 270 nK, and 110 nK. **b)** The image with a temperature of 530 nK was blurred with a Gaussian filter of different width. **c)** To the blurred image with a Gaussian width of 32 μm was Poissonian noise with a mean of 10 % to 50 % of the maximal signal added. Hence, a signal-to-noise-ratio of 10 to 2 was simulated. **d)** Poissonian noise was added to an image blurred with a Gaussian width of 54 μm . More details in the text.

4.10 Lifetime

The lifetime in the shell potential is important for future measurements with Bose-Einstein condensates. To study for example the dynamics of vortices one would need lifetimes of several seconds or up to minutes. Lifetimes in the range of minutes were already demonstrated in shell potentials [87]. The underlying magnetic trap of the shell potential has in our case a lifetime of several tens of seconds. Thus, the magnetic trap should not limit lifetimes in shell potentials. Lifetimes in shell potentials or in general in dressed state potential are mainly dominated by Landau-Zener losses and the RF source, where the main contributions come from the frequency stability, the amplitude stability, and from the frequency step size.

In Section 4.1 the Landau-Zener losses were introduced for a shell potential based on a magnetic quadrupole trap with the gravity vector aligned with strong trapping axis leading to Equation 4.13 for the decay rate:

$$\Gamma \approx \frac{4\omega_z}{\pi} \exp\left(-\frac{\pi\Omega_1^2}{2\alpha} \sqrt{\frac{M}{2E}}\right),$$

where ω_z is the trapping frequency perpendicular to the shell surface, Ω_1 the Rabi frequency, α the curvature of the underlying magnetic trap, M the mass of the atom, and E the energy of the atomic ensemble. The Landau-Zener losses are due to spin flips at the potential minimum (see for example illustration in Figure 4.16). The losses are thus govern by the Rabi frequency Ω_1 , which determines the splitting between trapping and non-trapping states at the potential minimum, by the velocity of atoms passing through the minimum (proportional to the energy of the atomic ensemble), and the potential curvature around the minimum of the shell. In turn, the curvature depends on the ratio of the detuning and the Rabi frequency, because the potential is proportional to $\sqrt{\delta^2 + \Omega_1^2}$. To sum up, the expected factors to the lifetime are

- Rabi frequency Ω_1 : Determines the splitting between the trapping and non-trapping potential and the curvature around the minimum.
- Detuning δ : Determines the curvature around the minimum for a given Rabi frequency.
- Ensemble temperature: Determines the rate of the atoms passing through the potential minimum, where the probability for a spin flip is the highest.

Typically, other experiments not using atom chip, but macroscopic coil configurations are able to find an analytical solution for the Landau-Zener losses, similar to the above equation, due to alignment of the gravity vector with surface normal vector and homogeneous Rabi frequency distribution over the shell [87]. In our case neither are the aforementioned vectors aligned nor is the Rabi frequency distribution homogeneous. Hence, numerical calculations are necessary to predict the Landau-Zener losses. This would have been out of scope for this work and was not pursued. However, the above equation was used to qualitatively understand the lifetime limiting factors.

The lifetimes in shell potentials at position $a2$ and b were measured. After transferring the atoms to the shell potentials as described in Section 4.5 the atoms were held for up to

800 ms, depending on the lifetime. Afterwards the RF power and frequency, and the bias coils were turned off and after further 0.25 ms were the atom chip structures turned off. This caused the atoms to accelerate away from the atom chip and to make them better detectable. The atoms were imaged with absorption imaging after a time-of-flight of 12 ms at position $a2$ and 16 ms at position b . To the resulting absorption images was a Gaussian distribution fitted and the atom number extracted. The atom number was then plotted against the hold time in the shell potential. To the resulting data the following function was fitted:

$$N(t) = N_0 e^{-t/\tau}, \quad (4.22)$$

where N_0 is the atom number after 10 ms hold time and τ the lifetime. Figure 4.34 shows the fit of the lifetime for position $a2$ with a detuning of 206 kHz and maximal RF power.

The lifetime was measured for different RF power values. The results are shown in Figure 4.35. The lifetime at position $a2$ was measured for detuning of 406 kHz and 206 kHz and at position b for a detuning of 25 kHz, 48 kHz, and 100 kHz. The RF power was mapped to the Rabi frequency by using the simulation described in Section 4.3 and calculating the Rabi frequency at the minimum of the shell potential. The measurement was started with maximal RF power and it was lowered until the lifetime was around 50 ms. The results for position $a2$ and b differ significantly.

The lifetime at position $a2$ is limited by the RF power and did not exceed (388 ± 22) ms. Below a Rabi frequency of 35 kHz the lifetime stays approximately constant and drops further for values smaller than 20 kHz. For Rabi frequencies values above the 35 kHz the lifetime at the smaller detuning is constantly above the lifetime at the larger detuning. The data indicates that the lifetime is limited by the RF power.

The lifetime at position b shows a significantly different behavior. It linearly decreases with the Rabi frequency. For example, at a detuning of 48 kHz the lifetime increases to a value of (243 ± 25) ms at a Rabi frequency of 3.8 kHz from an initial value of (112 ± 8) ms at at Rabi frequency of 26 kHz and quickly drops afterwards to (69 ± 5) ms at a Rabi frequency of 1.9 MHz. Atoms are not transferred to shell potentials for lower Rabi frequency values. The data indicates that the lifetime is not limited by the RF power.

The shell potential at position b is strongly distorted by gravity (see Figure 4.11), while at position $a2$ the potential still resembles a shell potential under gravity (see Figure 4.10). To verify that the lifetime is limited by the RF power at position $a2$ the lifetimes in shell

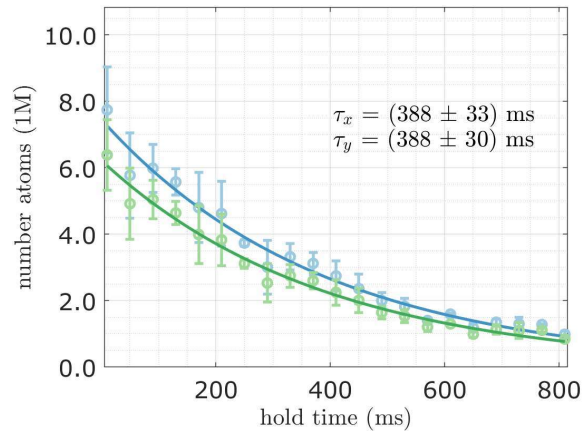


Fig. 4.34: Lifetime fit at position $a2$ for maximal RF power and a detuning of 206 kHz. The green colored data was extracted from the row profiles (y-direction) and the blue colored data from the column profiles (x-direction) of the absorption images.

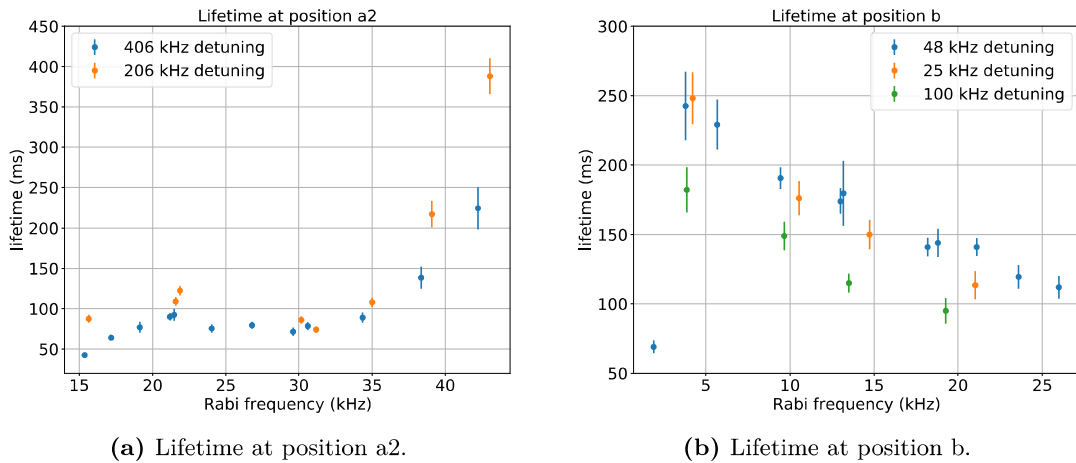


Figure 4.35: Lifetime measurements at position $a2$ and b . The atoms were initially transferred to the shell potentials as described Section 4.5 and held up to 800 ms in the potential. The atoms were detected 12 ms or 16 ms after release from the shell potential in case of potential at position $a2$ and b , respectively. To extract the lifetime from the measurement Equation 4.22 was fitted to the number of atoms as a function of the hold time. Figure 4.34 shows an example of such a fit. For the potential at position $a2$ an initial increase of lifetime is observed until a Rabi frequency of 21 kHz. Afterwards the lifetime stays approximately constant for up to a Rabi frequency of 35 kHz. A rapid increase of the lifetime is observed afterwards. The maximal Rabi frequency is limited by the maximal RF power. For a detuning of 206 kHz a lifetime of (388 ± 22) ms is reached. In case of position b the lifetime increases with decreasing Rabi frequency reaching a value of (243 ± 25) ms at a Rabi frequency of 3.8 kHz and a detuning of 48 kHz. At lower Rabi frequencies the lifetime sharply drops to (69 ± 5) ms at a Rabi frequency of 1.9 kHz. For lower Rabi frequency atoms are not transferred to shell potentials.

potentials closer to the atom chip were measured (see Table 4.2). Potentials closer to the atom chip have higher Rabi frequencies, because the RF antenna is located on the atom chip. The results are shown in Figure 4.37. For a z -distance of $150 \mu\text{m}$ to the atom chip, a detuning of 120 kHz, and maximal RF power a lifetime of (1481 ± 189) ms could be reached. For distances further away from the atom chip the lifetime decreases. On the other hand, for a distance of $100 \mu\text{m}$ the lifetime decreases again to (1421 ± 155) ms.

Finally, the lifetime dependence on the ensemble temperature was investigated. At position $a2$ and a detuning of 106 kHz the lifetime was measured for ensemble temperatures of $12.5 \mu\text{K}$, $8.5 \mu\text{K}$, and $3.0 \mu\text{K}$. The temperatures were adjusted by varying the RF frequency of the final evaporation ramp. These temperatures correspond to a final frequency of 3.7 MHz, 2.7 MHz, and 1.7 MHz, respectively. The measurement was repeated for three Rabi frequencies: 28 kHz, 19 kHz, 14 kHz. The results are shown in Figure 4.36. The resulting dependence of the lifetime on the temperature shows the exact opposite of the expected behavior. The lifetime increases approximately linearly with the temperature. On the other hand, the Equation 4.13 predicted that the lifetime would increase with decreasing temperature, because at lower temperatures the atoms would have a lower velocity and would have a lower probability to undergo a spin-flip when passing the minimum of the

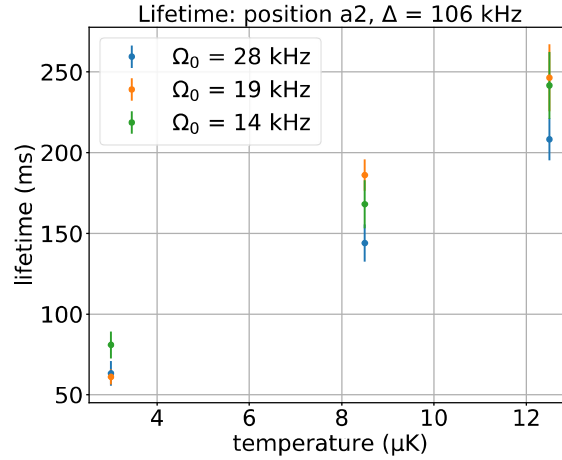


Figure 4.36: Lifetime at position $a2$ for different ensemble temperatures. The measurement was performed for a detuning of 106 kHz at position $a2$ for three different Rabi frequencies: 28 kHz, 19 kHz, and 14 kHz. The temperature of the atomic ensemble was adjusted by lowering the RF frequency of the final evaporation ramp. The temperatures of $12.5 \mu\text{K}$, $8.5 \mu\text{K}$, and $3.0 \mu\text{K}$ correspond to final RF frequencies of 3.7 MHz, 2.7 MHz, and 1.7 MHz, respectively.

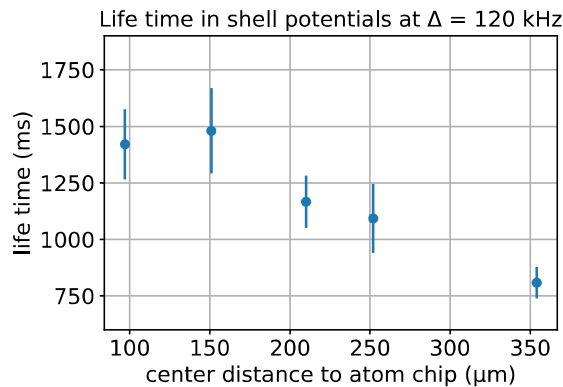


Figure 4.37: Life time in shell potentials as a function of the distance to the atom chip. To investigate whether the small RF power output was the reason for short lifetimes in the shell potentials the distance to the atom chip was varied and the lifetimes was measured. The detuning was set to 120 kHz and the trap geometry was chosen such that the trapping frequencies of the underlying magnetic traps were similar to the trapping frequencies at position $a2$. The exact trap parameters are shown in Table 4.2. An increase of the lifetime for traps closer to the atom chip can be observed. The likeliest explanation is the increase of the Rabi frequency due to the increased proximity to the RF antenna. The lifetime of the first data point at around $100 \mu\text{m}$ is lower than the next data point. The possible reasons could be the uncertainty of the determination of the lifetime or the proximity to the atom chip leading to magnetic field corrugation, because of the atom chip structures.

potential.

This section showed that the lifetime in shell potentials shows a complicated behavior. Application of Equation 4.13 to shell potentials created in this setup provides almost no insight. This is likely due to the gravitational vector not being aligned with a symmetry axis of the shell potential. This leads to an asymmetrical gravitational tilt in the potential. Furthermore, the anisotropic distribution of the Rabi frequency on the shell surface leads to regions with different lifetimes. To acquire predictions for the lifetime a numerical calculation is necessary, which includes the exact shape of the potential and the dynamic of the atomic ensemble. H el ene Perrin and Barry M. Garraway indicate in Chapter VIII of their review on radio-frequency adiabatic potentials [79] how such a calculation could be performed, but refrain from calculating the decay rate for a realistic adiabatic potential and only apply the calculations for a toy model. Thus, to perform such a calculation would have been out of the scope of this thesis and could be the subject of future investigations.

Nevertheless, insights on the lifetime dependences could be extracted. First, for the potential at position $a2$ and potentials closer to the atom chip the lifetime is limited by the RF power. Second, the lifetime increases with decreasing detuning. On the other hand, the constant lifetime at potentials at position $a2$ in the intermediate Rabi frequency range, the decreasing lifetime with increasing Rabi frequency at potentials at position b , and the decreasing lifetime with decreasing temperature could not be explained. A possible explanation could be that the atoms are occupying different regions of the shell potential for different parameters. These regions might have a lower lifetime. This question could possibly be answered with numerical calculations.

Table 4.2: Magnetic field configuration for lifetime measurements. The trapping frequencies and the potential bottom offset was chosen such that they are close to the values at position $a2$.

	Pos. 1	Pos. 2	Pos. 3	Pos. 4	Pos. a2
$(x_{min}, y_{min}, z_{min})$ (mm)	(0.07, 0.006, 0.0967)	(0.06, 0.008, 0.151)	(0.06, 0.009, 0.210)	(0.05, 0.01, 0.252)	(0.04, 0.01, 0.354)
(f_x, f_y, f_z) (Hz)	(11.86, 275.23, 284.56)	(14.41, 241.95, 250.64)	(17.14, 218.74, 226.84)	(18.98, 207.01, 214.68)	(24.85, 212.13, 218.51)
f_{bottom} (MHz)	1.8151	1.8471	1.8546	1.8553	1.8944
$(I_{BC}, I_{SC}, I_x, I_y)$ (A)	(6.0, 0.45, 1.1, -1.0)	(6.0, 0.65, 1.05, -1.0)	(6.0, 0.9, 0.95, -1.0)	(6.0, 1.1, 0.85, -1.0)	(6.0, 2.0, 0.5, -1.1)

4.11 Summary and Conclusion

This chapter demonstrated the implementation of shell potentials in microgravity, which may give rise to future application in studying Bose gases condensate on curved surfaces, vortex behavior, self-interference of different parts of the shell, and even application in astrophysics by investigating models neutron stars with atoms on shell potentials [32]. A simulation was developed and was utilized for investigation of possible shell potential configurations and to compare shell potentials under gravity and in microgravity. Afterwards shell potentials were implemented experimentally. Initially, a method to transfer atoms from bare to dressed states was implemented. Then shell potentials at different positions with different detunings and Rabi frequencies under gravity and in microgravity were implemented. The resulting absorption images were compared to the predicted shapes. For most cases the simulation agreed with the experiment.

Furthermore, the simulation predicted lower potential values at the shell potential side opposing the atom chip due to the RF power declining with the distance to the atom chip. In the measurements this could only be observed for shell potential with a higher detuning. The results for shell potentials with a smaller detuning were inconclusive. The asymmetry could be observed for a constant detection frequency, but not for a sweeping detection frequency. Further investigations are necessary.

Finally, the lifetime in the shell potentials was measured. The maximal values of around one second could only be achieved close the atom chip at positions with unfavorable Rabi frequency distribution on the isomagnetic surface. Measurements of the lifetime as a function of distance to the atom chip and the RF power led to the conclusion that the lifetime is limited by the RF power.

It is concluded that a higher RF power is needed to realize lifetimes in the range of several 10th of seconds. This could for example be realized by an additional RF amplifier. Moreover, another RF antenna, for example in the shape of a loop could reduce the effect of inhomogeneous Rabi frequency on the isomagnetic surface. Additionally, the impedance of the RF antenna should be set to 50Ω in the measurement range (300 kHz to 3 MHz). This would improve the power transfer to the RF antenna and omit Rabi frequency fluctuations while changing the RF frequency.

Bibliography

1. TURYSHEV, SLAVA G.: ‘Experimental Tests of General Relativity’. *Annual Review of Nuclear and Particle Science* (2008), vol. 58(1): pp. 207–248 (cit. on p. 1).
2. MOREL, LÉO, ZHIBIN YAO, PIERRE CLADÉ, and SAÏDA GUELLATI-KHÉLIFA: ‘Determination of the fine-structure constant with an accuracy of 81 parts per trillion’. *Nature* (2020), vol. 588(7836): pp. 61–65 (cit. on p. 1).
3. ELLIS, G.F.R., R. MAARTENS, and M.A.H. MACCALLUM: *Relativistic Cosmology*. Relativistic Cosmology. Cambridge University Press, 2012 (cit. on p. 1).
4. ARUN, KENATH, S.B. GUDENAVAR, and C. SIVARAM: ‘Dark matter, dark energy, and alternate models: A review’. *Advances in Space Research* (2017), vol. 60(1): pp. 166–186 (cit. on p. 1).
5. ROVELLI, CARLO and FRANCESCA VIDOTTO: ‘Planck stars’. *International Journal of Modern Physics D* (2014), vol. 23(12): p. 1442026 (cit. on p. 1).
6. WILL, CLIFFORD M.: *Theory and Experiment in Gravitational Physics*. 2nd ed. Cambridge University Press, 2018 (cit. on p. 1).
7. SCHIFF, L. I.: ‘On Experimental Tests of the General Theory of Relativity’. *American Journal of Physics* (1960), vol. 28(4): pp. 340–343 (cit. on p. 1).
8. HALZEN, FRANCIS and ALAN MARTIN: *Quarks & Leptons: An introductory course in modern particle physics*. New York, USA: John Wiley & Sons, 1984 (cit. on p. 1).
9. WILLIAMS, JAMES G., SLAVA G. TURYSHEV, and DALE H. BOGGS: ‘Progress in lunar laser ranging tests of relativistic gravity’. *Physical Review Letters* (2004), vol. 93(26 I): pp. 1–4 (cit. on p. 2).
10. SCHLAMMINGER, S., K. Y. CHOI, T. A. WAGNER, J. H. GUNDLACH, and E. G. ADELBERGER: ‘Test of the equivalence principle using a rotating torsion balance’. *Physical Review Letters* (2008), vol. 100(4): pp. 1–4 (cit. on p. 2).
11. TOUBOUL, PIERRE et al.: ‘MICROSCOPE Mission: First Results of a Space Test of the Equivalence Principle’. *Physical Review Letters* (2017), vol. 119(23): pp. 1–7 (cit. on p. 2).
12. ASENBAUM, PETER, CHRIS OVERSTREET, MINJEONG KIM, JOSEPH CURTI, and MARK A. KASEVICH: ‘Atom-Interferometric Test of the Equivalence Principle at the 10-12 Level’. *Physical Review Letters* (2020), vol. 125(19): p. 191101 (cit. on p. 2).
13. AGUILERA, D. et al.: ‘Erratum: STE-QUEST - Test of the universality of free fall using cold atom interferometry (Classical and Quantum Gravity (2014) 31 (115010))’. *Classical and Quantum Gravity* (2014), vol. 31(15) (cit. on pp. 2, 46).

14. ‘Observation of Gravitational Waves from a Binary Black Hole Merger’. *Phys. Rev. Lett.* (6 Feb. 2016), vol. 116: p. 061102 (cit. on p. 2).
15. MACH, LUDWIG: ‘Über einen Interferenzrefraktor’. *Zeitschrift für Instrumentenkunde* (1892), vol. 11: pp. 89–93 (cit. on p. 3).
16. BORN, MAX, EMIL WOLF, A. B. BHATIA, P. C. CLEMMOW, D. GABOR, A. R. STOKES, A. M. TAYLOR, P. A. WAYMAN, and W. L. WILCOCK: *Principles of Optics: Electromagnetic Theory of Propagation, Interference and Diffraction of Light*. 7th ed. Cambridge University Press, 1999 (cit. on p. 3).
17. GROTE, ALEXANDER: ‘Ultracold Rb87: from quantum metrology to two-photon ionisation’. PhD thesis. Universität Hamburg, 2016 (cit. on pp. 3, 48).
18. ABE, MAHIRO et al.: ‘Matter-wave Atomic Gradiometer Interferometric Sensor (MAGIS-100)’. Accepted at *Quantum Science and Technology*. 2021 (cit. on p. 3).
19. ZOEST, T. van et al.: ‘Bose-Einstein Condensation in Microgravity’. *Science* (2010), vol. 328(5985): pp. 1540–1543 (cit. on p. 3).
20. BARRETT, BRYNLE, LAURA ANTONI-MICOLLIER, LAURE CHICHET, BAPTISTE BATELIER, THOMAS LÉVÈQUE, ARNAUD LANDRAGIN, and PHILIPPE BOUYER: ‘Dual matter-wave inertial sensors in weightlessness’. *Nature Communications* (2016), vol. 7: pp. 1–9 (cit. on p. 3).
21. BECKER, DENNIS et al.: ‘Space-borne Bose–Einstein condensation for precision interferometry’. *Nature* (2018), vol. 562(7727): pp. 391–395 (cit. on pp. 3, 69).
22. FRYE, KAI et al.: ‘The Bose-Einstein Condensate and Cold Atom Laboratory’. *EPJ Quantum Technology* (2021), vol. 8(1): pp. 1–38 (cit. on pp. 3, 5, 69).
23. AMMANN, HUBERT and NELSON CHRISTENSEN: ‘Delta kick cooling: A new method for cooling atoms’. *Physical Review Letters* (1997), vol. 78(11): pp. 2088–2091 (cit. on pp. 5, 24).
24. MEWES, M.-O., M. R. ANDREWS, N. J. van DRUTEN, D. M. KURN, D. S. DURFEE, C. G. TOWNSEND, and W. KETTERLE: ‘Collective Excitations of a Bose-Einstein Condensate in a Magnetic Trap’. *Phys. Rev. Lett.* (6 Aug. 1996), vol. 77: pp. 988–991 (cit. on p. 5).
25. DEPPNER, CHRISTIAN et al.: ‘Collective-mode enhanced matter-wave optics’. Submitted to *Physical Review Letters*. 2021 (cit. on pp. 5, 23, 51, 54, 77).
26. ROBINS, N.P., P.A. ALTIN, J.E. DEBS, and J.D. CLOSE: ‘Atom lasers: Production, properties and prospects for precision inertial measurement’. *Physics Reports* (2013), vol. 529(3). Atom lasers: production, properties and prospects for precision inertial measurement: pp. 265–296 (cit. on p. 5).
27. MEISTER, MATTHIAS, ALBERT ROURA, ERNST M. RASEL, and WOLFGANG P. SCHLEICH: ‘The space atom laser: An isotropic source for ultra-cold atoms in microgravity’. *New Journal of Physics* (2019), vol. 21(1) (cit. on p. 5).

-
28. ZOBAY, O. and B. M. GARRAWAY: ‘Two-dimensional atom trapping in field-induced adiabatic potentials’. *Physical Review Letters* (2001), vol. 86(7): pp. 1195–1198 (cit. on pp. 5, 69).
 29. LANNERT, C., T. C. WEI, and S. VISHVESHWARA: ‘Dynamics of condensate shells: Collective modes and expansion’. *Physical Review A - Atomic, Molecular, and Optical Physics* (2007), vol. 75(1): pp. 1–4 (cit. on pp. 5, 69).
 30. MILAGRE, G. S. and WINDER A. MOURA-MELO: ‘Magnetic vortex-like excitations on a sphere’. *Physics Letters, Section A: General, Atomic and Solid State Physics* (2007), vol. 368(1-2): pp. 155–163 (cit. on pp. 5, 69, 82).
 31. PADAVIĆ, KARMELA, KUEI SUN, COURTNEY LANNERT, and SMITHA VISHVESHWARA: ‘Vortex-antivortex physics in shell-shaped Bose-Einstein condensates’. *Physical Review A* (2020), vol. 102(4): pp. 1–9 (cit. on p. 5).
 32. SUN, KUEI, KARMELA PADAVIĆ, FRANCES YANG, SMITHA VISHVESHWARA, and COURTNEY LANNERT: ‘Static and dynamic properties of shell-shaped condensates’. *Physical Review A* (2018), vol. 98(1) (cit. on pp. 5, 117).
 33. HERR, WALDEMAR: ‘Eine kompakte Quelle quantenentarteter Gase hohen Flusses für die Atominterferometrie unter Schwerelosigkeit’. PhD thesis. Gottfried Wilhelm Leibniz Universität Hannover, 2013 (cit. on pp. 7, 9, 11).
 34. RUDOLPH, JAN: ‘Matter-Wave Optics with Bose-Einstein Condensates in Microgravity’. PhD thesis. Gottfried Wilhelm Leibniz Universität Hannover, 2016 (cit. on pp. 7, 10, 36, 37, 39, 43, 57, 77, 79).
 35. GRZESCHIK, CHRISTOPH: ‘Experiments with Bose-Einstein Condensates in Microgravity’. PhD thesis. Humboldt-Universität zu Berlin, 2017 (cit. on p. 7).
 36. RUDOLPH, JAN, WALDEMAR HERR, CHRISTOPH GRZESCHIK, TAMMO STERNKE, ALEXANDER GROTE, MANUEL POPP, DENNIS BECKER, HAUKE MÜNTINGA, HOLGER AHLERS, ACHIM PETERS, CLAUS LÄMMERZAHN, KLAUS SENGSTOCK, NACEUR GAALOUL, WOLFGANG ERTMER, and ERNST M. RASEL: ‘A high-flux BEC source for mobile atom interferometers’. *New Journal of Physics* (2015), vol. 17(6): p. 65001 (cit. on p. 7).
 37. PAHL, JULIA, ALINE N. DINKELAKER, CHRISTOPH GRZESCHIK, JULIEN KLUGE, MAX SCHIEMANGK, ANDREAS WICHT, ACHIM PETERS, and MARKUS KRUTZIK: ‘Compact and robust diode laser system technology for dual-species ultracold atom experiments with rubidium and potassium in microgravity’. *Applied Optics* (2019), vol. 58(20): p. 5456 (cit. on p. 7).
 38. SCHIEMANGK, MAX, KAI LAMPMANN, ALINE DINKELAKER, ANJA KOHFELDT, MARKUS KRUTZIK, CHRISTIAN KÜRBIS, ALEXANDER SAHM, STEFAN SPIESSBERGER, ANDREAS WICHT, GÖTZ ERBERT, GÜNTHER TRÄNKLE, and ACHIM PETERS: ‘High-power, micro-integrated diode laser modules at 767 and 780 nm for portable quantum gas experiments’. *Applied Optics* (2015), vol. 54(17): p. 5332 (cit. on p. 7).
 39. POPP, MANUEL: ‘Compact, low-noise current drivers for atom chips’. PhD thesis. Gottfried Wilhelm Leibniz Universität Hannover, 2017 (cit. on p. 8).

40. STERNKE, TAMMO: ‘An ultracold high-flux source for matter-wave interferometry in microgravity’. PhD thesis. Carl von Ossietzky Universität Oldenburg, 2018 (cit. on pp. 8, 79).
41. REINAUDI, G., T. LAHAYE, Z. WANG, and D. GUÉRY-ODELIN: ‘Strong saturation absorption imaging of dense clouds of ultracold atoms’. *Optics Letters* (2007), vol. 32(21): p. 3143 (cit. on p. 10).
42. CORGIER, R, S AMRI, W HERR, H AHLERS, J RUDOLPH, D GUÉRY-ODELIN, E M RASEL, E CHARRON, and N GAALOUL: ‘Fast manipulation of Bose–Einstein condensates with an atom chip’. *New Journal of Physics* (May 2018), vol. 20(5): p. 055002 (cit. on pp. 11, 37, 79).
43. WALSER, REINHOLD: ‘MatterWaveSim / unpublished’. 2018 (cit. on pp. 12, 77, 80).
44. PETERS, ACHIM, KENG YEOW CHUNG, and STEVEN CHU: ‘Measurement of gravitational acceleration by dropping atoms’. *Nature* (1999), vol. 400(6747): pp. 849–852 (cit. on p. 13).
45. DIMOPOULOS, SAVAS, PETER W. GRAHAM, JASON M. HOGAN, and MARK A. KASEVICH: ‘Testing general relativity with atom interferometry’. *Physical Review Letters* (2007), vol. 98(11): pp. 1–4 (cit. on p. 13).
46. YOUNG, BRENTON, MARK KASEVICH, and STEVEN CHU: ‘Precision Atom Interferometry with Light Pulses’. *Atom Interferometry*. Ed. by BERMAN, PAUL R. San Diego: Academic Press, 1997: pp. 363–406 (cit. on pp. 13, 15, 28, 29).
47. RUDOLPH, JAN, THOMAS WILKASON, MEGAN NANTEL, HUNTER SWAN, CONNOR M. HOLLAND, YIJUN JIANG, BENJAMIN E. GARBER, SAMUEL P. CARMAN, and JASON M. HOGAN: ‘Large Momentum Transfer Clock Atom Interferometry on the 689 nm Intercombination Line of Strontium’. *Phys. Rev. Lett.* (8 Feb. 2020), vol. 124: p. 083604 (cit. on p. 13).
48. BRABEC, THOMAS and FERENC KRAUSZ: ‘Intense few-cycle laser fields: Frontiers of nonlinear optics’. *Reviews of Modern Physics* (2000), vol. 72(2): pp. 545–591 (cit. on p. 15).
49. ABEND, SVEN: ‘Atom-chip Gravimeter with Bose-Einstein Condensates’. PhD thesis. Gottfried Wilhelm Leibniz Universität Hannover, 2017 (cit. on pp. 17, 62).
50. CRONIN, ALEXANDER D., JÖRG SCHMIEDMAYER, and DAVID E. PRITCHARD: ‘Optics and interferometry with atoms and molecules’. *Reviews of Modern Physics* (2009), vol. 81(3): pp. 1051–1129 (cit. on p. 18).
51. MÜLLER, HOLGER, SHENG WEY CHIOU, and STEVEN CHU: ‘Atom-wave diffraction between the Raman-Nath and the Bragg regime: Effective Rabi frequency, losses, and phase shifts’. *Physical Review A - Atomic, Molecular, and Optical Physics* (2008), vol. 77(2): pp. 1–18 (cit. on p. 19).

-
52. LÉVÈQUE, T., A. GAUGUET, F. MICHAUD, F. PEREIRA DOS SANTOS, and A. LANDRAGIN: ‘Enhancing the area of a Raman atom interferometer using a versatile double-diffraction technique’. *Physical Review Letters* (2009), vol. 103(8): pp. 1–4 (cit. on p. 19).
 53. GIESE, E., A. ROURA, G. TACKMANN, E. M. RASEL, and W. P. SCHLEICH: ‘Double Bragg diffraction: A tool for atom optics’. *Physical Review A - Atomic, Molecular, and Optical Physics* (2013), vol. 88(5): pp. 1–23 (cit. on pp. 19, 21).
 54. AHLERS, H. et al.: ‘Double Bragg Interferometry’. *Physical Review Letters* (2016), vol. 116(17): pp. 1–6 (cit. on p. 19).
 55. GIESE, ENNO: ‘Mechanisms of matter-wave diffraction and their application to interferometers’. *Fortschritte der Physik* (2015), vol. 63(6): pp. 337–410 (cit. on pp. 19, 20).
 56. DAVIS, K. B., M. -O. MEWES, M. R. ANDREWS, N. J. van DRUTEN, D. S. DURFEE, D. M. KURN, and W. KETTERLE: ‘Bose-Einstein Condensation in a Gas of Sodium Atoms’. *Phys. Rev. Lett.* (22 Nov. 1995), vol. 75: pp. 3969–3973 (cit. on pp. 20, 69).
 57. ANDERSON, M. H., J. R. ENSHER, M. R. MATTHEWS, C. E. WIEMAN, and E. A. CORNELL: ‘Observation of Bose-Einstein Condensation in a Dilute Atomic Vapor’. *Science* (1995), vol. 269(5221): pp. 198–201 (cit. on pp. 20, 69).
 58. PETHICK, C. J. and H. SMITH: *Bose-Einstein Condensation in Dilute Gases*. 2nd ed. Cambridge University Press, 2008 (cit. on pp. 20–23, 37).
 59. CASTIN, Y. and R. DUM: ‘Bose-einstein condensates in time dependent traps’. *Physical Review Letters* (1996), vol. 77(27): pp. 5315–5319 (cit. on pp. 22, 23).
 60. LEANHARDT, A. E., T. A. PASQUINI, M. SABA, A. SCHIROTZKEK, Y. SHIN, D. KIELPINSKI, D. E. PRITCHARD, and W. KETTERLE: ‘Cooling Bose-Einstein condensates below 500 picokelvin’. *Science* (2003), vol. 301(5639): pp. 1513–1515 (cit. on p. 23).
 61. SIMSARIAN, J. E., J. DENSLAG, MARK EDWARDS, CHARLES W. CLARK, L. DENG, E. W. HAGLEY, K. HELMERSON, S. L. ROLSTON, and W. D. PHILLIPS: ‘Imaging the phase of an evolving Bose-Einstein condensate wave function’. *Physical Review Letters* (2000), vol. 85(10): pp. 2040–2043 (cit. on p. 25).
 62. SALEH, BAHAA E A and MALVIN CARL TEICH: *Fundamentals of photonics; 2nd ed.* Wiley series in pure and applied optics. New York, NY: Wiley, 2007 (cit. on p. 34).
 63. DEPPNER, CHRISTIAN. PhD thesis. Gottfried Wilhelm Leibniz Universität Hannover, 2021 (cit. on pp. 36, 37, 55).
 64. CORNELIUS, MERLE. PhD thesis. Universität Bremen, 2021 (cit. on pp. 39, 51).
 65. ANDREWS, M. R., C. G. TOWNSEND, H. J. MIESNER, D. S. DURFEE, D. M. KURN, and W. KETTERLE: ‘Observation of interference between two bose condensates’. *Science* (1997), vol. 275(5300): pp. 637–641 (cit. on p. 46).

66. HUGBART, M., J. A. RETTER, F. GERBIER, A. F. VARÓN, S. RICHARD, J. H. THYWISSEN, D. CLÉMENT, P. BOUYER, and A. ASPECT: ‘Coherence length of an elongated condensate : AAA study by matter-wave interferometry’. *European Physical Journal D* (2005), vol. 35(1): pp. 155–163 (cit. on p. 46).
67. KRUTZIK, MARKUS: ‘Matter wave interferometry in microgravity’. PhD thesis. Humboldt-Universität zu Berlin, 2014 (cit. on p. 61).
68. RILEY, WILLIAM and DAVID HOWE: *Handbook of Frequency Stability Analysis*. en. 2008-07-01 2008 (cit. on p. 63).
69. WU, B., Z. Y. WANG, B. CHENG, Q. Y. WANG, A. P. XU, and Q. LIN: ‘Accurate measurement of the quadratic Zeeman coefficient of 87Rb clock transition based on the Ramsey atom interferometer’. *Journal of Physics B: Atomic, Molecular and Optical Physics* (2014), vol. 47(1) (cit. on p. 66).
70. GRIMM, RUDOLF, MATTHIAS WEIDEMÜLLER, and YURI B. OVCHINNIKOV: ‘Optical Dipole Traps for Neutral Atoms’. Ed. by BEDERSON, BENJAMIN and HERBERT WALTHER. Vol. 42. *Advances In Atomic, Molecular, and Optical Physics*. Academic Press, 2000: pp. 95–170 (cit. on p. 69).
71. BLOCH, IMMANUEL, JEAN DALIBARD, and WILHELM ZWERGER: ‘Many-body physics with ultracold gases’. *Reviews of Modern Physics* (2008), vol. 80(3): pp. 885–964 (cit. on p. 69).
72. COLOMBE, Y., E. KNYAZCHYAN, O. MORIZOT, B. MERCIER, V. LORENT, and H. PERRIN: ‘Ultracold atoms confined in rf-induced two-dimensional trapping potentials’. *Europhysics Letters* (2004), vol. 67(4): pp. 593–599 (cit. on pp. 69, 76, 95).
73. HOFFERBERTH, S., B. FISCHER, T. SCHUMM, J. SCHMIEDMAYER, and I. LESANOVSKY: ‘Ultracold atoms in radio-frequency dressed potentials beyond the rotating-wave approximation’. *Physical Review A - Atomic, Molecular, and Optical Physics* (2007), vol. 76(1): pp. 1–5 (cit. on pp. 69, 77).
74. LESANOVSKY, IGOR and WOLF VON KLITZING: ‘Time-averaged adiabatic potentials: Versatile matter-wave guides and atom traps’. *Physical Review Letters* (2007), vol. 99(8): pp. 1–4 (cit. on p. 69).
75. ELLIOTT, ETHAN R., MARKUS C. KRUTZIK, JASON R. WILLIAMS, ROBERT J. THOMPSON, and DAVID C. AVELINE: ‘NASA’s cold atom lab (CAL): System development and ground test status’. *npj Microgravity* (2018), vol. 4(1): pp. 1–7 (cit. on p. 69).
76. ZENER, CLARENCE: ‘Non-adiabatic crossing of energy levels’. *Proc. Roy. Soc. A* (1932), vol. 33(1929): pp. 696–702 (cit. on p. 70).
77. EARNSHAW, S.: ‘On the Nature of the Molecular Forces which Regulate the Constitution of the Luminiferous Ether’. *Transactions of the Cambridge Philosophical Society* (Jan. 1848), vol. 7: p. 97 (cit. on p. 71).

-
78. KETTERLE, W., D. S. DURFEE, and D. M. STAMPER-KURN: ‘Making, probing and understanding Bose-Einstein condensates’. *PROCEEDINGS OF THE INTERNATIONAL SCHOOL OF PHYSICS "ENRICO FERMI", COURSE CXL, EDITED BY M. INGUSCIO, S. STRINGARI AND C.E. WIEMAN* (IOS. Press, 1999: p. 67 (cit. on pp. 71, 77).
 79. PERRIN, HÉLÈNE and BARRY M. GARRAWAY: ‘Trapping Atoms With Radio Frequency Adiabatic Potentials’. *Advances in Atomic, Molecular and Optical Physics* (2017), vol. 66: pp. 181–262 (cit. on pp. 73, 116).
 80. HOFFERBERTH, S., B. FISCHER, T. SCHUMM, J. SCHMIEDMAYER, and I. LESANOVSKY: ‘Ultracold atoms in radio-frequency dressed potentials beyond the rotating-wave approximation’. *Physical Review A - Atomic, Molecular, and Optical Physics* (2007), vol. 76(1): pp. 1–5 (cit. on p. 73).
 81. FORTÁGH, JÓZSEF and CLAUS ZIMMERMANN: ‘Magnetic microtraps for ultracold atoms’. *Rev. Mod. Phys.* (1 Feb. 2007), vol. 79: pp. 235–289 (cit. on p. 74).
 82. ZOBAY, O. and B. M. GARRAWAY: ‘Atom trapping and two-dimensional Bose-Einstein condensates in field-induced adiabatic potentials’. *Physical Review A - Atomic, Molecular, and Optical Physics* (2004), vol. 69(2): p. 15 (cit. on p. 74).
 83. BURROWS, KATHRYN A., HÉLÈNE PERRIN, and BARRY M. GARRAWAY: ‘Nonadiabatic losses from radio-frequency-dressed cold-atom traps: Beyond the Landau-Zener model’. *Physical Review A* (2017), vol. 96(2) (cit. on p. 74).
 84. MARTIN, A. G., K. HELMERSON, V. S. BAGNATO, G. P. LAFYATIS, and D. E. PRITCHARD: ‘Rf spectroscopy of trapped neutral atoms’. *Physical Review Letters* (1988), vol. 61(21): pp. 2431–2434 (cit. on p. 75).
 85. ESSLINGER, TILMAN, IMMANUEL BLOCH, and THEODOR W. HÄNSCH: ‘Bose-Einstein condensation in a quadrupole-Ioffe-configuration trap’. *Phys. Rev. A* (4 Oct. 1998), vol. 58: R2664–R2667 (cit. on p. 76).
 86. BECKER, DENNIS: ‘Demonstration einer neuartigen kompakten chip-basierten Quelle kalter Atome’. MA thesis. Gottfried Wilhelm Leibniz Universität Hannover, 2011 (cit. on p. 109).
 87. MORIZOT, O., L. LONGCHAMBON, R. KOLLENGODE EASWARAN, R. DUBESSY, E. KNYAZCHYAN, P. E. POTTIE, V. LORENT, and H. PERRIN: ‘Influence of the Radio-Frequency source properties on RF-based atom traps’. *European Physical Journal D* (2008), vol. 47(2): pp. 209–214 (cit. on p. 112).

List of Figures

1.1	Illustration of the drop tower. Figure taken from [17].	3
1.2	Sketch of the optical and atomic Mach-Zehnder interferometer.	4
2.1	Overview of the QUANTUS-2 apparatus.	8
2.2	Overview of the three layers of the QUANTUS-2 atom chip.	9
2.3	The two imaging systems of the QUANTUS-2 apparatus.	10
3.1	Sketch of 1- and 2-photon interactions.	15
3.2	Sketch of the Bragg diffraction process.	16
3.3	Different diffraction regimes for single Bragg diffraction.	17
3.4	Velocity selection of different pulse shapes.	20
3.5	Double diffraction Rabi oscillations.	21
3.6	Illustration of the magnetic lensing process.	24
3.7	Sketch of an Open-Ramsey type interferometer with single diffraction . . .	26
3.8	Sketch of an Open-Ramsey type interferometer with double diffraction. . . .	27
3.9	Mach-Zehnder interferometer sketch.	28
3.10	Sketch of an asymmetric Mach-Zehnder interferometer.	31
3.11	The atom interferometry setup.	32
3.12	Measurement of the offset frequency with the current-by-pass.	33
3.13	Power Stability of the <i>Spincore PulseBlaster</i> and the following amplifier chain. .	35
3.14	Path of the two atom interferometry paths in the distribution module. . . .	36
3.15	Phase difference between the two beams imprinted in the intensity of the pulse.	37
3.16	Phase drift in three different measurements.	38
3.17	y-z position of the magnetic trap at position a with varying z-bias-coil current. .	38
3.18	Comparison of the flight trajectories of <i>parabola1</i> and <i>parabola2</i>	40
3.19	Pulse duration scan for single diffraction pulses	42
3.20	Comparison of different pulse durations.	43
3.21	Diffractions to higher order for 80 μs , 100 μs , and 120 μs pulses.	45
3.22	Single diffraction stability.	45
3.23	Example of Equation 3.59 fitted to an absorption image with an interrogation time of 500 μs	47
3.24	The fringe spacing and the contrast of an ORI with single diffraction. . . .	48
3.25	Rabi oscillation with double diffraction.	49
3.26	Example of Equation 3.59 fitted to an absorption image with an interrogation time of 250 μs	49
3.27	The fringe spacing and the contrast of an ORI with double diffraction. . . .	51

3.28	The $+2\hbar k$ and $0\hbar k$ diffraction order of an Open-Ramsey type interferometer in microgravity.	52
3.29	Open Ramsey type interferometer with unlensed BECs in microgravity. . .	53
3.30	Analysis of the images from Figure 3.29.	53
3.31	Optical shear interferometer. Figure taken from thorlabs.com.	54
3.32	Cold atom clouds 1.5 s after the magnetic lens.	54
3.33	Illustration of the <i>virtual time-of-flight</i> principle in the atomic shear interferometer.	55
3.34	Atomic shear interferometer gallery.	56
3.35	Fit of the $ 0\hbar k\rangle$ port for $\tau = 1.5$ ms.	57
3.36	Evaluation of the atomic shear interferometer gallery (Figure 3.34).	58
3.37	Asymmetric Mach-Zehnder interferometer with single diffraction.	59
3.38	Contrast in the asymmetric Mach-Zehnder interferometer.	60
3.39	Fringe spacing in the asymmetric Mach-Zehnder interferometer.	61
3.40	Illustration of the effects of the capsule rotation on an asymmetric Mach-Zehnder interferometer.	62
3.41	Fringe scan at different interrogation times of the Mach-Zehnder type Interferometer with single diffraction.	64
3.42	Measurement of the acceleration of the Bragg lattice.	65
3.43	The position and the size of the BEC during the Mach-Zehnder sequence. .	67
4.1	Illustration of the Landau-Zener model.	70
4.2	Illustration of an Ioffe-Pritchard magnetic trap created with a Z-wire and a bias field.	72
4.3	<i>Base</i> and <i>Science Chip</i> structures used for shell potentials.	76
4.4	Magnetic trap configurations with different y-bias-coils currents.	78
4.5	Simulation of the shell potentials at positions <i>a2</i> , <i>b</i> , and <i>c</i>	81
4.6	Slices through the shell potential at position <i>a2</i>	83
4.7	Slices through the shell potential at position <i>b</i>	84
4.8	Slices through the shell potential at position <i>c</i>	85
4.9	Comparison of the curvature at the minimum of the shell potentials.	86
4.10	Shell potential at position <i>a2</i> under gravity and in microgravity.	87
4.11	Shell potential at position <i>b</i> under gravity and in microgravity.	88
4.12	Atom occupation in the potential at position <i>a2</i>	89
4.13	Atom occupation in the potential at position <i>b</i>	90
4.14	RF power of NI PXI 5421 and impedance of RF U-wire.	91
4.15	Cold atom cloud temperature after transport.	92
4.16	Illustration of the transfer to the dressed states.	94
4.17	Illustration of two transfer ramps.	95
4.18	Simple transfer procedure from bare states to dressed states.	96
4.19	Transport duration scan of <i>procedure1</i> for a final frequency of 2.3 MHz. . .	98
4.20	Transfer procedure from the bare states to the dressed states with an additional ramp through the potential bottom offset frequency (1 ms duration). 98	

4.21	Transfer procedure from the bare states to the dressed states with an additional ramp through the potential bottom offset frequency (10 ms duration).	99
4.22	Rabi frequency scan at position $a2$	100
4.23	Scan of the Rabi frequency at position c and a detuning of 31 kHz in microgravity.	101
4.24	Scan of the Rabi frequency at position c and a detuning of 231 kHz in microgravity.	102
4.25	Scan of the detuning at position $a2$ under gravity viewed from the primary detection system.	103
4.26	Scan of the detuning at position $a2$ under gravity viewed from the secondary detection system.	104
4.27	Scan of the detuning at position b in microgravity.	105
4.28	Scan of the detuning at position c in microgravity	105
4.29	Comparison of shell potentials at positions $a2$, b , and c in microgravity and under gravity from the primary detection system	107
4.30	Comparison of shell potentials at positions $a2$, b , and c in microgravity and under gravity from the secondary detection system	107
4.31	Different ensemble temperatures at position c	108
4.32	Different ensemble temperatures at position c	109
4.33	Simulation of the occupancy with thermal atoms of the shell potential at position c	111
4.34	Lifetime fit at position $a2$ for maximal RF power and a detuning of 206 kHz.	113
4.35	Lifetime measurements at position $a2$ and b	114
4.36	Lifetime at position $a2$ for different ensemble temperatures.	115
4.37	Life time in shell potentials as a function of the distance to the atom chip.	115

List of Tables

2.1 Properties of different positions dubbed a , $a2$, b , and c	12
3.1 Sequence of steps for the trajectory <i>parabola1</i>	39
3.2 Sequence of steps for the trajectory <i>parabola2</i>	40
3.3 Double diffraction efficiency during the drop campaign.	51
3.4 Measurement parameters and fit results of the atomic shear interferometer.	56
4.1 Properties of different positions dubbed position $a2$, b , and c	80
4.2 Magnetic field configuration for lifetime measurements.	116

Publications

Scientific publications

- "Collective-mode enhanced matter-wave optics" Deppner, Herr, Cornelius, **Stromberger**, Sternke, Grzeschik, Grote, Rudolph, Herrmann, Krutzik, Wenzlawski, Corgier, Charon, Guéry-Odelin, Gaaloul, Lämmerzahl, Peters, Windpassinger, Rasel. Submitted to Phys. Rev. Lett. (2021).
- "Spatially resolved thermometry by means of an atomic shear interferometer", Cornelius, **Stromberger**, Pahl, Deppner, *et. al.*. Manuscript in preparation.

Submissions to conferences

- "QUANTUS-2 – Quantum Gases Under Microgravity", **Stromberger**, Cornelius, Pahl, Deppner, Wenzlawski, Windpassinger. *43rd COSPAR Scientific Assembly*. 2021 (virtual).
- "QUANTUS-2 - Ultra Low Expansion Atomic Source for Matter Wave Interferometry in Extended Free Fall", **Stromberger**, Cornelius, Deppner, Herr, Wenzlawski, Windpassinger. *Okinawa School in Physics: Coherent Quantum Dynamics*. 2019 (Onna, Okinawa, Japan).
- "Ultracold Atoms for Matter Wave Interferometry in Microgravity", Sternke, Deppner, **Stromberger**, Cornelius, Herr, Herrmann, Lämmerzahl. *69th International Astronautical Congress*. 2018 (Bremen, Germany).
- "QUANTUS-2 - Ultra Low Expansion Atomic Source for Matter Wave Interferometry in Extended Free Fall", **Stromberger**, Sternke, Gaaloul, Wenzlawski, Windpassinger. *German Physical Society spring meeting*. 2018 (Erlangen, Germany).
- "QUANTUS-2 - Ultra Low Expansion Atomic Source for Matter Wave Interferometry in Extended Free Fall", **Stromberger**, Grote, Wenzlawski, Windpassinger. *German Physical Society spring meeting*. 2017 (Mainz, Germany).
- "QUANTUS 2 - a Matter Wave Interferometer in Extended Free Fall", **Stromberger**, Grote, Wenzlawski, Windpassinger. *Frontiers in Matter Wave Optics*. 2016 (Arcahon, France).